REPUBLIQUE ALGERIENNE DEMOCRATIQUE ET POPULAIRE
Ministre de l'enseignement suprieur et de la recherche scientifique
Université Ferhat Abbas Sétif 1

Faculté des Sciences, Département de Physique

Thèse

Présentée pour obtenir le titre de Docteur en Radiophysique et Imagerie Biomédicale

Développement d'une approche hybride pour l'amélioration des images CBCT pour la radiothérapie adaptative

Halima Saadia Kidar

Présentée le 01 Décembre 2020, devant le jury composé de:

Faycal Kharfi	Pr. Université Ferhat Abbas Sétif 1	Président
Hacene Azizi	Pr. Université Ferhat Abbas Sétif 1	Directeur de thèse
Habib Zaidi	Pr. Hôpitaux Universitaires Genève, Suisse	Examinateur
Mohamed Kaddeche	Pr. Université Badji Mokhtar, Annaba	Examinateur
Djamel Eddine. C. Belkhiat	Dr.Université Ferhat Abbas Sétif 1	Examinateur
Saadia Benhalouche	Dr. Université des Sciences et de la Technologie d'Oran	Invitée

People's Democratic Republic of Algeria
Ministry of Higher Education and Scientific Research
University Ferhat Abbas Setif 1

Faculty of Sciences, Department of Physics

PhD Thesis

Presented to obtain Doctor degree in Radiation Physics and Biomedical Imaging

Development of a hybrid approach for the enhancement of CBCT images for adaptive radiation therapy

Halima Saadia Kidar

Presented on December 1,2020, in front of the jury:

Faycal Kharfi	Pr. Ferhat Abbas Setif 1 University	President
Hacene Azizi	Pr. Ferhat Abbas Setif 1 University	Advisor
Habib Zaidi	Pr. Geneva University Hospital , Switzerland	Examiner
Mohamed Kaddeche	Pr. Badji Mokhtar-Annaba University	Examiner
Djamel Eddine. C. Belkhiat	Dr. Ferhat Abbas Setif 1 University	Examiner
Saadia Benhalouche	Dr. University of Sciences and Technology Mohamed-Boudiaf of Oran	Invited

For my mother,
For who lost their loved ones to cancer,

Aknowledgments

Undertaking this PhD has been a truly life-changing experience for me and it would not have been possible to do without the support and guidance that I received from many people.

First and foremost, I would like to thank my supervisor ***Doctor Hacene AZIZI*** for the patient guidance, encouragement and advices he has provided throughout my time as his student. I greatly appreciate the freedom he has given me to find my own path and the support he offered when needed. Additionally, I would like to thank my committee members ***Pr. Faycal KHARFI*** , ***Pr. Habib ZAIDI***, ***Pr. Mohamed Kaddeche***, ***Dr. Djamel Eddine BELKHIAT***, and ***Dr. Saadia BENHALOUCHE*** for their interest in my work.

I also express my gratitude to the head of the Dosing, Analysis and Characterization with high resolution (DAC-HR) Laboratory, ***Professor Faycal KHARFI***, for accepting me into his group and supporting my work.

Spacial thanks go to the stuff of the department of radiotherapy (Centre de lutte Contre le Cancer) in Setif, Algeria, for providing the data sets used in this work.

This work would also have been impossible without the help of ***Miss Wafa BOUKELLOUZ*** from the department of computer sciences ate Ferhat Abbas Setif University. Thank you so much for your knowledge, skills, time and support.

Finally, I would like to acknowledge friends and family who always supported me. First and foremost, I would thank my father ***Lakhdar***, sisters ***Khadidja, Fadhila, Naima and Faiza*** and my brother ***Mhamed Islem*** for believing in me and being there for practical support in all those things of life beyond doing a PhD.

Abstract

Recently, the integration of in-board cone beam computed tomography (CBCT) systems into linear accelerators has provided not only a powerful tool for improving the accuracy of patient positioning but also it makes it possible to adapt the treatment planning with the patient anatomy modifications throughout the entire treatment, known as adaptive radiation therapy (ART). During ART planning, after applying a rigid registration between daily acquired CBCT images and planning CT (pCT) scans and getting information about patients structural changes and internal organs deformations, a repeated acquisition of CT images (repCT) is needed for replanning if the patients anatomical changes are significative. Although repCT images provide the most up-to-date information for a human body with an accurate hounsfield unit (HU) distribution for dose calculation, their repeated acquisition may pose a health concern to patients due to the additional dose. Therefore, the aim of this thesis is to investigate the feasibility of daily CBCT images for dose calculation instead of acquiring repCT images. The main interest is to propose a promising strategy to overcome the limitations related to the high amount of scatter that reduces the quality of CBCT images compared to the pCT.

To this end, we proposed three complementary approaches that allow the correction of the HU distribution in the CBCT images. The first proposed approach is inspired from the fact that the CBCT and the pCT images have not the same gray-level histograms. Therefore, we applied the histogram matching (HM) process to resemble their histograms and offer the possibility to distinguish the different tissue types in the CBCT images. As a second approach, we proposed the application of multilevel threshold (MLT) to improve the correctness of the HU distribution obtained with HM. Finally, in the third approach we proposed the generalization of the previously proposed approaches to contribute in the minimization of the ART workload requirements. The main idea is to include the notion of inter-patient deformable registration in order to investigate the pCT images available in the archive for the correction of CBCT images rather than acquiring new CT images for each patient.

Results of the visual and statistical analysis showed that the proposed approaches

can improve the HU distribution in the CBCT images and generate corrected images in good agreement with the pCT.

Keywords: CBCT correction; deformable registration; histogram matching; multilevel threshold; adaptive radiation therapy.

Résumé

Récemment, l'intégration des systèmes de tomodensitométrie à faisceau conique (CBCT) embarqués dans les accélérateurs linéaires a fourni non seulement un outil puissant pour l'amélioration de la précision du positionnement du patient mais il a permis aussi d'adapter la planification du traitement aux modifications de l'anatomie du patient tout au long du traitement, connu sous le nom de radiothrapie adaptative (ART). Pendant la planification du ART, après avoir appliqué un recalage rigide entre les images CBCT du jour et les images CT de planification (pCT) et obtenu des informations sur les changements structurels du patient et les déformations des organes internes, une acquisition répétée des images CT (repCT) est nécessaire pour la replanification si les changements anatomiques sont significatifs. Bien que les images repCT fournissent les informations du jour sur le corps humain avec une distribution prcise des unités hounsfield (HU) nécéssaires pour le calcul de dose, leur acquisition répétée peut poser un problème de santé aux patients à cause de l'accumulation de dose. Par conséquent, le but de cette thèse est d'étudier la faisabilité du calcul de dose basé sur des images CBCT au lieu d'acquérir les images repCT. L'intérêt principal est de proposer une stratégie pour surmonter les limitations liées à la grande quantité du rayonnement diffusé qui réduit la qualité des images CBCT par rapport aux images pCT.

À cette fin, nous avons proposé trois approches complémentaires qui permettent la correction de la distribution des HU dans les images CBCT. La première approche proposée s'inspire du fait que les images CBCT et pCT n'ont pas les mêmes histogrammes de niveaux de gris. Par conséquent, nous avons appliqué le processus de correspondance d'histogramme (HM) pour ressembler leurs histogrammes et offrir la possibilité de distinguer les différents types de tissus dans les images CBCT. Comme deuxième approche, nous avons proposé l'application d'un seuillage à plusieurs niveaux (MLT) pour améliorer l'exactitude de la distribution des HU obtenue avec HM. Enfin, dans la troisième approche, nous avons proposé la généralisation des approches proposées précédemment pour contribuer à la réduction des exigences de charge de travail de l'ART. L'idée principale est d'inclure la notion du recalage

déformable inter-patients afin d'exploiter les images pCT disponibles dans l'archive pour la correction des images CBCT au lieu d'acquérir de nouvelles images CT pour chaque patient.

Les résultats de l'analyse visuelle et statistique ont montré que les approches proposées peuvent améliorer la distribution des HU dans les images CBCT et générer des images corrigées en bon accord avec les images pCT.

Mots clés: Correction des CBCT; recalage déformable; correspondance des histogrammes; seuillage à plusieurs niveaux; radiothérapie adaptative.

Contents

List of publications

The thesis is based on the following papers :

Published papers

- Halima Saadia Kidar, Hacene Azizi and Wafa Boukellouz. Evaluation of CT to CBCT Deformable Registration Algorithms for Adaptive Radiation Therapy. *Proceeding of Engineering and Technology.* 33:40-44, 2017.

- Halima Saadia Kidar and Hacene Azizi. Assessing the impact of choosing different deformable registration algorithms on Cone-Beam CT enhancement by histogram matching. *Radiation Oncology*, 13(1):217, 2018.

- Halima Saadia Kidar and Hacene Azizi. Enhancement of Hounsfield unit distribution in cone-beam CT images for adaptive radiation therapy: Evaluation of a hybrid correction approach. *Physica Medica*, 69:269-274, 2020.

Unpublished papers

- Halima Saadia Kidar, Hadjer Saadallah and Hacene Azizi. Generalization of a hybrid approach for the correction of cone beam CT images using an inter-patient image registration.
  "Accepted for publication in the proceeding of the First International Conference on Communications, Control Systems and Signal Processing (CCSSP 2020)."

List of Figures

List of Tables

List of abbreviations

2D	two-dimensional
3D	three-dimensional
3D-CRT	3-dimensional conformal radiotherapy
ART	adaptive radiotherapy
ASGD	adaptive stochastic gradient descent
CC	correlation coefficient
CNR	contrast to noise ratio
CT	computed tomography
CTV	clinical target volume
$\mathbf{D_{min}}$	minimum dose
$\mathbf{D_{max}}$	maximum dose
$\mathbf{D_{mean}}$	mean dose
DCNN	deep convolutional neural network
DIR	deformable image registration
DL	deep learning
DOFs	degrees of freedom
DVHs	dose-volume histograms
ED	electron density
FOV	field of view
GD	gradient descent
GAN	generative adversarial network
GTV	gross tumor volume

H&N	head and neck
HM	histogram matching
HU	hounsfield unit
ICRU	International Commission on Radiation Units and Measurement
IGRT	image guided radiotherapy
IMRT	intensity modulated radiotherapy
ITK	insight segmentation and registration toolkit
ITV	internal target volume
kV-CBCT	kilovoltage cone-beam CT
Linac	linear accelerator
MAE	mean absolute error
MC	Monte Carlo
MI	mutual information
MLC	multileaf collimator
MLT	multilevel threshold
MRI	magnetic resonance imaging
MSD	mean squared difference
MU	monitor unit
MV-CBCT	megavoltage cone-beam CT
NCC	normalized correlation coefficient
NMI	normalized mutual information
OARs	organs at risk
pCT	planning computed tomography
PET	positron emission tomography
PTV	planning target volume
repCT	replanning computed tomography
RMSD	root mean squared difference
ROIs	regions of interest

RR rigid registration

RT radiotherapy

SD standard deviation

VMAT volumetric modulated arc therapy

VOIs volumes of interest

Introduction

Recently, the growing use of modern imaging modalities in radiotherapy (RT) has allowed a better medical care for cancer patients under the treatment machine. Thanks to the integration of in-room imaging systems as the cone beam computed tomography (CBCT), the verification and the correction of the patient's setup during the course of treatment in three dimensions with sufficient soft tissue contrast and low patient dose become possible. Moreover, the development of CBCT systems in terms of images acquisition, rapidity and improved image quality has allowed the appearance of more sophisticated treatment techniques as adaptive radiation therapy (ART). This technique aims to adapt the treatment planning with patient anatomy modification throughout the entire treatment; it is mainly based on three complex and consuming time processes: acquisition of daily CBCT images for making decision if the re-planning is necessary by comparing them to the CT images, the second process deals with the acquisition of new planning CT (pCT) images and the delineation of volumes of interest to provide a base for the last process which is the dose re-calculation.

The development of such treatment techniques has offered a huge place to integrate the medical image processing field in clinical routine. With its various processes, this field has enabled the improvement of delivered treatment in terms of precision and execution time. Deformable registration (DR) process could be considered as the most used in ART because it highlighted the importance of investigating different imaging modalities as CBCT images to quantify organs deformation [1], propagate contours [2] or calculate the dose accumulation [3], all by deforming the pCT to the CBCT images. Nowadays, another application of DR aiming to generate from the daily CBCT images a basis for dose calculation without the need to acquire new pCT images and keep the dose to the patient as low as possible has been carried out. Yet, the use of CBCT images for such application is a challenge due to the high amount of scatter that reduces their quality and causes a lack of CT number, called also Hounsfield units (HU), accuracy compared to the pCT images [4]. Therefore, many approaches for the correction of CBCT images, either by the combination of DR with medical image processing methods or by direct correction approaches, can be found in literature.

In DR-based approaches, the main idea is to apply a medical image processing methods as the HU mapping [5], multilevel threshold [6], histogram matching [7], creation of shading map [8] or the use of deep learning [9] after deforming the pCT to the CBCT images in order to transfer the HU distribution to the CBCT images. Direct approaches have also been employed to correct CBCT images; they can be classified into three approaches: the first one, which is the most obvious, is the use of physical scatter rejection techniques as anti-scatter grids [10] or bow-tie filters during the data acquisition. The second approach is the scatter correction based on Monte Carlo modeling of the imaging system [11] and the last approach is the calibration of CBCT systems using phantoms [12].

Most of these studies converge to the use of DR-based approaches due to their efficiency and rapidity compared to the integration of hardware or the use of simulation. Therefore, to justify this choice, this thesis aims first to review the different methods existing in the literature and determine their points of strength and weakness. Then, based on the results of comparison, it proposes a new approach for the correction of HU distribution in the CBCT images.

Thesis outline

The thesis is divided into five chapters, the first two ones present the basic clinical and technical notions required for the comprehension of the different techniques cited in this work. The remaining three chapters present the main contributions for the generation of corrected CBCT images.

Each chapter can be described as follows:

Chapter 1 presents the main concepts frequently used in the clinical routine of radiotherapy. It also presents the evolution of RT techniques with emphasis on the reasons behind the integration of CBCT imaging and image registration in the RT domain, particularly, the ART. Finally, it discusses the limitations of treatment by this latter and explains how research is being oriented towards the generation of corrected CBCT images for dose calculation in ART;

Chapter 2 reviews the different CBCT correction approaches available in literature and compares the results of their application on several cases. It also discusses the advantages and limitations of each approach. Finally, it proves the choice of the used approach in this thesis;

Chapter 3 presents two contributions, the first is a preliminary work consisting of the evaluation of different CT to CBCT registration algorithms in terms of their accuracy and computation time. In the second contribution, the proposed correction approach is presented and based on the results of the performed tests, the impact of the chosen algorithms on the correction accuracy is assessed;

Chapter 4 focuses on the optimization of the previously proposed approach by hybridizing it with another one. The new developed approach is referred to as hybrid, because it applies consecutively two correction approaches and attempts to improve the HU distribution in the CBCT images obtained from the previously used method.

Chapter 5 presents the fourth contribution that aims to generalize the use of the hybrid approach in order to minimize the workload requirements in ART. The main idea is to include the notion of inter-patient image registration that allows investigating the CT scans already available in the archive for the correction of CBCT images rather than acquiring new CT images for each patient.

Chapter 1

Clinical and Technical Notions

1.1 Introduction

Radiotherapy (RT), also known as radiation therapy, is a field that has rapidly advanced over the last three decades, thanks to the breakthrough of multi-modal imaging systems and the development of computer technology and treatment machines. These technological advances has allowed to treat very complicated target volumes while sparing the adjacent normal structures. In this chapter we started by describing the standard workflow of RT, introducing the main concepts frequently used in clinical routine. Then, we discussed the evolution of RT techniques focusing on the reasons behind the integration of modern imaging modalities and image processing tools. Finally, we focused on the latest treatment technique, its limitations and the main proposed solutions that aim to increase its performance.

1.2 External radiotherapy

External radiotherapy is a treatment technique that aims to destroy cancer cells using high-energy ionizing radiation produced by an external source. Depending on the tumor type, its location, size and stage, it can be curative, palliative or symptomatic. Curative radiotherapy is the most common and its main purpose is to sterilize the tumor and preserve as possible the surrounding normal critical structures known as organs at risk (OARs).

1.2.1 Workflow of radiotherapy

Generally, the workflow of external radiotherapy goes through different complex processes starting from the data acquisition to the treatment delivery as illustrated

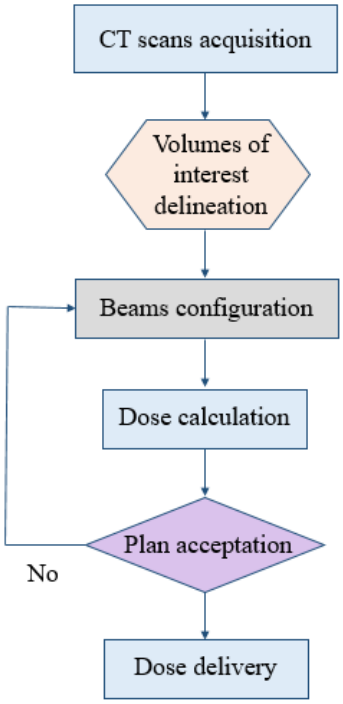

Figure 1.1: The workflow of external radiotherapy.

in Figure 1.1. Each part of the workflow can be described as follows:

1.2.1.1 CT scans acquisition

The 3D planning begins with the acquisition of CT scans, called planning CT (pCT), for the patient in the treatment position. Numerous immobilization devices could be used to help duplicate the same position throughout the treatment course.

1.2.1.2 Definition of target volumes and OAR

From the acquired CT scans, radiation oncologists define target volumes and OAR according to a comprehensive guidelines provided by the International Commission on Radiation Units and Measurement reports 50, 62 and 83 [13, 14, 15].
For the target volume delineation, several concentric volumes are described (Figure 1.2). First, the extent of malignant cells, including any involved nodes, is called the gross tumor volume (GTV). Next, a margin arround the GTV is added to account for potential local-regional subclinical extension, and is called the clinical target volume (CTV). The GTV and CTV are based only on anatomic and biological considerations. Another volume, called the internal target volume (ITV), taking into account variation in the position, shape and the size of the CTV was lately defined [14]. The final volume is the planning target volume (PTV). This volumetric expansion

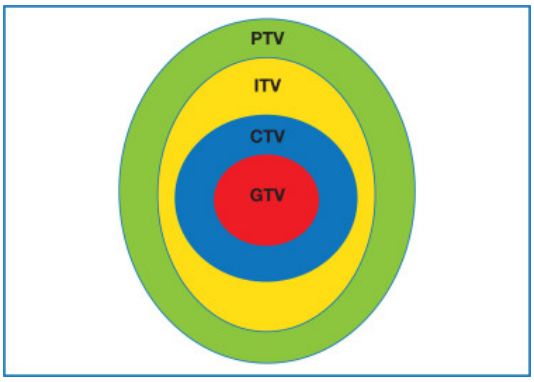

Figure 1.2: Graphical representation of the volumes of interest, as defined in ICRU reports 50 and 62 [16].

takes into account the uncertainties of the CTV position from day-to-day, the patient movement (e.g., breathing), and differences in the patient positioning.
For the OAR delineation, all normal tissues surrounding the tumor and may receive a significant dose from the treatment plan are taken in consideration [17, 18].

1.2.1.3 Treatment planning

Once the geometrical information concerning the shapes of the volumes of interest (VOIs) is complete, medical physicists determine the beams arrangement (number of beams, weights, shapes, orientations, energies, use of beams modifiers,...) that allows the generation of acceptable treatment plan respecting the dose prescription provided by the radiation oncologist. The dose calculation is performed according to the ICRU guidelines and it should be normalized at the center of PTV to 100% with the dose elsewhere within the PTV being in the range $100 \pm 5\%$.
The acceptance of the treatment plan is based on qualitative and quantitative evaluation of the dose distribution; the qualitative evaluation consists of integrating the dose distribution in two or three-dimensional (2D, 3D) patient model (Figure 1.3.a), presented in the observer's view, which gives a fast impression about the global dose distribution. It should be ensured that the target volume is covered by the 95% isodose line. For the quantitative evaluation the dose-volume histograms (DVHs) present a powerful parameter that enables getting a precise information about the percentage of dose received by a particular volume (Figure 1.3.b). 95% of the PTV should receive at least 95% of the prescribed dose while for the OARs a set of tolerances should be respected.
Another statistical parameters as the minimum, maximum and the mean dose (D_{min}, D_{max} and D_{mean}) can be also examined.

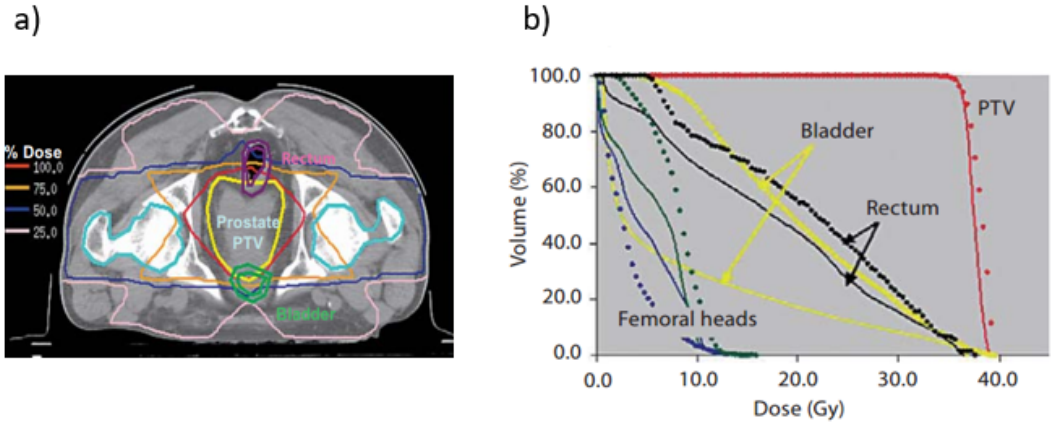

Figure 1.3: Example of treatment plan evaluation for prostate cancer by the verification of the isodose distribution (a) and the dose-volume histograms (b) [19].

1.2.1.4 Dose delivery

This process aims to correctly transfer the planned irradiation technique to the patient. So that, it is critically important to position the target volume under the treatment machine as during the acquisition of CT scans. First, the skin marks made at the simulation session are aligned to the room-mounted positioning lasers. Then, the in-room imaging systems are used to verify the position of the target volume and the OARs.

1.2.2 Evolution of radiotherapy techniques

In the past two decades, the use of modern imaging modalities, efficient 3D treatment planning systems and developed treatment machines has allowed the appearance of more sophisticated treatment techniques such as the 3D conformal radiotherapy (3D CRT), intensity modulated radiotherapy (IMRT), volumetric modulated arc therapy (VMAT), image guided radiotherapy (IGRT) and adaptive radiotherapy (ART). The application of these techniques in clinical practice is based on the standard workflow described in the section 1.2.1; however, some significant differences exist, particularly in the treatment planning and dose delivery processes. This section focuses on the description of the evolution of radiotherapy from the 3D CRT to the ART by explaining in details the contribution of each technique to improve the dose targeting to the tumor and spare the normal tissues.

1.2.2.1 3D Conformal radiation therapy

3D-CRT is a technique where the beams of radiation used in treatment are shaped to match the tumor [20]. In its beginning, the beam shaping was performed with

metal blocks, called "cerrobend" blocks, which allowed to introduce fields with irregular shapes and conform the dose distribution closely to the tumor. Individual realization of these blocks turned out to be time-consuming and expensive; therefore, great progress in 3D CRT was achieved by the development and the integration of computer-controlled multileaf collimator (MLC) in the linear accelerators (Linac).

With this technology, the delivery of dose distribution with high conformity became possible; however, conformal and homogeneous dose distribution can not be obtained in all cases. This is particularly true for complex-shaped target volumes, especially, the concave-shaped ones that remained a challenging task.

1.2.2.2 Intensity modulated radiation therapy

To tackle the problem of complex-shaped target volumes, intensity modulated radiation therapy was introduced into clinical use. As its name implies, this technique allows the modulation of the intensity or fluence of multiple radiation beams incident from different directions, so that each beam delivers intentionally non-uniform dose to the target. The superimposition of such beams results in more conformal dose distribution and allows for lower doses to OARs as seen in Figure 1.4 [20, 21].

Compared to the 3D-CRT where the number, position, shape and intensity of used beams are configured manually; the IMRT is based on inverse planning concept that begins the treatment planning with the ideal dose prescription and ends with the IMRT radiation beams providing more degree of freedom to optimize the plan [22].

Despite the clear benefits of IMRT in terms dose escalation and normal tissue

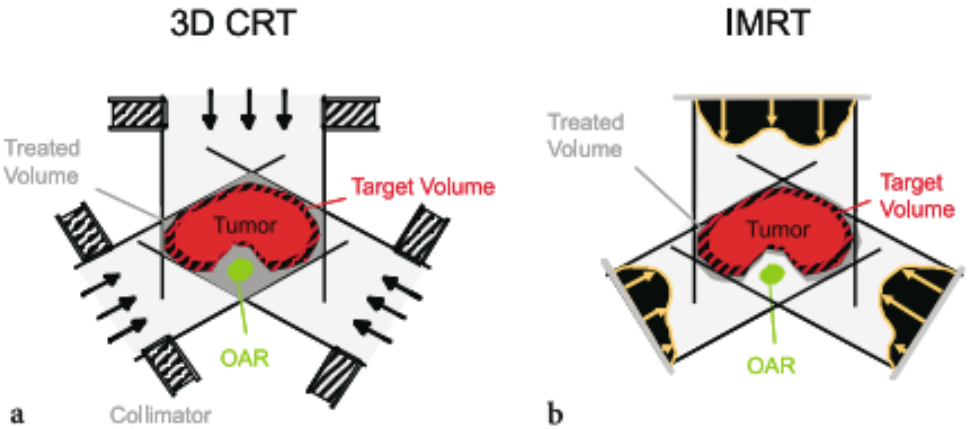

Figure 1.4: Comparison of the principals of 3D-CRT and IMRT. In (a), the use of uniform fields yields a convex dose distribution that include the OARs; while in (b), the combination of multiple beams produces the desired dose coverage of the target volume and sufficient sparing of OARs [21].

sparing, there are some limitations. First, the use of multiple gantry angles, fixed fields and differential beam intensity increases the treatment delivery time which may impact patient reproducibility and increase intrafraction organ motion variability. Second, the use of IMRT is an increase in low dose radiation to non-target tissue (i.e., integral dose) due to higher monitor unit (MU) requirements for IMRT delivery and increased number of beams which raises some concern regarding the risk of secondary radiation-induced cancer. Finally, all uncertainties related to daily inter-fraction positioning, displacement and distortions of internal anatomy and intra-fraction motion of tumors and normal tissues during the course of treatment, may also limit the applicability and efficiency of IMRT.

1.2.2.3 Volumetric modulated arc therapy

Arc therapy has emerged as a technique to address some of the limitations of fixed fields treatments. In contrast to fixed field IMRT, arc therapy incorporates rotation of the Linac gantry while the beam is on [23]. In most cases the patient is treated from all angles in one or more 360-degree rotations (Figure 1.5).

The major conceptual advantage of VMAT over standard IMRT is that since the

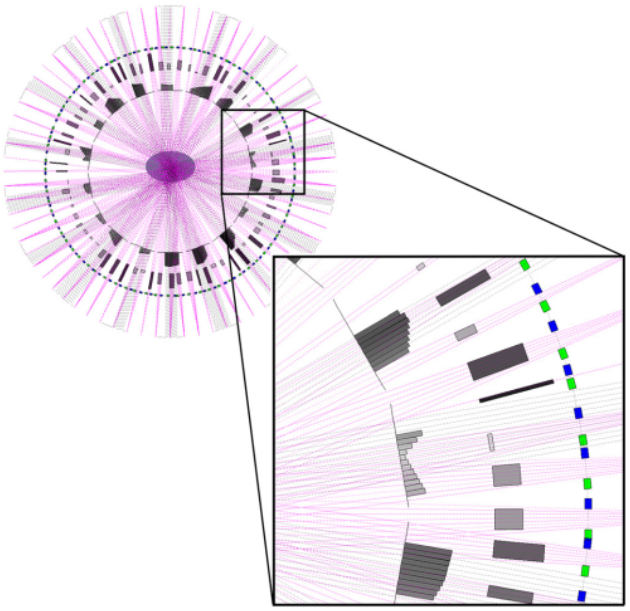

Figure 1.5: Principal of VMAT. The moving source rotates along a circle indicated by the outermost circle in the diagram. The green and blue rectangles represent the position of the leaves at each gantry angle. The next circle shows the segment weighting plotted as a grey rectangle of varying height and intensity which both vary in proportion to the segment weighting. The next circle in represents the reconstructed maps from re-sorted parallel rays shown with the associated parallel rays. It can be seen that these re-sorted rays have an intensity modulation. [24].

rotation of the source is performed around the patient, all angles are available to deliver radiation to the target volume while avoiding normal tissues, and time is used efficiently because the radiation delivery does not stop in between different angles. Furthermore, the decreased monitor unit required for this technique can result in a lower dose to normal tissues.

1.2.2.4 Image guided radiation therapy

As mentioned previously, internal organs motion, patient's shapes changes and patient's setup errors may limit the efficiency of IMRT or VMAT and result in under-dosage of target volume or over-dosage of OARs. Therefore, optimal treatment delivery relies on accurate image guidance.

Usually, image guidance refers to the use of different imaging systems in order to detect and correct random and systematic errors that occur before or during the treatment delivery. Several imaging modalities such as kilovoltage cone-beam CT (kV-CBCT), megavoltage cone-beam CT (MV-CBCT), magnetic resonance imaging (MRI) and positron emission tomography (PET) can be used to acquire information on the patient's body position or the position of the target organs, including bone structures, soft tissues, or a tumor itself [21, 25, 26].

With these modalities, the image guidance intervention in the workflow of radiotherapy appears in three main levels that could be summarized as follows:

- **Image guidance for delineation:** CT scans are the standard imaging modality in radiation treatment planning since it combines high geometrical accuracy with a measure of electron density which enables dose calculations. However, in comparison with MRI, the quality of CT scans is inferior in the detailed definition of soft tissues, particularly, microscopic tumor extensions. Therefore, coupling MRI with CT scans should be applied for an accurate delineation of volumes of interest. Furthermore, the use of biological imaging as PET provides additional information about the proliferating areas of the tumor and allows differentiating areas of biological importance within the boundaries of target volumes [27].

- **Image guidance for patient's setup:** In-room imaging systems as the MV-CBCT and kV-CBCT are currently used to refine the patient's position under the treatment machine and control the evolution and the localization of the target volume during the treatment. Both of these modalities provide volumetric images in single revolution of the gantry using the megavoltage treatment source for the MV-CBCT and kilovoltage source for the kV-CBCT.
  The benefits of kV over MV imaging for the patient's setup include not only lower

dose exposure, but also high quality of kV-CBCT images which allows reduced observer variability and consequently better reproducibility of the desired position [28].

- **Image guidance for treatment verification:** Online volumetric pre-treatment imaging, as kV-CBCT, serves as an ideal method for target verification at the time of treatment due to its ability to describe anatomical distribution with high contrast. Based on geometrical measures, it allows estimating tumor regression throughout the treatment. Currently, PET scans are also taken to estimate the degree of tumor response [21].

1.2.2.5 Adaptive radiation therapy

Although IGRT gives clinicians the possibility of better patient's positioning during the treatment by aligning the beam with the target before radiation, a simple repositioning is insufficient to correct shape variations in target or nearby critical structures. The more complex correction is usually performed by replanning: a process called ART, which includes the modification of initial plan to adapt to changes in target volume or OARs. As shown in Figure 1.6, the ART process goes through four complex and time consuming steps: (1) initial planning, (2) image guidance for patient's setup, (3) repeated imaging and adaptive planning and (4) treatment delivery. In theory, these steps can occur in clinical routine on three time scales:

- Offline adaptation. The plan is re-optimized between fractions in case of

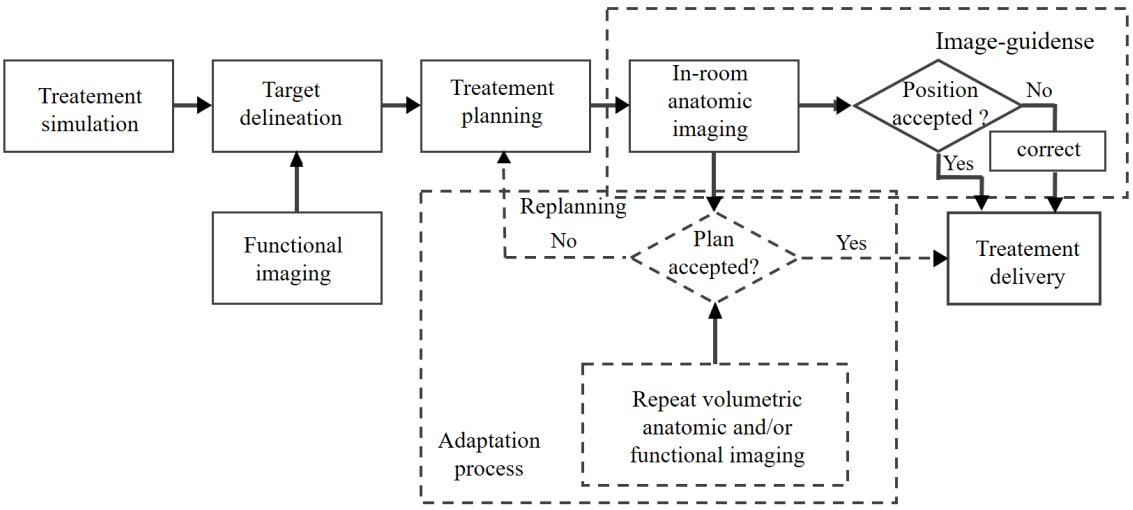

Figure 1.6: Process of image-guided adaptive radiotherapy [29].

clinically significant variations in the patient's anatomy (weight loss, tumor shrinkage,...)[30, 31].

- Online adaptation. In this case, the re-optimization is applied just before irradiation. In-room imaging are often used to detect and correct systematic and random errors [32, 33, 34].

- Real time adaptation. The plan is re-optimized during irradiation by adapting the beam according to the target position (tracking) [35, 36] or by interrupting the irradiation when the target moves outside the planned area (gating) [37].

To date, the implementation of online strategies in clinical practice is challenging because patients must remain immobilized on the treatment couch while waiting for ART correction. Moreover, these strategies could provide greater treatment precision but at the cost of substantial increase in physician and stuff effort and treatment time. Several researches have converged to the full automation of the ART workflow in order to reduce the workload requirements for online ART. The main focus was attributed to the image guidance and the replanning steps. Since IGRT is mainly based on the comparison of the information provided by the daily acquired images, usually kV-CBCT, and the initial pCT images, the notion of automatic image registration process has been appeared. In addition, as the replanning process requires the need for new pCT images acquisition which may pose a health concern to patients, the idea of investigating the daily kV-CBCT images not only for guidance but also for treatment planning have seen a special interest.

In the two following sections, the role of image registration and daily kV-CBCT images as base for treatment planning in ART and its limitations are described in details.

1.3 Integration of image registration process

Notations

I_F	Fixed image
I_M	Moving image
$\overline{I_F}$	Average intensity of I_F
$\overline{I_M}$	Average intensity of I_M
x_i	Voxel number i
N	Total number of voxels in an image
T	Transform
μ	Registration parameters
$\widehat{\mu}$	Registration results
ζ	Cost function
$H(A) = -\int p_A(a) \log p_A(a) da$	Entropy of a random variable
$H(A,B) = -\int p_{AB}(a,b) \log p_{AB}(a,b) dadb$	Joint entropy of two variables
$p_A(a)$, $p_B(b)$	Marginal discrete probabilities

Image registration plays a central role in various stages of image guidance in ART. It is a process of establishing spatial correspondences across two images of the same scene (in medical image registration: the same anatomical region) acquired at different times by the same or different imaging modalities to obtain a complete information [29]. The purpose is to determine a geometric transformation (translation, rotation or deformation) that maps points from one image (moving image) to their homologous points in another image (fixed image). In this way, images can be combined and fused on a voxel-by-voxel basis and differences between anatomical structures can be quantified for image guidance and follow up [21].

The general image registration process can be illustrated in Figure 1.7. In this process, the registration is considered as an optimization problem which has to be solved throughout the minimization of a cost function using an iterative way. Commonly, this problem is formulated as follows:

$$\widehat{\mu} = arg \min_{\mu} \zeta \ (\mu; I_F, I_M) \tag{1.1}$$

From the Figure 1.7 and Equation 1.1 several components can be recognized:

Moving image: is the image which will be deformed to correspond to the fixed image;

Fixed image: is the image from which deformations will be computed to be applied

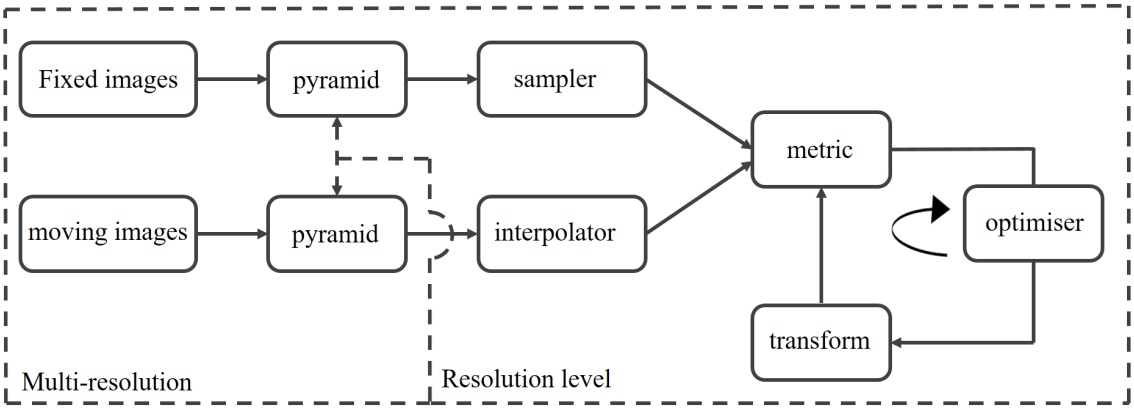

Figure 1.7: Basic components of an image registration framework [38].

to the moving image;

Similarity measure: is, by definition, the metric that quantifies the degree to which a pair of imaging studies are aligned (or mis-aligned). Using standard optimization techniques the transformation parameters are manipulated until this metric is minimized (or maximized). Most registration metrics in use presently can be classified as either geometry-based or intensity-based. Geometry-based metrics make use of features extracted from the image data such as anatomic or artificial landmarks (points) and organ boundaries (contours or surfaces). However, the definition of such features requires the use of accurate segmentation techniques. Intensity-based (voxel-based) metrics use the numerical gray-scale information directly to measure how well two images are registered. Several mathematical formulations are used to measure this similarity; four of the most common are described below:

1. **Mean Squared Difference (MSD):** is a simple and easy-to-apply metric. It is computed as the average squared intensity difference between the fixed and the moving images. Its formula is given by:

$$MSD(I_F, I_M) = \frac{1}{N}\sum_{i=1}^{N}(I_F(x_i) - I_M(x_i))^2 \tag{1.2}$$

   This metric is effective for registering two images have essentially identical intensities (Mono-modal images)[39, 40].

2. **Normalized Correlation Coefficient (NCC):** is one of the common used metrics. it determines a linear relation between the fixed and the moving images. It can be formulated as follow:

$$NCC = -\frac{\sum_{i=1}^{N}(I_F(x_i) - \overline{I_F})(I_M(x_i) - \overline{I_M})}{\sqrt{\sum_{i=1}^{N}(I_F(x_i) - \overline{I_F})^2 \sum_{i=1}^{N}(I_M(x_i) - \overline{I_M})^2}} \tag{1.3}$$

This metric is more complex, but offers greater flexibility, as it can be applied to multi-modal images[41, 42].

3. **Mutual Information (MI):** as the name implies, this metric is based on the information content of the fixed and the moving images and is computed directly from the probability distribution of these images intensities. It is given by:

$$MI(I_F, I_M) = H(I_F) + H(I_M) - H(I_F, I_M) \tag{1.4}$$

This method is more complex than either MSD or NCC, but offers even more flexibility and is often the metric of choice for multi-modal images[43, 44].

4. **Normalized Mutual Information (NMI):** is a normalized version of the MI and it is given by:

$$NMI(I_F, I_M) = 1 + \frac{MI(I_F, I_M)}{H(I_F, I_M)} = \frac{H(I_F) + H(I_M)}{H(I_F, I_M)} \tag{1.5}$$

Transform: the fundamental task of image registration is to find the geometric transformation, T, that maps the coordinates of a point in the moving image to the coordinates of the corresponding point in the fixed image. In general, a number of parameters (often referred to as degrees of freedom (DOFs)) is required to determine the transformation [45]. This number depends on the form of T, which in turn depends on the clinical site, clinical application and the modalities involved. According to its degree of freedom, transformations are categorized into three types:

1. **Rigid transform:** a rigid registration (RR) allows to treat the image as a rigid body, which can translate and rotate. It can be described by the following formula:

$$T_\mu(x) = R(x - c) + t + c \tag{1.6}$$

With R a rotation matrix, c the center of rotation and t the translation.

2. **Affine transform:** affine transformation can be seen as the extension of rigid transformation. It is composed of rotations, translations, scaling, and shearing. Its formula is given by:

$$T_\mu(x) = A(x - c) + t + c \tag{1.7}$$

Where the matrix A has no restrictions.

3. **Deformable transform:** a deformable image registration (DIR) is often used in sites where rigid or affine transformations are not powerful enough to achieve acceptable alignment of anatomical structures. One class of deformation model is called B-spline, which is a curve that interpolates points in space based on a set of control points. A set of parameters associated with each control point defines the exact shape of this interpolation. The number and location of control points determine the extent of deformation that a spline can express. The formula describing this deformation is given by:

$$T_\mu = x + \sum_{x_k \in N_x} p_k \beta^3 (\frac{x - x_k}{\sigma}) \tag{1.8}$$

With x_k the control points, $\beta^3(x)$ the cubic multidimensional B-spline control points spacing and N_x the set of all control points within the compact support of the B-spline at x.

Interpolator: during optimization an interpolator is used to evaluate intensity at non-voxel positions. Different interpolation methods including nearest neighbor, linear and N^{th} Order B-Spline interpolators exist. The most used one is The N^{th} Order B-Spline Interpolator; for which the higher the order the better the quality.

Optimizer: an optimizer is the element that aims to find the optimal metric value giving the most accurate alignment. Gradient descent (GD) is the most common one and it is defined as follows:

$$\mu_{k+1} = \mu_k - a_k g(\mu_k) \tag{1.9}$$

with $g(\mu_k) = \partial\zeta/\partial\mu$, the gradient at the position μ_k and $a_k = \dfrac{a}{(k+A)^\alpha}$ the decaying function where: $a > 0, \quad A \geq 1 \quad and \quad 0 \leq \alpha \leq 1$ are user defined constants.

There is also a more advanced version of the standard GD called the adaptive stochastic gradient descent (ASGD); it allows an automatic calculation of the parameters a, A and α and tends to be more robust.

Samplers: an image sampler defines the way to select a subset of voxels for the metric calculation. It should be assumed that the loop covers all voxels in the fixed image. The subset can be selected in different ways: random, on a grid,... etc.

Pyramid: a pyramid allows starting the registration from images with low complexity (smoothed or down-sampled) to images with high complexity.

Figure 1.8: Illustration of a linac-mounted kV-CBCT system.

1.4 Investigation of CBCT images

As sight previously, significant (non-rigid) changes in the patient's anatomical structures can be quantified only by treatment guidance based on the comparison of the initial pCT and the daily acquired images. One of the most widely used imaging technique for treatment guidance, being also the one under consideration in this thesis, is CBCT. This section serves to describe this imaging modality in details with emphasis on its imaging quality and its main limitations.

1.4.1 Acquisition system

A CBCT imaging system consists of a kilovoltage (kV) X-ray source and flat panel detector mounted orthogonally to the linear accelerator gantry axis, on the opposite side of the patient with respect to the imaging source (Figure 1.8) [46]. The rotational axes are parallel to the treatment table and pass through the center of the target. When the system rotates, planar projections are recorded from different angles. Then, a 3D image of the patients anatomy is reconstructed from all projections [17].

CBCT has the particularity of using a cone-shaped beam, unlike the CT where the beam is fan-shaped as shown in Figure 1.9. This cone-beam geometry makes it possible to acquire tens of tomographic sections for a single rotation of the CBCT gantry compared to the acquisition of individual consecutive sections with a conventional CT.

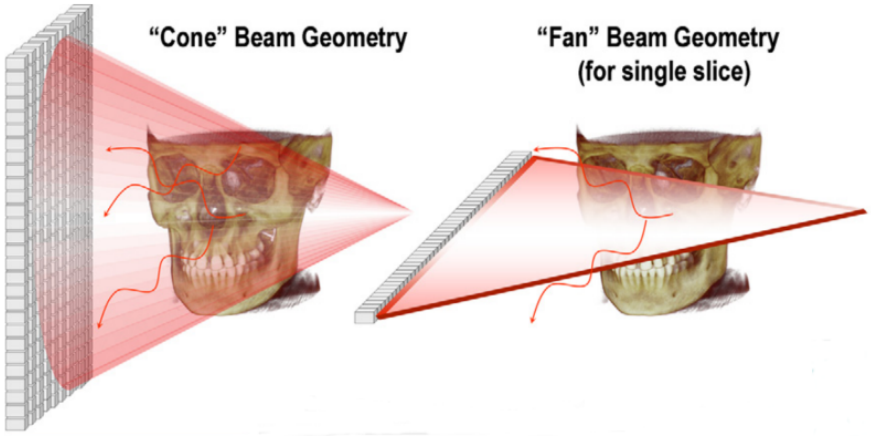

Figure 1.9: Schematic representation of the conventional, fan-beam geometry and the cone-beam geometry [17].

1.4.2 CBCT image quality

Although image reconstruction principals of CBCT images is similar to that of pCT images, the CBCT image quality is very different (Figure 1.10). The fact that the patient is imaged using a cone-shaped beam that covers a large section (large field of view(FOV)) increases the amount of detected X-ray scatter resulting in a multitude of artefacts that reduce their quality compared to the pCT images. Here, a brief overview of these different artefacts and their sources is presented.

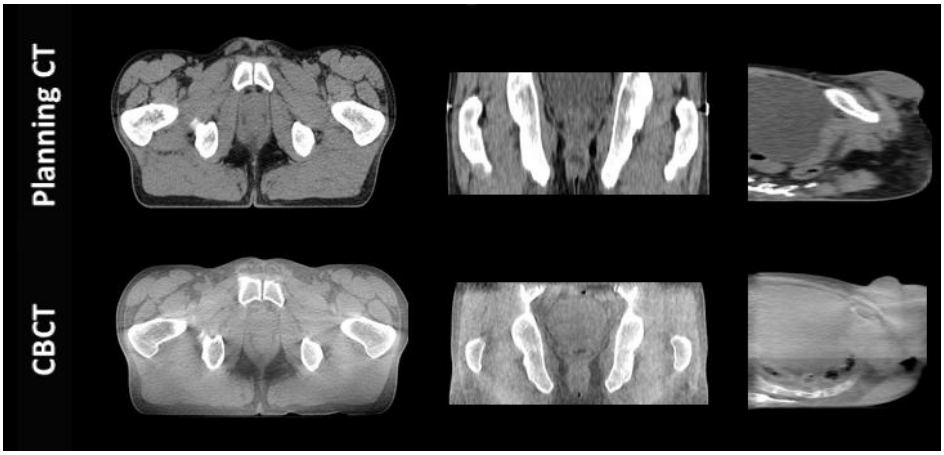

Figure 1.10: pCT and CBCT for the same patient (axial, coronal and sagital views) displayed using the same window level.

1.4.2.1 Cupping artefacts

Cupping, so called shading, artefacts are the most prominent in CBCT imaging. They come out as an apparent decrease in density towards the center of homogeneous

objects imaged on a CBCT system (Figure 1.11). These artefacts are due to the high scatter conditions found in CBCT imaging, where the large 2D detector panel acquires signal from scattered photons as well as primary photons. Furthermore, differential attenuation of polyenergetic x-ray beams (known as beam hardening) adds to the cupping artefact, although at smaller magnitude than the scattered photons [47].

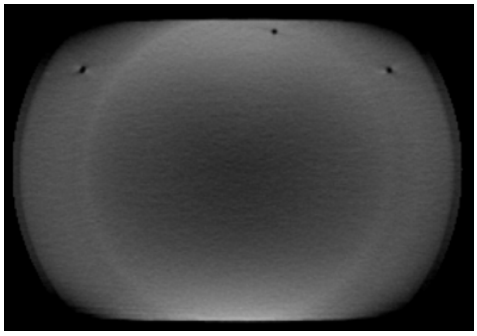

Figure 1.11: CBCT image of a homogeneous phantom which displays the cupping artefact commonly found in CBCT imaging. The central part of the phantom appears to be less dense than the rest of the phantom, and this effect is a combined result of scattered photons and beam hardening [47].

1.4.2.2 Streaking artefacts

Streaking artefacts, often termed "missing values artefacts", are another effect of high scatter condition in CBCT imaging. They appears if the object under study contains highly absorbing material, e.g. bone or prosthetic gold restorations. In this case, the high density material causes an abrupt change in the scatter to primary ratio (SPR), and the soft tissue behind bony anatomy may appear to have a lower density than in other regions of the same image (Figure 1.12).

1.4.2.3 Radar artefacts

Radar artefacts are pronounced, if the CBCT scanning isocenter located near the surface of the human body (Figure 1.13). These artefacts are due to non-instantaneous readout of the 2D flat panel imager used in CBCT imaging for IGRT showing themselves as a bright circular lines extending from the patient surface inside the patients body. Similar effects can be observed around bony anatomy in other CBCT acquisitions.

1.4.2.4 Aliasing artefacts

Aliasing artefacts in CBCT imaging are mainly related to two factors: the size of the detector elements, i.e. the pixel size, and the cone-beam geometry. First, in order

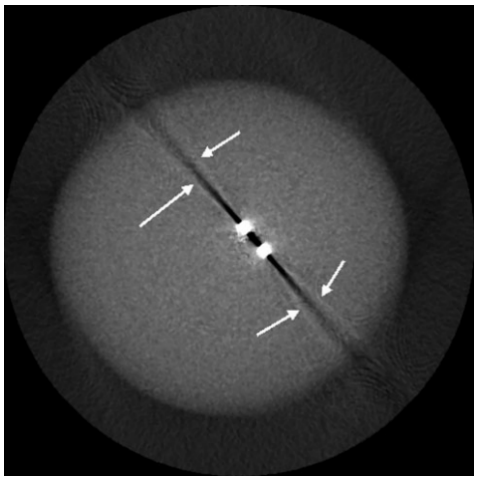

Figure 1.12: CBCT image of a homogeneous phantom with dense implements. Typical thin lines tangent to the sharp edges appear in the direction of the beam [48].

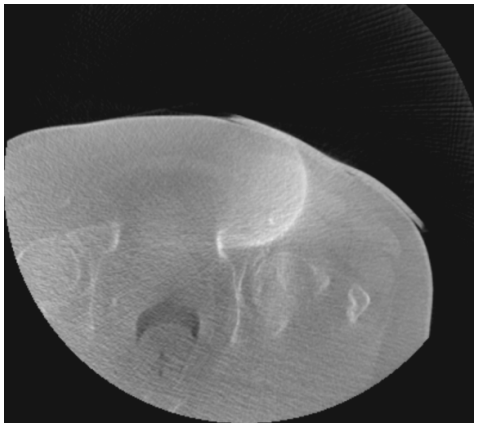

Figure 1.13: Example of CBCT image displaying the radar artefact as a bright circular line extending from the patient surface inside the patients body. Similar effects can be observed around bony anatomy in other CBCT acquisitions [47].

to completely reconstruct a continuous signal, the sampling frequency (represented by the number of pixels per area) must be higher than twice the highest frequency in the signal. Thus, violating this condition may raise the problem of undersampling [49]. Second, owing to the divergent shape of the cone beam, the voxels close to the source will be traversed by more rays than those close to the detector (Figure 1.14). Hence, these artefacts manifests as line patterns commonly diverging towards the periphery of the reconstructed volume (Figure 1.15).

1.4.2.5 Ring artefacts

Ring artefacts are more pronounced when homogeneous media are imaged. Owing to the circular trajectory and the discrete sampling process, these artefacts appear as concentric rings centered around the location of the rotation axis (Figure 1.16). In a

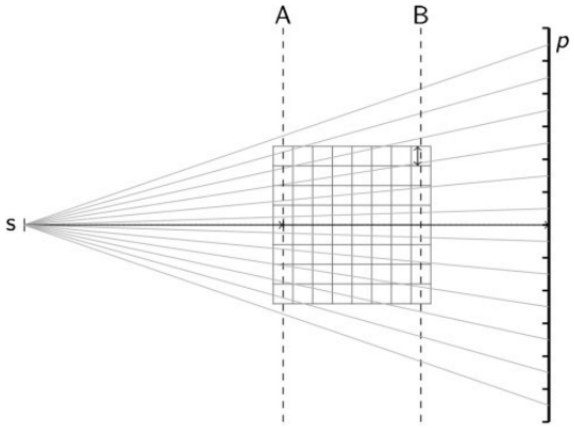

Figure 1.14: One source of undersampling resulting in aliasing errors in CBCT is the cone divergence itself. Obviously, the slice A of the volume nearest to the source collects many more rays per voxel (as measured on the detector pixels, p) than slice B, which is closest to the detector. The number of rays per voxel linearly decreases with the distance of the slice from the source [50].

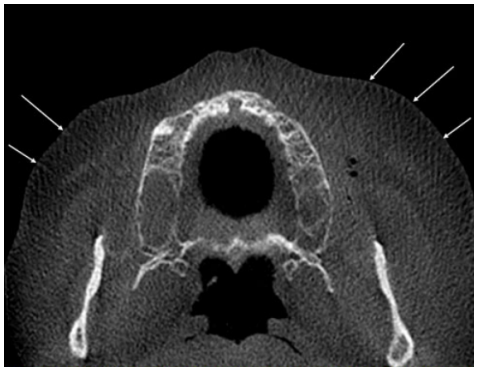

Figure 1.15: Typical aliasing patterns in CBCT data sets. The lines (arrows) diverge from the centre towards the periphery and are most probably caused by the undersampling owing to the cone beam geometry.

broader sense, ring artefacts could also be allocated to the group of aliasing artefacts.

1.4.2.6 Motion artefacts

CBCT scanners are mounted on the linac gantry that does not rotate more than one revolution per minute. A result of the slow CBCT acquisition following from the gantry rotation speed is that CBCT images are prone to motion artefacts, e.g. patient's breathing, cardiac motion or intestinal gas. The general problem is quite easy to explain for patient motion artefacts (Figure 1.17). If an object moves during the scanning process, the reconstruction does not account for that move since no information on the movement is integrated in the reconstruction process. Hence, the lines along which the

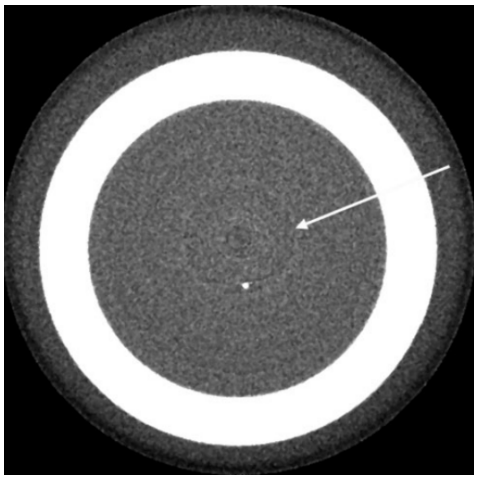

Figure 1.16: Example of CBCT image of a homogeneous phantom displaying ring artefacts (arrow) centred around the location of the axis of rotation. As with many other artefacts, they are most clearly visible in axial slices, i.e. in beam direction[50].

Figure 1.17: Example of a typical double contours (arrows) induced by patient movement during the acquisition process of the projection images.

backprojection takes place do not correspond to the lines along which the attenuation had been recorded, simply because the object has moved during the acquisition.

1.4.3 Towards ART based on CBCT images

The fact that CBCT images suffer from high amount of artefacts did not limit its use for image guidance alone, but it opened a new research axes looking for the investigation of CBCT images as a basis for treatment adaptation, particularly, as an alternative to the acquisition of new pCT in case of anatomical changes [51, 52].

The key limitation in such application is the lack of hounsfield unit (HU) accuracy

caused by all of the above mentioned artefacts. Therefore, many studies proposed different techniques to overcome this limitation and ensure suitable HU distribution for an accurate dose calculation. These techniques include: the integration of physical instruments as anti-scatter grids to reduce the impact of scatter on the CBCT reconstruction quality [10, 53], scatter measurement based on the imaging system modeling (simulation) [11, 54], calibration of CBCT images using phantoms [12, 55, 56] and finally the use of image processing techniques that allow correcting the HU distribution in the CBCT images based on that provided by the pCT images [5, 6, 57].

Most of research converges to the use of image processing techniques due to their efficiency and rapidity compared to the integration of hardware or the use of simulation. These techniques are classified and reviewed in detail in the next chapter with discussion of their main advantages and limitations.

1.5 Conclusion

This chapter presented the technical and clinical notions widely used in the RT domain. The main goal was to provide a basic knowledge to understand the rational behind the choice of the problematic in this thesis. It focused on the description of the evolution of RT from its simplest forms to its more complicated ones which are the ART techniques. Actually, the growing use of in-room imaging, especially CBCT systems, with the integration of image registration tools has highlighted the idea of implementing online ART techniques in the clinical routine. Reaching this goal was associated with the appearance of increasing number of published works proposing the investigation of CBCT images as a base for treatment planning instead of acquiring new pCT images. For deep understanding, the next chapter presents these works and reviews the existing techniques that aims to generate appropriate CBCT images for dose calculation in the context of online ART.

Chapter 2

Literature review

2.1 Introduction

Cone-beam CT imaging is now fully integrated in radiation therapy; it can be considered as a powerful tool for improving tumor targeting and dose delivery to normal tissues. However, these images suffer from a reduced contrast due to the increased amount of scatter which limits the use of CBCT images directly for dose calculation [4]. For that reason, several authors proposed promising techniques to enhance the quality of CBCT images. This chapter provides a state of art of CBCT image correction techniques. The main goal is to review briefly the different correction methods available in literature and compare the results of their application for the treatment of several patients by ART.

2.2 Classification of CBCT correction approaches

So far, four types of CBCT correction approaches have been evaluated in literature: physics-based, calibration-based, pCT-based and deep learning-based approaches. Each type is detailed in this section.

2.2.1 Physics-based approaches

2.2.1.1 Use of physical instruments

This technique is the most obvious and it can be defined as the use of anti-scatter grids or beam blockers to prevent the influence of scattered irradiation on the CBCT image quality.

In 2007, Léterneau et al [58] assessed the impact of post-patient anti-scatter grid in combination with a non linear scatter correction on the CBCT number accuracy.

Testing of the complete process was performed on phantoms with assessment of dosimetric accuracy based on 2D γ-analysis. The results showed that the cupping artefact was reduced from 30% to 4.5%. Also, the CBCT number accuracy was improved in water of about $\pm$20 HU and in bone and lung to within $\pm$130 HU. γ-analysis showed that 97 to 99% of the pixels of radiochromic films agreed with the calculated dose within 5% of dose difference or 2 mm of distance to agreement. However, this technique is limited by the fact that the use of anti-scatter grid can reject some of the scatter but serves also to attenuate the primary beam, which can result in an increase in image noise for the same dose to the patient.

In 2009, Zhu et al [59] proposed the use of another instrument which is the beam blocker usually placed between the source and the imaging object. This instrument has a strip pattern, such that partial volume can still be accurately reconstructed and the whole-field scatter distribution can be estimated from the detected signals in the shadow regions using interpolation or extrapolation. Hence, the estimated scatter may be separated from the CBCT information acquired in an open field without beam blocker. The evaluation results showed that the errors in HU were reduced from about 350 HU to bellow 50 HU when applying this method on Catphan600 phantom, while when using an anthropomorphic phantom, the error was reduced from 15.7% to 5.4%. Despite these findings, the need for two scans to measure scatter and acquire image data with and without beam-blocks is a limiting factor due to the additional dose to the patient.

In 2010, Jin et al [60] proposed the same method as [59] but they acquired the imaging data simultaneously from the grid interspace regions during scatter measurement. They reported that the proposed technique reduced the streak artifact index from 58% to 1% in comparison with the conventional CBCT. It also improved CT number linearity from 0.880 to 0.998 and the contrast-to-noise ratio (CNR) from 4.29 to 6.42. Even though, this technique remains limited by the grid parameters as the septa width that affect the image quality.

2.2.1.2 Simulation of the imaging system

This technique consists of the scatter modulation using simulation methods.

In 2006, Jarry et al [61] used Monte Carlo (MC) simulation to predict scatter distribution in CBCT images. The study was performed on a cylindrical water phantom and an anthropomorphic head phantom and for evaluation purposes contrast and profile measurements were obtained for the scatter corrected and non-corrected images. An improvement of 3% for contrast between solid water and a liver insert and 11% between solid water and a Teflon insert were obtained and a significant reduction in cupping

and streaking artifacts was observed. However, simulation time was about 430 hours which is a significant amount of time.

In 2008, Mainegra-Hing et al [62] developed a new MC simulation code for CBCT scatter computation. They proposed the use of a variance set that allowed increasing the simulation efficiency by a factor of 4000. They also proposed a denoising process for the computed scatter distribution that reduced the simulation time by another factor of 10. Such that the calculations described in [61] would be 39 seconds instead of the 430 hours reported. However, since results reported in their work can be considered only preliminary, extensive benchmarking of the algorithm with real CBCT images, and a better model of the X-ray source and detector array is still needed.

In 2014, Thing et al [63] studied two simulation geometries with two different x-ray sources and variant user input parameters to take into account the impact of the source geometry not addressed in [62]. They reported that optimizing the input parameters to the specific simulation geometry can improve scatter calculation efficiencies by more than 4 orders of magnitude. However, this study was based on lengthy simulation and it is important to realize a few easy ways of reducing the required calculation time.

In 2015, Xu et al [54] proposed a new method for scatter estimation. In contrast to the previously cited works, they measured the scatter from the pCT images instead of scatter-contaminated CBCT images. Then, scatter signals were removed from the CBCT projections and corrected CBCT images was reconstructed. This method was evaluated in numerical simulation, phantom and real patient cases. In the simulation cases, the mean HU errors was reduced from 44 to 3 HU and from 78 to 9 HU in the full-fan and the half-fan cases, respectively. In both the phantom and the patient cases, image artifacts caused by scatter, such as ring artifacts around the bowtie area, were reduced. The limitation of this method is that scatter correction results in increased noise level in the reconstructed images and denoising algorithms are still needed.

In the same year, Bootsma et al [64] novel scatter correction method that uses a sparse number of MC simulations run concurrently with a fitting algorithm. They reported that the fitting function decreases the statistical noise in the MC scatter distribution. Also, The cupping was measured to be reduced by $32\%-88\%$ in the simulated head and pelvis phantoms. However, there are still some image artifacts remaining in the corrected images, some of which are related to the under sampling of the projection space and image lag.

In 2016, Thing et al [65] proposed another artefact correction method to tackle the problems related to the image lag, detector scatter, body scatter and beam hardening. In contrast to the previous studies where each factor was studied extensively using different phantoms, they investigated the potential increased image quality when all

artefacts sources are considered together. The study was performed on five lung cancer patients and the obtained results showed that the root mean squared difference between the reconstructed CBCT and the reference CT images was reduced by 31%. Even though, this method did not address the time consuming and difficult contouring on the noisy CBCT images.

In 2017, Thing et al [66] investigated the artefact corrected CBCT images resulted from [65] for dose calculation. They performed the study on 21 lung cancer patients with re-simulation CT images acquired during radiotherapy. For evaluation, dose comparisons were made using γ-analysis. They reported that dose distributions calculated on the artefact corrected CBCT images had a median 2%/2 mm gamma pass rate of 99.4% when compared to the reference rCT. Doses calculated on the clinical CBCT images had a median 2%/2 mm gamma pass rate of 93.1%. However, as sight previously the required time to perform the correction for each patient is not taken into consideration.

2.2.2 Calibration-based approaches

This technique can be defined as the establishment of HU-ED tables for CBCT system referring to the calibration tables of CT scans using different phantoms. The mean CT values in the phantom CBCT datasets are described by the density values of the pCT which are determined based on the relationship between CT values and physical density as specified by the phantom manufactures.

In 2008, Richter et al [52] investigated the feasibility of dose calculation in CBCT images using this correction method. Four different correction strategies to match CT values and ED in CBCT images were analyzed: standard CT HU-ED table without adjustment for CBCT; phantom based HU-D tables; patient group based HU-ED tables (pelvis, thorax, head); and patient specific HU-ED tables. Their results showed a mean difference of 564±377 HU between CT values determined from the pCT and CBCT images. For dose calculation in real patient CBCT images, the largest differences between CT and CBCT were observed for the standard CT HU-D table: differences were 8.0±5.7%, 10.9±6.8% and 14.5±10.4% respectively for pelvis, thorax and head patients. The use of patient and group based HU-D tables resulted in small dose differences between planning CT and CBCT: 0.9±0.9%, 1.8±1.6%, 1.5±2.5% for pelvis, thorax and head patients, respectively. The application of the phantom based HU-ED table was acceptable for the head patients but larger deviations were determined for the pelvis and thorax patient populations. However, this technique showed a dependency to the acquisition parameters and different HU-ED tables were required for each region to overcome this limitation.

In 2009, Hatton et al [67] assessed the impact of HU-ED calibration phantom insert composition and phantom volume on dose calculation accuracy for CBCT. They reported that the HU-ED calibration curves for the commercial phantoms diverge at densities greater than that of water, depending on the elemental composition of the phantom insert. The effect of adding scatter material longitudinally, increasing the phantom length, was found to be up to 260 HU numbers for the high-density insert. The change in the HU value, by increasing the diameter of the phantom, was found to be up to 1200 HU for the high-density insert. These differences can lead to dose differences for 6 MV and 18 MV X-rays under bone inhomogeneities of up to 20% in extreme cases. These results confirmed the dependency of the dose accuracy to the calibration phantom choice.

In 2014, Srinivasan et al [68] evaluated treatment plans based on CBCT calibrated using different phantoms. Dose calculations were performed on four different sized phantoms and to extend the study to a typical clinical situation, two prostate cases were included. The isodose distributions computed based on pCT and CBCT using the Catphan calibration curve agreed to within $\pm 1\%$ compared to that based on CBCT using the density phantom calibration curve. However, for phantoms of larger diameter, there was a pronounced discrepancy in the 50% and 60% isodose lines, with the dose difference being about $\pm 3\%$. For phantoms whose thickness is less than the cone beam scan length (16 cm) and for phantoms whose diameter is less than that of the calibration phantom, the variation in HU values is high. The effect of a change in radial diameter has a larger impact on dose calculations which confirms the results of the previous works [67].

In 2016, De smet et al [69] were interested to the application of this approach on lung cancer patients. Dose calculation was based on three different HU-ED tables determined from: a patient-specific, a general thorax-CBCT, and the standard CT HU table. They reported that the average differences between CT and CBCT dose calculations were $2\%-3\%$ for most dose metrics when the standard CT HU table was used. A better agreement was observed when a thorax-CBCT HU table was used, with differences of $1\%-2\%$. However, the creation of a HU-ED tables is more time-consuming and the gain in dose calculation accuracy should be weighed against the additional time investment.

In 2018, MacFarlane et al [56] proposed an automated patient-specific calibration method. In contrast to the previously cited works where the CBCT images were calibrated region by region, their method was based on the generation of correlation plots between pCT and CBCT voxel values, for each image slice. Then, a linear calibration curve specific to each slice was obtained by least-squares fitting and applied

to the CBCT slice's voxel values. For 15 head and neck patients, the average dose difference was $\leq 1.1\%$ and the average gamma pass rate with 3%/3mm was about 95%. However, the calibration of higher and lower densities separately is still needed to improve the performances of this method.

2.2.3 pCT-based approaches

2.2.3.1 HU mapping

HU mapping can be defined as the replacement of HU values in CBCT images by their equivalent points in CT images after the application of rigid or deformable image registration [6].

In 2007, Zijtveld et al [5] validated the use of this technique in combination with rigid registration for 5 head and neck cancer patients treated by IMRT. They compared dose distributions between CT images and CBCT images with adjusted HUs. The metrics of comparison were the dose difference plots and 3D γ-analysis. The results showed dose differences less than 1% in the majority of points and 96% of the points of 3D γ-analysis resulted in less than 1.

In the same year, Yang et al [51] evaluated the accuracy of the mapping for dose calculation. They employed four datasets including three prostate cancer patients and one lung cancer patient. For each case a set of modified CBCT (m-CBCT) was generated by mapping the electronic density (or HUs) distribution from the CT to the CBCT using B-spline DR. For the lung cases, the results showed a difference between CBCT and m-CBCT based calculations of about 5%, due to the motion artifacts, while for the prostate cases, the difference was less than 2%. Therefore, they concluded that CBCT images can be used directly for dose calculation in the absence of motion artifacts. However, the pCT cannot be replaced by CBCT images, due to their poor quality which affects the delineation of volumes of interest.

2.2.3.2 Histogram matching

The image processing by HM is a method that allows the adjustment of HU values between CBCT and pCT images using cumulative histograms. The same cumulative values are determined as:

$$CBCT(H1) = pCT(H2) \tag{2.1}$$

where CBCT (H1) represents the HU for CBCT and pCT (H2) represents the HU for pCT [70].
Figure 2.1 shows a conceptual shart of the histogram matching algorithm.

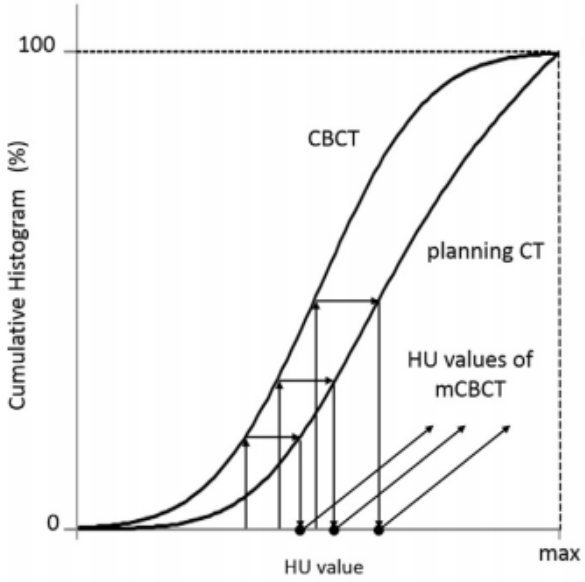

Figure 2.1: Conceptual chart of histogram-matching algorithm [70].

In 2014, Onozato et al [6] studied the feasibility of this modification for the dose calculation based on CBCT images. The HM was applied on a set of 10 prostate cancer patients datasets after a DR between CBCT and pCT images. They found that the average dose differences were less than 1%.

In 2015, Amit et al [7] developed and validated a methodology for using corrected CBCT images in an automated treatment planning for breast cancer. They used HM to correct the intensities in CBCT images. To evaluate the accuracy of the modification they compared the m-CBCT and the pCT by the average mutual information and the average sum of absolute differences. Thus, after the dose calculation, they compared the dose distribution using γ- index analysis. They observed an average mutual information of 1.0 ± 0.1 and an average sum of absolute differences of 185 ± 38, which indicate a good agreement between m-CBCT and pCT. In addition, the dosimetric comparison showed that 99.4% of the points resulted in γ less than 1.

2.2.3.3 Multilevel threshold

The MLT is a method that classifies all CBCT pixels with similar HUs into 3 or 4 different segments based on pCT [6].

In 2009, Boggula et al [71] evaluated an online adaptation plan based on CBCT images. They used as datasets, one inhomogeneous phantom and three prostate cancer patients. For each set, homogeneous structures in the CBCT images were segmented, then, reasonable averaged HU derived from pCT were assigned to each segment. Dose distribution accuracy was compared between CBCT with/without modification and

pCT using γ-analysis. They reported that dose deviations of 51% were observed when uncorrected CBCT were used, while after modification, 97% of the dose deviations were less than 3% (γ-index: 3%/3mm).

In 2012, Fotina et al [72] performed dose calculation on CBCT images of 30 patients, including patients with prostate, lung and head and neck cancer. The method of MLT was called density override technique. They considered that the patient is assumed to be comprised mostly of water, except bones or low density/air regions. These regions were extracted using an automatic segmentation algorithm based on gray values threshold. The evaluation was made by comparing dose distributions in the CT and m-CBCT using DVHs and γ-index analysis. The results showed a dosimetric difference less than 2%.

In 2014, Onozato et al [6] performed the same modification as Fotina et al [72] but they excluded water and used fat and muscle instead. In addition, they used DR to minimize the effect of organ deformation and different HUs values between pCT and CBCT. For 10 prostate cancer patients, the results showed that the combination of MLT with DR gives an average dose differences less than 1%.

In 2015, Dunlop et el [73] assessed for pelvic, lung and head neck treatment sites the accuracy of density override approaches. They applied this method in different ways: by assigning water density to the entire CBCT images, assigning of either water or bone density, assigning of either water or lung density and binning CBCT voxels into six density levels automatically. They reported that for H&N and pelvic cases the average dose-volume differences were within 1% and about 1.3% for lung cases, when using the three first assignment methods. The automatic assignment showed differences of about 0.6%, 1.2% and 1.4% for the three cites, respectively.

In 2016, Almatani et al [57] developed an automated MLT algorithm to reduce the operator time associated with the manual MLT. They aimed to increase the accuracy and the rapidity of CBCT-based dose calculation. As in the previous studies, they used as metrics of comparison, dose difference between pCT and m-CBCT and γ-index analysis. The results showed that 97.7% of points resulted in γ less than 1 (γ-index: 3%/3mm) when automated MLT where used. Furthermore, dose differences shown by MLT algorithm were about -0.46%, while those shown by the automated MLT were -1.3%.

In 2019, Giacometti et al [74] assessed the efficiency of this modification on CBCT images of 15 patients, including patients with head and neck, lung and prostate cancer. An automatic contouring tools were used to delineate 7 tissues (air, lung, adipose, muscle, soft and dense bone and metal). Then, the HU override values for these structures were determined from corresponding volumes on the patient's pCT.

The median pass rate ranges when using γ- index of 2%/0.1mm were 99.6−99.9%, 94.6−96.0% and 94.8−96.0% for prostate, head and neck and lung, respectively.

2.2.4 Deep learning-based approaches

Deep learning (DL) is, by definition, a class of machine learning algorithms that uses multiple layers to progressively extract higher level features from the raw input [75, 76]. For example, in image processing, lower layers may identify edges, while higher layers may identify the concepts relevant to a human such as digits or letters or faces.

In RT, DL was already applied to lesion detection [77] and image segmentation [78]; however, there are few studies that investigate this approach for image quality improvement.

In 2018, Kida et al [9] proposed for the first time a deep convolutional neural network (DCNN) for improving CBCT images. The main objective was to learn a direct mapping from the original CBCT to their corresponding pCT images. They reported that the root mean squared differences (RMSD) of the mean pixel values for corrected CBCT images was about 11 and 14 HU in fat and muscle, respectively. However, misalignments between paired images can lead to errors like edge blurring, deformation, and the disappearance of some anatomical structures in the improved CBCT images. In addition, the accuracy of such application is related to the training data size; therefore, handling a large data may decrease its processing speed.

In 2019, Kida et al [79] proposed the use of a conditional generative adversarial network (GAN), which is an approach to learning translation mapping with conditional setting to capture structural information. Such that, to synthesize planCT-like from CBCT, unpaired and unaligned CBCT and pCT training datasets were used. They reported that the differences in the maximum and minimum average HUs of muscle and fat ROIs on resulted CBCT images (44 and 83 HU) were much smaller than those of the original CBCT (268 and 218 HU), which indicates that the artifacts were effectively suppressed by the proposed method.

2.3 Discussion

In the Table 2.1, the different works for the correction of CBCT images are grouped following the classification presented previously. The number of patients used in each work and the chosen location are also indicated with some statistical results as reported by the authors of the papers.

Synthesizing these works shows that over the past few years there have been a significant increase in both interest as well as performance of generating from the

Table 2.1: Summary of the different approaches used for the correction of CBCT images.

Approaches	Work	Location	Number of patients	Reported results
Use of physical instruments	[58]	Head and body phantoms	/	Average HU difference in water: ±20 HU Average HU difference in bone and lung: ±130 HU 2D γ pass rate range: 97-99% (5%/2mm)
	[59]	Anthropomorphic chest phantom	/	Average HU difference: $\leq$50 HU Error reduction of 10.3%
	[60]	Anthropomorphic pelvic phantom	/	Streak artifact reduction of 57% CT number linearity: 0.998 CNR=6.42
Scatter modulation	[61]	Water phantom and Anthropomorphic head phantom	/	Water-liver contrast improvement of 3% Water-teflon contrast improvement of 11% Simulation time: 430 h
	[62]	Water cylinder Water cube with 5 bone rods Water sphere with different inserts	/	Simulation time: 39 s
	[63]	Chest phantoms	/	Scatter calculation improvement of 80%
	[54]	Anthropomorphic pelvic phantom H&N Prostate	/ 1 1	Mean Error reduction from 44 to 3 HU for H&N Mean Error reduction from 78 to 9 HU for prostate
	[64]	Anthropomorphic pelvic phantom Anthropomorphic H&N phantom	/	Cupping artefact reduction of 32-88% CNR improvement of 10-50%
	[65]	Lung	5	RMSD reduction of 31%
	[66]	Lung	21	γ pass rate: 99.4% (2%/2mm)
Calibration	[52]	Pelvis Thorax Head	11 11 11	Mean dose difference= 0.9±0.9% Mean dose difference= 1.8±1.6% Mean dose difference= 1.5±2.5%
	[67]	Semi- anthropomorphic pelvic phantom	/	Effect of phantom diameter under bone >20%
	[68]	Prostate	2	Mean dose difference= ±3% γ pass rate: 98% (2%/2.5mm)
	[69]	Thorax	10 (Elekta Linac) 6 (Varian Linac)	Mean dose difference $\leq$10% Mean dose difference $\leq$3%
	[56]	H&N	15	Mean dose difference $\leq$1.1% γ pass rate: 95% (3%/3mm)
HU mapping	[5]	H&N	5	Mean dose difference $\leq$1% γ pass rate: 96% (2%/2mm)
	[51]	Prostate Lung	3 1	Mean dose difference $\leq$2% Mean dose difference $\simeq$5%
HM	[6]	Prostate	10	Mean dose difference $\leq$1%
	[7]	Breast	38	MI=1.0±0.1 Sum of squared differences= 108±38 HU γ pass rate: 99.4% (3%/3mm)

Approaches	Work	Location	Number of patients	Reported results
MLT	[71]	Prostate	3	γ pass rate: 97% (3%/3mm)
	[72]	Prostate H&N Lung	10 10 10	Mean dose difference $\leq$2%
	[6]	Prostate	10	Mean dose difference $\leq$1%
	[73]	Pelvis H&N Lung	4 4 3	Mean dose difference $\leq$1% Mean dose difference $\leq$1% Mean dose difference $\simeq$1.3%
	[57]	Prostate	1	Mean dose difference=$-$1.3% γ pass rate: 97.7% (3%/3mm)
	[74]	Prostate H&N Lung	5 5 5	γ pass rate: 99.6$-$99.9% (2%/0.1mm) γ pass rate: 94.6$-$96.0% (2%/0.1mm) γ pass rate: 94.8$-$96.0% (2%/0.1mm)
DL	[9]	Prostate	20	RMSD(fat)=11 HU RMSD(muscle)=14 HU
	[79]	Prostate	20	Difference in maximum and minimum average HU Muscle=44 HU Fat=83 HU

CBCT images an appropriate base for dose calculation. It has been noticeable that most of research focused primarily on the pelvis and secondly on the H&N, whereas poor work concentrated on the lung or other body parts. For these body regions, promising results have been obtained that demonstrate the feasibility of all proposed approaches for clinical use. However, each approach presents some drawbacks and limitations that should be taken into consideration and could extend the field of research in ART based only on CBCT images. The efficiency of approaches that are based on the use of physical instruments is limited by the fact that the anti-scatter grids or beam blockers attenuate the scatter and the primary photons as well, and the imaging dose therefore needs to be increased to maintain the image quality which may pose a health concern to patients. In addition, improving the performance of beam blockers requires a professionally fabricated grids with optimized parameters, and therefore additional workload requirements appear. The use of these methods decreased with the appearance of approaches based on the scatter modeling and elimination from the CBCT images. Such approaches showed a good agreement between the generated CBCT images and the pCT images; however, as reported by [65] the operator time should be always taken into account because an exact simulation of the imaging system with all its components as well as the scatter measurements for each patient are a time consuming processes, which is not acceptable when aiming to use CBCT images for daily online pre-treatment adaptation.

For the third class which is based on the calibration of CBCT using different

phantoms, although all reported results showed a good agreement between the generated CBCT and the pCT images, the accuracy of these approaches is strongly dependent to the phantom choice and the acquisition parameters. Therefore, the validation of the used phantoms is always needed. Moreover, the improvement of its accuracy requires the establishment of HU-ED tables for each studied region of body, and this can only be performed at the cost of substantial increase in correction time.

In order to avoid all types of integrating hardwares and maintain the workload minimum as possible, another approaches using the pCT images as a prior information for the correction of CBCT images have been appeared. The different modifications included in this class showed high performances in generating corrected CBCT images with decreases HU error even for body regions where the anatomical deformations are significant. However, as these methods relies on DR between the pCT and CBCT images, a stronger validation of registration algorithms is needed to ensure an accurate correction.

Finally, for fast CBCT artefact correction, the use of DL branch in RT has been proposed in the last two years [80, 81, 82]. Excellent results have been obtained when applying these methods on different anatomical sites. However, its implementation needs the availability of a large data and a sophisticated hardware architecture in order to ensure a fast learning process.

For our study, since the IGRT based on CBCT images was newly integrated in clinical practice at the Centre de Lutte Contre le Cancer (CLCC, Setif, Algeria), the number of patients available was limited. Therefore, the DL approaches were not adopted. In addition, as the pCT-based approaches can be easily automated and show high performances in generating CBCT images in good agreement with pCT images, we proposed in this thesis to palliate the limitations of the different approaches included in this class and combine their strengths rather than using time consuming processes as simulation or the integration of hardware for calibration.

2.4 Conclusion

This chapter aimed to present an overview on the generation of corrected CBCT for dose calculation in the context of ART. We presented a classification of the different approaches available in literature and discussed their strengths and weaknesses. According to the comparison of the reported results, one of the main conclusions that one may draw is the remarkable success of the pCT-based approaches for the correction of CBCT images. Despite its dependency to the CBCT image quality and the DR algorithms accuracy, these approaches have shown decreased HU errors even

for body regions where the anatomical modifications are more pronounced. In the light of this conclusion, we propose four contributions for the correction of CBCT images. The first one is an evaluation of different DR algorithms. The second contributions is an assessment of the impact of the chosen algorithms on the CBCT correction by HM. The third contribution is based on a hybrid approach that combines HM with MLT and the last one is a generalization of this later by the use of inter-patient DR process. More details about these contributions are presented in the following chapters.

Chapter 3

The impact of DR accuracy on CBCT enhancement

3.1 Introduction

Recently, the integration of medical image processing field in the ART workflow has offered a chance to generate from the CBCT images an appropriate basis for dose calculation. It is well accepted in literature that the future of using pCT-based approaches for the correction of CBCT images depends on the use of accurate DR algorithms. Thus, the choice of algorithm components with the right parameters is essential for an accurate correction approach.

In this chapter, we present a preliminary work consisting of the evaluation of different DR algorithms in terms of their accuracy and computation time. Then, we present the proposed correction approach and based on the results of the performed tests, we assess the impact of the chosen algorithms on its performance.

3.2 Data description

In this thesis, all studies was performed on data sets of 10 patients with prostate cancer containing pCT and CBCT images obtained by Simense scanner and on-board imager (OBI, Varian Medical Systems) mounted on the gantry of clinical iX21 linear accelerator, respectively. The settings of pCT and CBCT acquisition according to pre-defined protocols are recapitulated in Table 3.1. The slices number differed from a patient to another; it ranged from 123 to 159 slices in the pCT images and from 50 to 64 slices in the CBCT images giving sufficient information about the anatomical distribution and the motion artifact variations. For all these data CBCT images were acquired for the first day of treatment to minimize the error of patients setup under the

treatment machine. Since this technique is newly integrated in the clinical practice, the number of patients used in this study is limited.

Table 3.1: Acquisition settings of pCT and CBCT images.

Protocol	Tube current (mA)	Exposure time (ms)	Tube voltage (kVp)	Axial image size (pixels)	Voxel size (mm^3)
CBCT	360	500	100	512x512	0.8496x0.8496x3.0
pCT	80	8632	125	512x512	0.8789x0.8789x2.5

3.3 Evaluation of CT to CBCT deformable registration algorithms

Since the choice of algorithm components is highly dependent to the imaging modality and the anatomical region to be registered, a preliminary work aiming to evaluate the accuracy of CT to CBCT deformable registration is presented in this section. Six algorithms with different similarity measures and optimizers were tested in terms of their accuracy and computation time on a small set of data in order to find a set of promising parameters to use in further studies.

3.3.1 Data preprocessing

Initially, collected CBCT and pCT contained not only the information describing the patients body but also the couches of the CT scanner and the linear accelerator. For that reason, all images were pre-processed using the FIJI software [83] to select the region including the patient volume and remove the couches. Furthermore, to eliminate all unnecessary content, a fixed threshold was applied to assign all pixels outside the body surface (below 700 HU for pCT and bellow -600 HU for CBCT) to standard CT value for air (-1000 HU) using the 3D Slicer software [84]. Results of registration for the images with and without couches were compared.

3.3.2 Image registration

Before starting the DR, the pCT images (referred to as the moving images) for each patient were rigidly registered to the CBCT images (fixed images), using the 3D rigid transformation described in chapter 1, in order to ensure a good alignment between images and improve the speed of DR. Then, a DR process was applied on the obtained

pCT images to minimize the effect of difference in organs deformation between the pCT and the CBCT images. A multi-resolution B-spline transformation with different similarity measures, namely NCC, MI and NMI, and two optimizers (GD and ASGD) were used.

The six algorithms resulting from the combination of the previously mentioned elements were implemented in Elastix [38] which is an open source software based on the insight segmentation and registration toolkit (ITK) that gives the possibility to choose several registration components to create the algorithms that suits to our needs. The different components and parameters used for this study are recapitulated in Table 3.2.

Table 3.2: Summary of study algorithms with their different components and parameters.

Algorithm number	**Components**								
	Transform	**Metric**	**Optimizer**		**Interpolator**		**Sampler**		**Pyramids**
	Name	**Name**	**Name**	**Parameter**	**Name**	**Parameter**	**Name**	**Parameter**	**Name**
1	Deformable Registration (BSpline Transform)	AdvancedMattes MutualInformation	Standard Gradient Descent	A = 50 a = 2000 α = 0.602	BSpline Interpolator	Number of iterations = 300	Random Coordinate	Number of Samples= 3000	Fixed Smoothing Image Pyramid & Moving Smoothing Image Pyramid
2		AdvancedNormalized Correlation				Number of iterations = 500			
3		NormalizedMutual Information							
4		AdvancedMattes MutualInformation	Adaptive Stochastic Gradient Descent	Automatic determination of A, a and α		Number of iterations = 300			
5		AdvancedNormal ized Correlation				Number of iterations = 500			
6		NormalizedMutual Information							

α and a : constants defined by the user, A: 10% of the maximum number of iterations.

3.3.3 Evaluation

The accuracy of registration was evaluated by two different methods. The first one consisted of using VV image viewer [85] to perform a visual assessment. This software allows comparing the deformed moving images (planning CT in our study) to the fixed images (CBCT) by superimposing them using complementary colors. The second method consisted of a quantitative evaluation; it was mainly based on the measures of similarity between the deformed moving images and the fixed images using Elastix. For this comparison we used as metrics, the MSD and the NCC described in chapter 1.

3.3.4 Computation time

The consumed time to perform the registration is an important criterion to accept or refuse the algorithm for clinical practice, therefore, the computation time for each algorithm were measured. For this study, all the calculations were done on $Intel^{®}$ $Core^{TM}$ i5-3230M CPU (2.60 GHz, 4 GB RAM).

3.3.5 Results and discussion

3.3.5.1 Qualitative evaluation

Figure 3.1.a and b show respectively the CBCT and pCT slices used for this study. Generally, the number of slices acquired for these two types of tomography is not the same. Therefore, the superimposition of all slices can lead to a miss-alignment between the CBCT and pCT images as shown in Figure 3.1.c. To deal with this problem a RR was applied resulting in a good global alignment (Figure 3.1.d), whereas in specific regions as the bony regions a poor registration can be observed.

Figure 3.2 presents the results of superimposition of the CBCT images (fixed images) and the deformed CT images by applying different DR algorithms. As shown in Figure 3.2.a, b and c, the use of the GD with MI, NCC and NMI results in good alignment between anatomical structures but with some differences in body contours due to the fact that the algorithms based on GD depends on the increased amount of scatter present in CBCT images. On the other hand, the Figure 3.2.d, e and f, in which a combination of ASGD with MI, NCC and NMI were used, show an excellent alignment between anatomical structures and also body contours which demonstrates the independency of those algorithms on the quality of CBCT images.

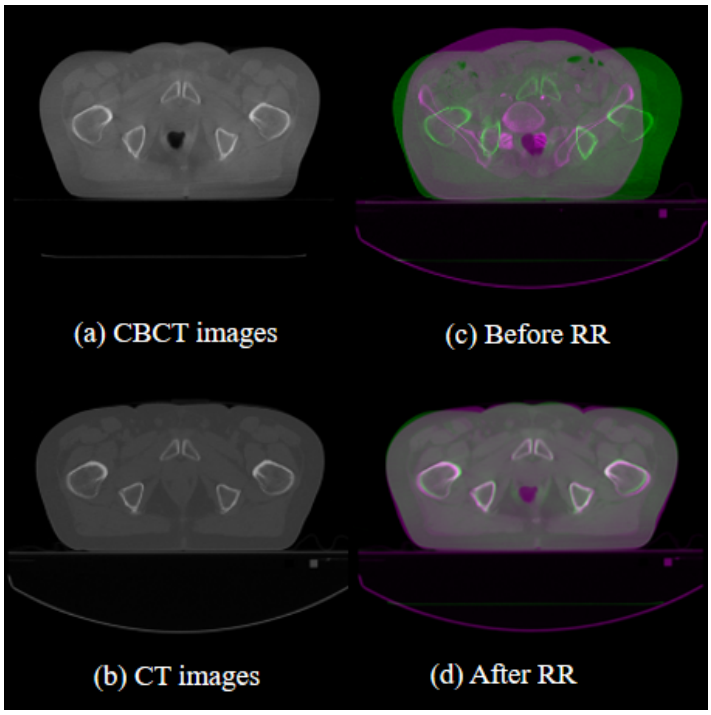

Figure 3.1: A slice of CBCT images (a), planning CT images (b) and the results of their superimposition before alignment (c) and after alignment (d) with rigid registration.

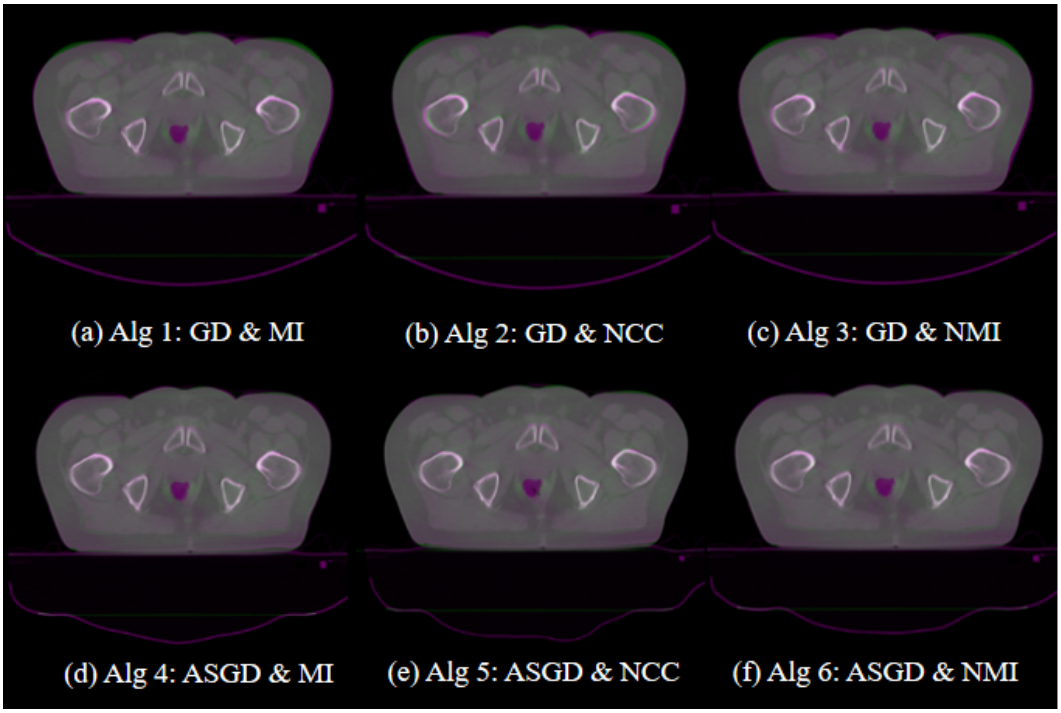

Figure 3.2: Results of superimposition of CBCT and deformed pCT images after using six DR algorithms based on (a) GD and MI (b) GD and NCC (c) GD and NMI (d) ASGD and MI (e) ASGD and NCC (f) ASGD and NMI.

3.3.5.2 Quantitative evaluation

Figure 3.3 illustrates the results of comparison of CBCT and deformed CT images with and without couches using the MSD for which the lower the metric value, the better the registration. For the two patients, we observe acceptable values of MSD ranging from 0.115 to 0.128 mm for the algorithms based on GD, while we achieve a better registration accuracy for the algorithms based on ASGD optimizer with lower MSD values ranging from 0.055 to 0.067 mm. Furthermore, the pre-processing of CBCT and pCT images by removing the couches before applying the DR decreased the MSD values from about 0.12 mm to lower values of about 0.06 mm. Besides, regarding the combination of GD or ASGD with MI, NCC or NMI, the results show that in the most of cases the use of ASGD with NCC can improve the quality of registration giving decreased values of MSD compared to the other algorithms.

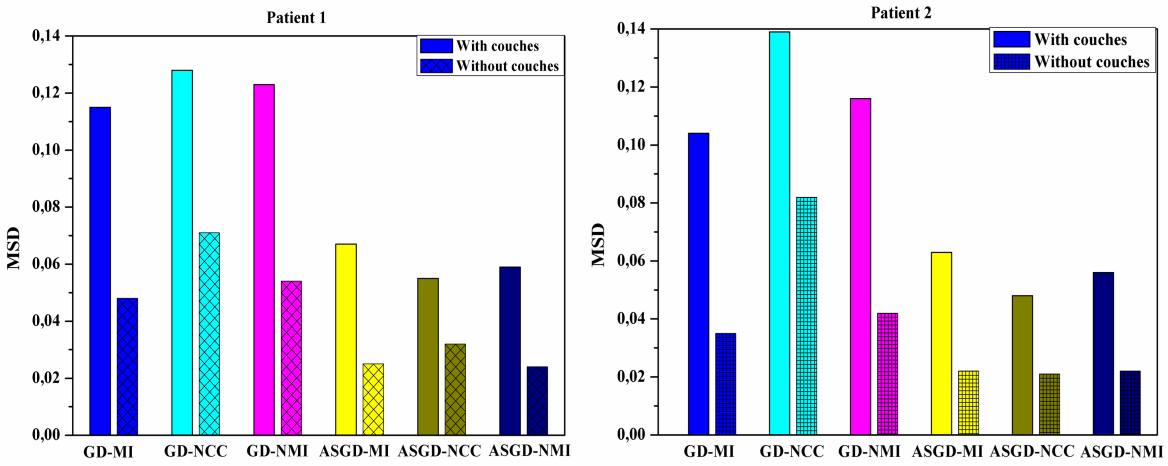

Figure 3.3: Comparison of MSD values between CBCT and deformed pCT images with and without couches for two patients using the different algorithms.

In the same way, Figure 3.4 presents the results of comparison of CBCT and deformed pCT images with and without couches using the NCC for which the optimum is reached for metric value of -1. The measured values of NCC are presented in absolute values as visible in Figure 3.4. For the two patients, the results show a good correlation between CBCT and deformed pCT with NCC values close to 1. In addition, the DR based on images without couches yielded more accurate results of about 0.99 which confirm the advantages of the pre-processing of pCT and CBCT images. In addition, the performances of ASGD with NCC was confirmed. Thus, we can say that applying this algorithm on pre-processed pCT and CBCT images allows gaining in terms of accuracy.

Results of measuring the required time to complete the registration process are summarized in Table 3.3. When comparing the obtained results for each algorithm a

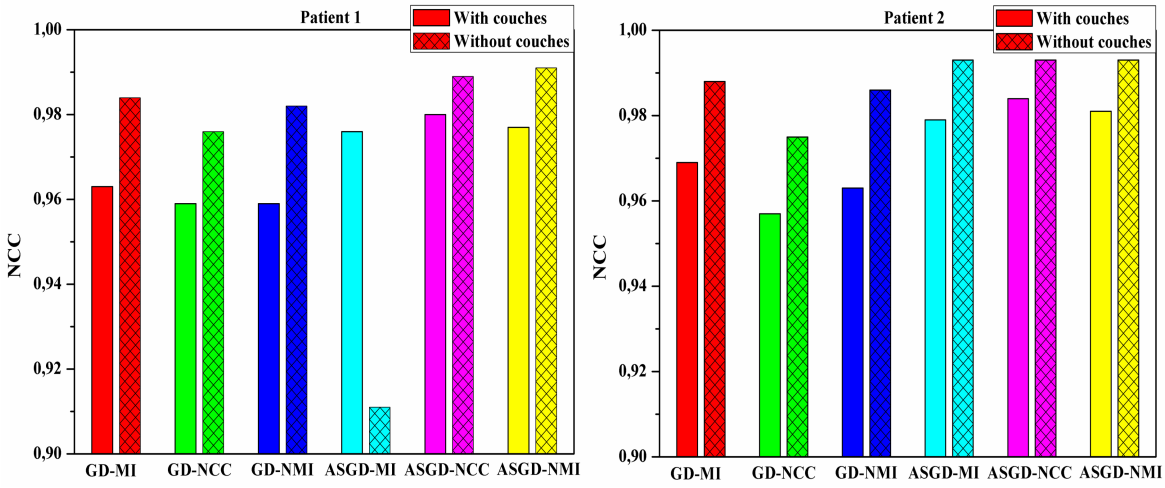

Figure 3.4: Comparison of the NCC values between CBCT and deformed CT images with and without couches for the two patients using the different algorithms.

large variability can be observed. We found that the DR with ASGD was two times longer than using the GD optimizer. Also, the use of both GD and ASGD with NMI and NCC was in the most of cases a time consuming process while the combination of GD with MI ran in a shorter time. Moreover, the computation time was markedly reduced when using pre-processed images.

In this thesis, since the used algorithms were not studied under sophisticated hardware allowing the optimization of the execution time we will focus more on the DR accuracy and keep the optimization task for further studies. Therefore, referring to all the obtained results, the use of ASGD-NCC with modified pCT and CBCT images seems to be the most appropriate to gain in terms of accuracy.

Table 3.3: Comparison of the computation time of the different algorithms using images with and without couches.

Algorithm	**Patient 1**		**Patient 2**	
	With couches	**without couches**	**with couches**	**without couches**
GD-MI	16 min 3.5 s	10 min 7.5 s	9 min 59.2 s	10 min 39.6 s
GD-NCC	16 min 11 s	11 min 43.7 s	10 min 6.3 s	10 min 15.2 s
GD-NMI	32 min 55.8 s	18 min 49.9 s	19 min 21.5 s	19 min 8 s
ASGD-MI	29 min 50.6 s	17 min 45.9 s	31 min 57.4 s	19 min 59.7 s
ASGD-NCC	29 min 58.8 s	16 min 8.6 s	28 min 46.3 s	18 min 10.3 s
ASGD-NMI	50 min 42.1 s	33 min 31.1 s	44 min 18.2 s	27 min 16.1 s

3.4 Impact of DR on CBCT enhancement

Among the previously tested algorithms those based on ASGD optimizers showed better alignment of anatomical structures in the pCT and CBCT images. However, to confirm the dependency between the DR algorithm and the correction accuracy and validate the choice of the appropriate similarity measure, a comparative study showing the impact of each similarity measure is required. Therefore, we present in this section the results of applying our proposed approach with different DR algorithms.

3.4.1 Corrected CBCT generation

In order to assess the impact of DR on the quality of CBCT enhancement, three intensity-based algorithms with different similarity metrics were used. The workflow of corrected CBCT generation is described in Figure 3.5.

After DR, the 3D slicer software was used to match the histograms of the CBCT images against the corresponding deformed pCT (step3 in Figure 3.5). As described in the previous chapter, this processing method aims to adjust the HU values between pCT and CBCT images using their cumulative histograms. Each pixel value in the CBCT images is replaced by the HU having the same cumulative value in the pCT images.

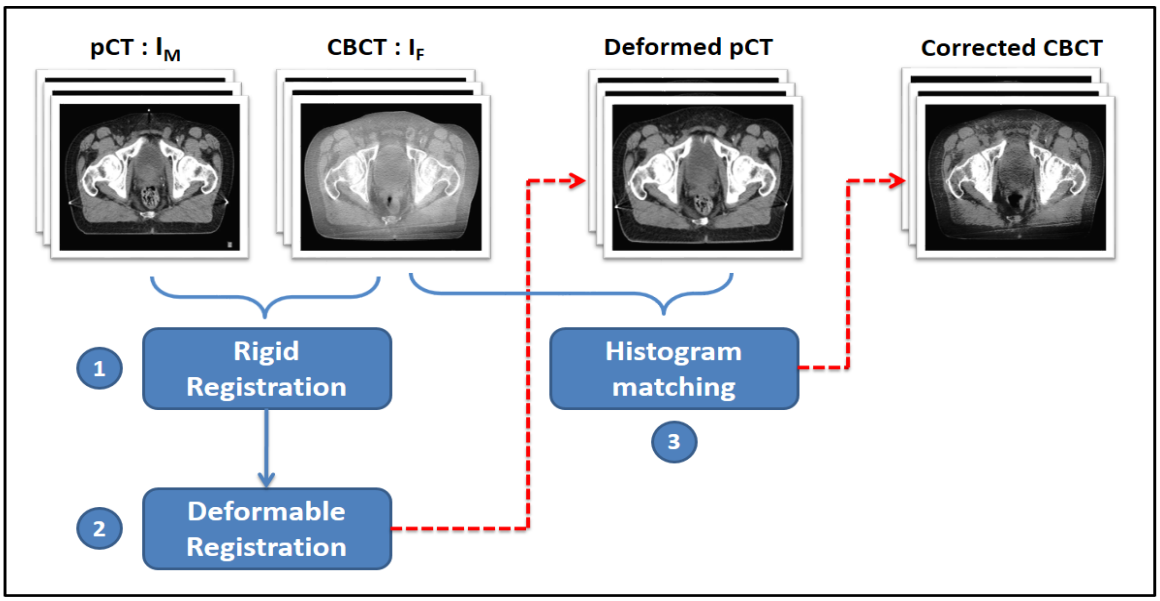

Figure 3.5: Workflow of corrected CBCT generation.

3.4.2 Data analysis

To evaluate the quality of corrected CBCT, deformed pCT images were considered as a reference for each patient. A visual assessment was performed by the calculation of absolute difference between pCT and CBCT images before and after HM to assess the discrepancies between them.

Furthermore, to evaluate quantitatively the agreement between corrected CBCT and pCT, three methods were used. The first one consists of the average HU error estimation over the entire volume, called also the root mean squared difference (RMSD), [65] given by:

$$RMSD = \sqrt{mean([HU_{pCT}(x,y,z) - HU_{CBCT}(x,y,z)]^2)} \tag{3.1}$$

The second method is the mean absolute error (MAE) plots creation which allows comparing the different tissue classes. It is based on the calculation of the MAE between pCT and corrected CBCT in equidistant bins across the HU scale. For this comparison a size of 20 HU was taken for each bin and the formula describing the MAE is given by:

$$MAE = \frac{1}{N}\sum_{i=0}^{N} |HU_{pCT_i} - HU_{CBCT_i}| \tag{3.2}$$

Where N is the number of pixels having intensities in [HU-10, HU+10] in the pCT images [86].

The third one is the image quality evaluation in terms of spatial uniformity. For this method, the mean pixel value among five regions of interest (ROIs) having 10 by 10 pixels and positioned in regions of the same soft tissue area was measured [9]. Then, the RMSD between the mean pixel values in the pCT and the CBCT images before and after correction were calculated.

3.4.3 Results

3.4.3.1 Visual assessment

Figure 3.6 shows the absolute difference between deformed pCT and CBCT images for one patient before and after HM using three DR algorithms (DR-NCC, DR-MI and DR-NMI). Obtained results for a RR algorithm are also included to confirm the effect of morphologic deformation between pCT and CBCT on the correction quality. The effect of applying HM is clearly visualized; it reduced the amount of artefacts in CBCT and yielded corrected images in good agreement with deformed pCT. However, high differences in bony regions and soft tissue-air interfaces are present due to the

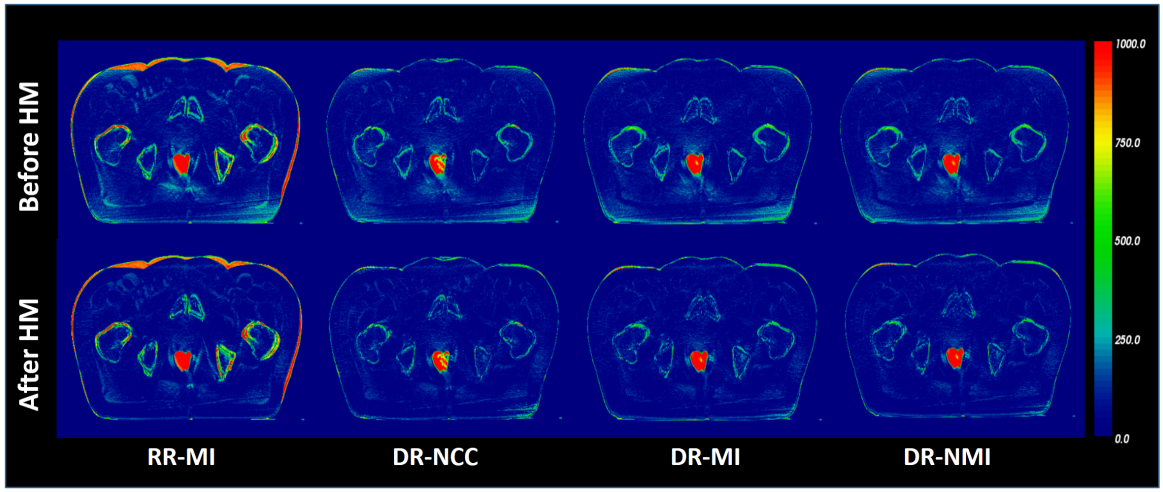

Figure 3.6: Absolute difference between deformed pCT and CBCT in the first row and corrected CBCT in the second row using one RR and three DR algorithms. Blue colors represent low discrepancies while red colors represent the highest ones.

misalignment between CBCT and pCT.

3.4.3.2 Volumes comparison

Results of volumes comparison for each patient in terms of HU average error between deformed pCT and CBCT before and after correction are shown in Table 3.4. The mean and the standard deviation are also presented. The largest magnitude of RMSD is observed for processed CBCT images when using RR process where the mean HU error value was about 221.68 ± 57.97 HU. For the DR process, a significant decrease was obtained with error values ranging from 64.15 ± 9.50 to 68.20 ± 10.12HU which confirms the performance of DR algorithms. Whereas, after the correction of CBCT images reduced values of HU of about 55.95 ± 10.43 HU, 56.58 ± 10.51 HU and 58.60 ± 10.35 HU were obtained for DR-NCC, DR-NMI and DR-MI, respectively, indicating that the HM after using DR-NCC yielded corrected CBCT images in good agreement with pCT images compared to unprocessed CBCT images.

3.4.3.3 Tissue class's comparison

Since volumes comparison may not give information about the presence of large errors and their location, the MAE plots for each algorithm over the HU scale are illustrated in Figure 3.7. Similarly to [6], HU scale for pCT images was divided according to the tissue type on different classes. All the values lower than -400 HU was considered as air. The HU values between -400 and 250 HU were associated to soft tissues, while those between 250 and 600 HU presented the soft bone. The remaining values (higher

Table 3.4: HU average error values between deformed pCT and CBCT before and after HM for each patient with the mean and the standard deviation.

RMSD (HU)								
Patient's number	RR-MI		DR-NCC		DR-MI		DR-NMI	
	Before HM	After HM	Before HM	After HM	Before HM	After HM	Before HM	After HM
1	138.50	141.33	71.03	64.70	75.94	68.07	73.53	65.67
2	140.00	143.01	57.89	49.10	60.77	51.76	59.90	49.87
3	260.62	288.10	73.58	65.17	76.33	66.71	75.09	64.84
4	257.67	274.16	65.76	55.10	71.23	57.05	68.51	54.03
5	239.04	267.54	67.48	55.73	73.34	59.89	71.44	58.02
6	258.85	269.82	82.09	77.88	87.37	80.24	86.24	79.04
7	171.96	195.80	57.74	47.26	60.12	48.18	58.90	46.26
8	193.20	194.09	54.89	45.74	58.68	47.75	57.23	46.03
9	153.75	173.61	51.82	45.90	56.13	51.47	54.33	49.09
10	251.15	269.41	59.29	52.92	62.16	54.96	60.62	53.01
Mean	206.47	**221.68**	64.15	**55.95**	68.20	**58.60**	66.57	**56.58**
SD	52.21	**57.97**	9.50	**10.43**	10.12	**10.35**	10.06	**10.51**

than 600 HU) were considered as bone.

Figure 3.7.a compares MAE results using RR algorithm before HM with those obtained after HM. It shows obviously that the use of HM with RR increases the uncertainties in CBCT images, due to the misalignment between pCT and CBCT images. However, in (Figure 3.7.b, c and d) the MAE becomes lower and the combination of DR with HM contributes significantly to reduce the errors after correction, especially for pixels with CT number higher than 200 HU. For the values below 200 HU a mismatch is observed and the MAE values after correction are higher than before. This is due to the low number of pixels in corrected CBCT containing the same HU values as pCT in the interfaces soft tissue-air, which is in agreement with the visual assessment where high errors were noticeable in those regions owing to the improper registration.

The DR performance comparison is depicted in Figure 3.8. Plotting together the MAE values before and after correction against each other (Figure 3.8.a and b respectively) shows that the use of DR based on NCC metric was better than MI

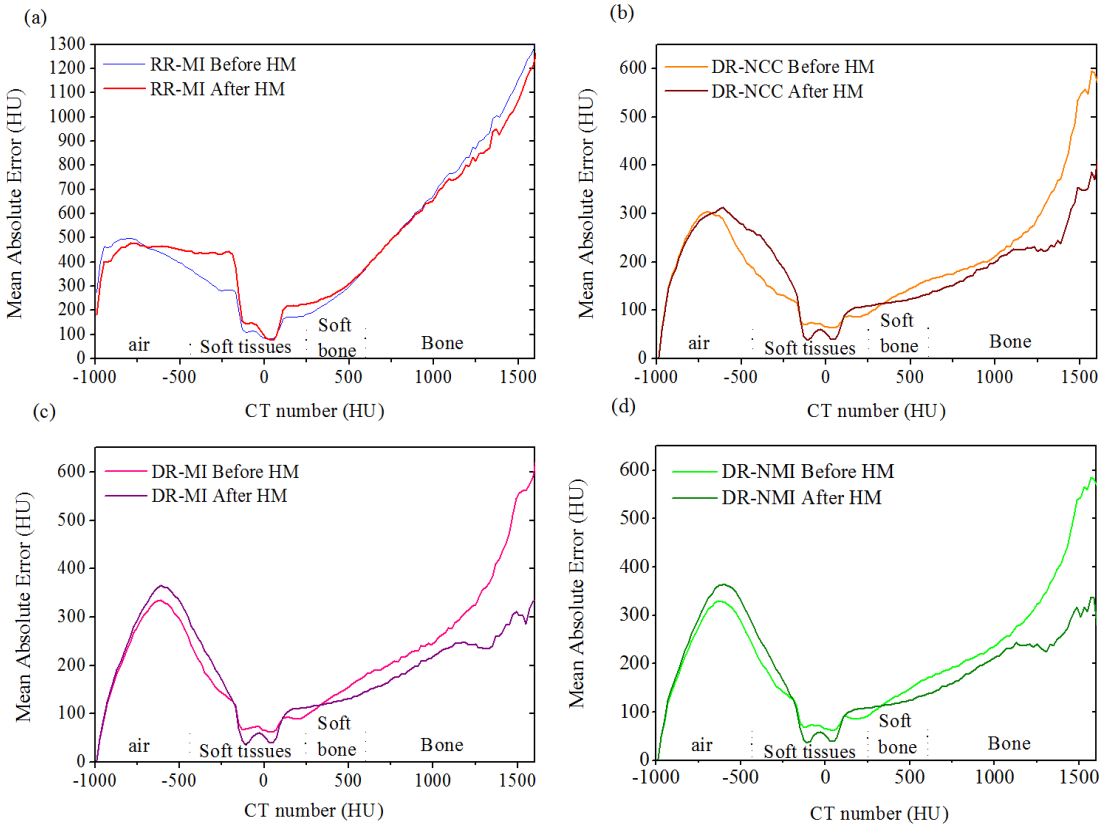

Figure 3.7: MAE values of CBCT images before and after correction using a) RR-MI, b) DR-NCC, c) DR-MI and d) DR-NMI.

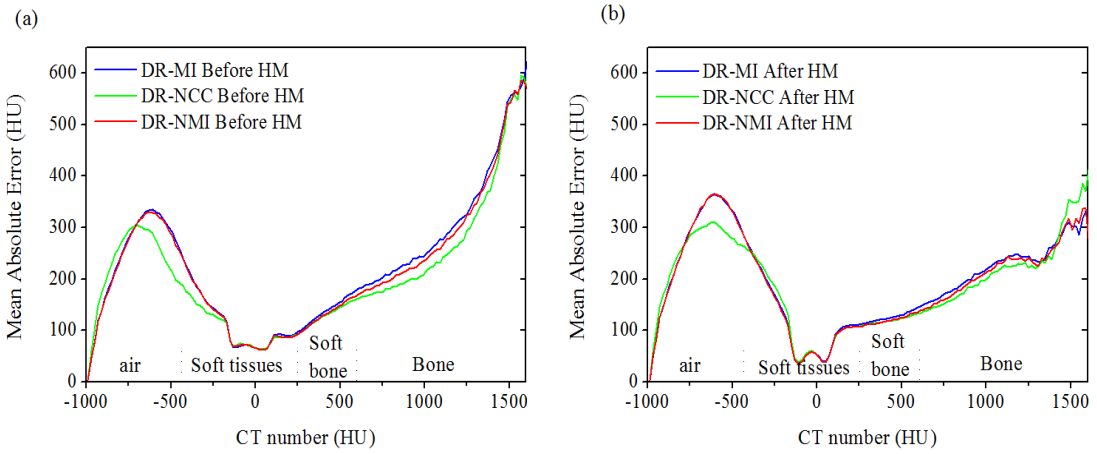

Figure 3.8: MAE values of CBCT images for each algorithm before HM (a) and after HM (b).

and NMI especially in soft tissue-air interfaces. Moreover, using the NCC metric in combination with HM produced more accurate CBCT images.

Concerning the uniformity of resulted CBCT images, the RMSD of the mean pixel

values of ROIs between CBCT, corrected CBCT and pCT images are summarized in Table 3.5. The obtained results showed that the use of HM reduced the RMSD in fat and muscle (soft tissues) from about 57 and 25 HU to 8 HU, respectively, indicating that the CBCT image quality was brought closer to the pCT image quality through this correction technique.

Table 3.5: Comparison of the mean pixel values in fat and muscle between the pCT, CBCT and corrected CBCT images with the three different DR algorithms.

Mean pixel value (HU)					
Patient's	**Fat**				
number	**pCT**	**CBCT**	**CBCT$_{\text{DR-NCC}}$**	**CBCT$_{\text{DR-MI}}$**	**CBCT$_{\text{DR-NMI}}$**
1	-108.16	-144.37	-90.73	-92.50	-92.06
2	-87.68	-163.92	-84.98	-88.25	-85.77
3	-104.83	-139.75	-90.03	-91.48	-91.16
4	-103.80	-151.60	-104.64	-105.23	-105.19
5	-103.43	-170.34	-102.28	-103.16	-102.89
6	-109.43	-130.55	-98.50	-99.30	-99.09
7	-97.70	-148.56	-97.08	-98.47	-97.97
8	-108.62	-213.92	-108.76	-108.53	-108.04
9	-110.23	-160.35	-105.87	-106.76	-106.82
10	-99.50	-123.33	-100.24	-101.55	-101.40
RMSD		**56.83**	**8.19**	**7.38**	**7.57**
	Muscle				
1	49.45	-1.37	31.76	30.62	30.68
2	51.61	25.39	42.09	41.12	41.68
3	47.59	59.00	53.25	54.53	53.25
4	42.17	45.81	50.65	51.61	50.93
5	48.87	11.70	47.66	47.66	47.65
6	49.68	40.03	50.09	50.78	50.25
7	49.73	28.39	45.44	46.12	46.01
8	46.46	13.39	36.65	39.04	39.34
9	48.85	56.30	52.18	51.95	51.86
10	49.44	51.98	45.97	47.25	46.40
RMSD		**25.49**	**7.72**	**8.28**	**8.02**

3.4.4 Discussion

In this work, the impact of choosing different registration algorithms on the quality of CBCT correction by HM was studied. One RR algorithm based on MI similarity metric and three DR algorithms including NCC, MI and NMI similarity metrics were validated.

Several studies investigated the accuracy of dose calculation based on corrected CBCT using HM with DR based on MI [6, 7] but our strategy differs from those studies because it aims to initially choose the appropriate DR algorithm, and then generate corrected CBCT images.

All the results confirmed that the performance of DR of each algorithm is strongly dependent on the region in which the transformation was applied. It was shown that all DR algorithms provided a good alignment between anatomical structures in pCT and CBCT compared to RR registration but their reduced ability to align some regions as soft tissue-air and soft tissue-bone interfaces was clearly visualised. In addition, the sensitivity of HM process to the quality of registration has been proved. It has been found that the better the alignment the more significant is the HM contribution to correct the HU distribution in CBCT images. For that reason, the best compromise for this correction method seems to be the use of DR with NCC similarity metric for which the MAE values after correction were found to be the lowest as indicated in Figure 3.8. Also, this choice can be justified by Table 3.4 where reduced HU errors in corrected CBCT were obtained for the DR-NCC algorithm.

Despite the influence of DR accuracy on the HM process, the use of DR-NCC before HM yielded acceptable HU errors values compared to other studies investigating pCT-based approaches and direct approaches without recourse to pCT [9, 87]. In [9], Kida et al. applied a deep convolutional neural network (DCNN) method to improve the quality of CBCT images acquired for 20 prostate cancer patients. They reported that the RMSD of the mean pixel values for corrected CBCT images was about 11 and 14 HU in fat and muscle, respectively, while in our study the same evaluation showed that the RMSD was about 8 HU. This suggests that our proposed workflow had successfully improved the spatial uniformity in the CBCT images. Besides, Poludniowski et al. [87] studied for 12 patients (6 brain, 3 prostate and 3 bladder cancer patients) four correction methods based on scatter calibration and scatter measurement using CBCT images acquired by other linear accelerator (Elekta Linac). They reported that for prostate cancer the average HU error for each method, called also Root Mean Squared Difference, were about 95.5, 91.5, 73.1 and 67.7 HU. Whereas, in our study the HM considered as pCT-based approach resulted in average HU error of about 55.95 ± 10.43 HU when using DR-NCC indicating that although our CBCT images

differs from theirs; our results are better than their findings.

To improve the correctness of the proposed workflow, the minimization of its limitations as the existence of non-comparable regions in the pCT and CBCT images, e.g. regions of gas in the rectum, is a priority. Thus, further investigations taking into account the correction of these regions before performing DR and HM are required. In addition, dosimetric evaluation is needed to validate the efficiency of using corrected CBCT for dose calculation in the context of adaptive radiation therapy. Also, we are looking forward to applying this workflow on large number of patients and translate it to other body regions.

3.5 Conclusion

In this chapter, we presented the results of evaluating different CT to CBCT DR algorithms. Then, we studied their impact on the correction of CBCT images using HM. It has been found that the quality of correction is strongly dependent on the accuracy of DR process and revealed that performing HM after DR with the NCC similarity metric contributed significantly to reduce the uncertainties in CBCT images. Although the proposed workflow showed acceptable performance, seeking for more accurate results is still a research topic. Therefore, we present in the next chapter our second contribution for the enhancement of CBCT images which consists of the optimization of the proposed workflow by hybridizing it with another pCT-based approach.

Chapter 4

Optimization of the proposed method by the development of a hybrid approach

4.1 Introduction

Recent studies have proved the usefulness of pCT-based approaches for the correction of HU distribution in CBCT images. Among the proposed approaches there were those based on multilevel threshold (MLT). Since these strategies are mainly based on the segmentation of different tissue types in the target images and the higher the image contrast, the more accurate the correction is, the application of such strategies on CBCT images warrants the need to improve their contrast.

Inspired from the previous chapter findings, wherein the application of HM on CBCT images offered the possibility to distinguish the different tissue types in the CBCT images, we present in this chapter an extension to our previous works [88, 89] where we propose a new hybrid approach that applies first the HM, then, the MLT processes.

4.2 Methods

4.2.1 Data description

The data used in this chapter is the same data used throughout this thesis. It was described in chapter 3.

4.2.2 Description of the proposed approach

In order to correct the HU distribution and generate an appropriate base for dose calculation, two different pCT-based approaches were consecutively applied as shown in Figure 4.1. The first approach was the HM, evaluated in [89], which allowed changing the gray-level histogram of the CBCT images to resemble the pCT image histogram offering the possibility to distinguish the different tissue types present in the CBCT images.
The previously proposed workflow [89] can be summarized in the following steps (Figure 4.1, phase1):

- Images preprocessing by eliminating all unnecessary content in the pCT and CBCT images using a thresholding method to assign to the voxels outside the patients body the standard value for air (-1000 HU).
- Application of a DR process to ensure an accurate alignment between anatomical structures in the pCT and CBCT images. For this study a B-spline transform with the NCC metric implemented in Elastix was used.
- Modification of the HU values in the CBCT images by matching their histograms to those of deformed pCT ($CBCT_{HM}$). The HU values in the CBCT images were replaced by the HU values in the deformed pCT images having the same cumulative value.

Subsequently, MLT was applied to improve the correctness of the HU distribution obtained with HM (Figure 4.1, phase 2). The voxel values in the $CBCT_{HM}$ images were grouped into five segments representing air, fat, muscle, soft bone and bone according to the HU ranges extracted from their histograms. Then, the HU values corresponding to the peak of each tissue in the pCT images were assigned to each segment. The HU range and the peak value for each tissue type are listed in Table 4.1.

Finally, the resulting CBCT images ($CBCT_{HM\text{-}MLT}$) were smoothed using a mean box filter with voxel size of 1x1x1 mm^3 to decrease high intensity variations that may occur inside the segments.

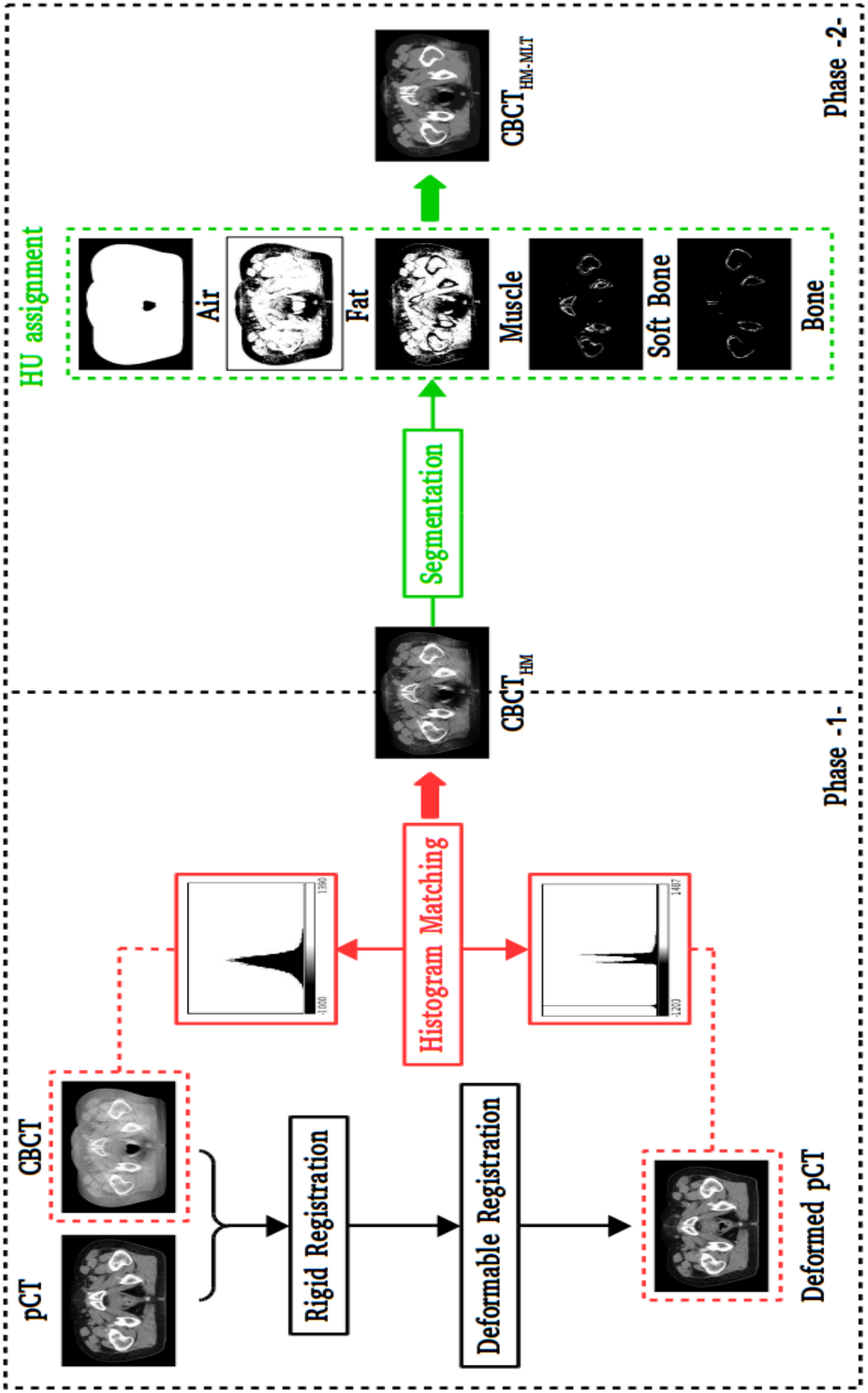

Figure 4.1: Pipeline of the CBCT enhancement process.

Table 4.1: HU range and peak value of different tissue types present in pCT and CBCT images after HM. The ranges of soft bone and bone were divided into two sub-ranges, each replaced by a peak value, to take into account low and high HU values that represent each tissue.

Tissu type	**HU range (HU)**	**Peak value (HU)**
Air	Below -400	-1000
Fat	From -400 to -30	-114
Muscle	From -30 to 250	46
Soft bone	From 250 to 500 From 500 to 600	450 600
Bone	From 600 to 900 above 900	800 1400

4.2.3 Evaluation

To assess the accuracy of the proposed approach the absolute difference between the pCT and the CBCT images before and after correction was calculated and visualized using the VV image viewer [85]. The HU values along four line profiles with different directions extracted from the pCT and the $\text{CBCT}_{\text{HM-MLT}}$ images were also compared. Figure 4.2 shows the positions where the comparisons were performed. The correlation coefficient (CC) between deformed pCT and CBCT images before and after HM+MLT was calculated and compared according to:

$$CC = \frac{\sum_m \sum_n (HU_{pCT_{mn}} - \overline{HU_{pCT}})(HU_{CBCT_{mn}} - \overline{HU_{CBCT}})}{\sqrt{[\sum_m \sum_n (HU_{pCT_{mn}} - \overline{HU_{pCT}})^2][\sum_m \sum_n (HU_{CBCT_{mn}} - \overline{HU_{CBCT}})^2]}} \quad (4.1)$$

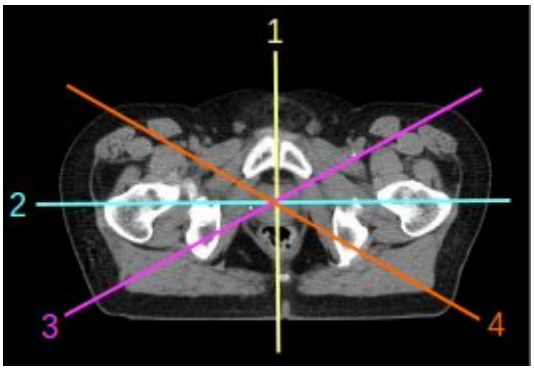

Figure 4.2: A pCT slice with four lines describing the directions of the extracted profiles.

Where $\overline{HU_{pCT}}$ and $\overline{HU_{CBCT}}$ are the mean HU values of the deformed pCT and CBCT images, respectively, and N is the total number of voxels.

Furthermore, the agreement between the pCT and the $\text{CBCT}_{\text{HM-MLT}}$ images was estimated by calculating the RMSD over the entire volume and finally, to localize errors over the HU scale, we computed the MAE histogram between the pCT and the $\text{CBCT}_{\text{HM-MLT}}$ images for different tissue classes.

4.3 Results

4.3.1 Visual assessment

Figure 4.3 shows the absolute difference between the HU values of the deformed pCT and CBCT images before correction (Figure 4.3.a), after correction using only HM (Figure 4.3.b) and after using HM followed by MLT (Figure 4.3.c). From these images, it is noticeable that the high discrepancies observed for uncorrected CBCT images were significantly reduced when applying our proposed approach compared to using only HM. However, some high differences in the soft tissue-air and soft tissue-bone interfaces can be observed. In addition, the observed high discrepancies in the center where the rectum is located are caused by differences in rectum fillings during the acquisition of CT and CBCT images.

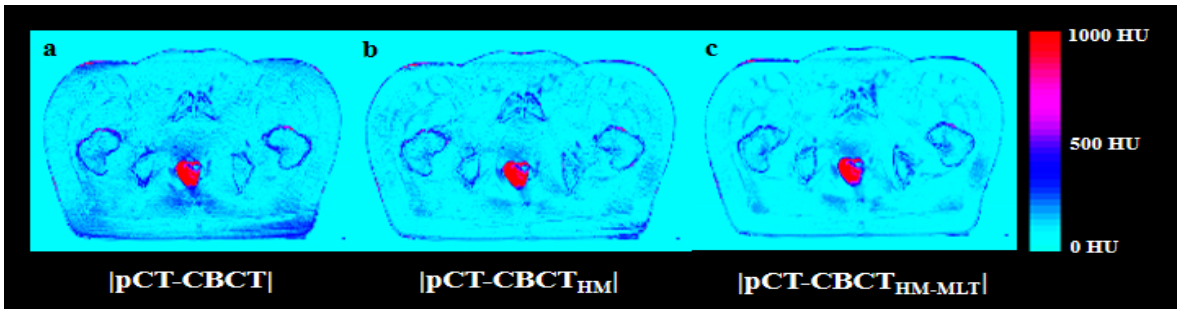

Figure 4.3: Absolute difference between the HU values of the deformed pCT and CBCT images (a) before correction, (b) after using only HM and (c) after using HM+MLT correction.

4.3.2 Profiles comparison

The profile extracted in correspondence of the four lines drawn in Figure 4.2 are illustrated in Figure 4.4. It shows that before correction (Figure 4.4.a-d) the profiles of the CBCT images are more irregular compared to those of the $\text{CBCT}_{\text{HM-MLT}}$ (Figure 4.4.e-h). There are also high differences between the HU values of the pCT

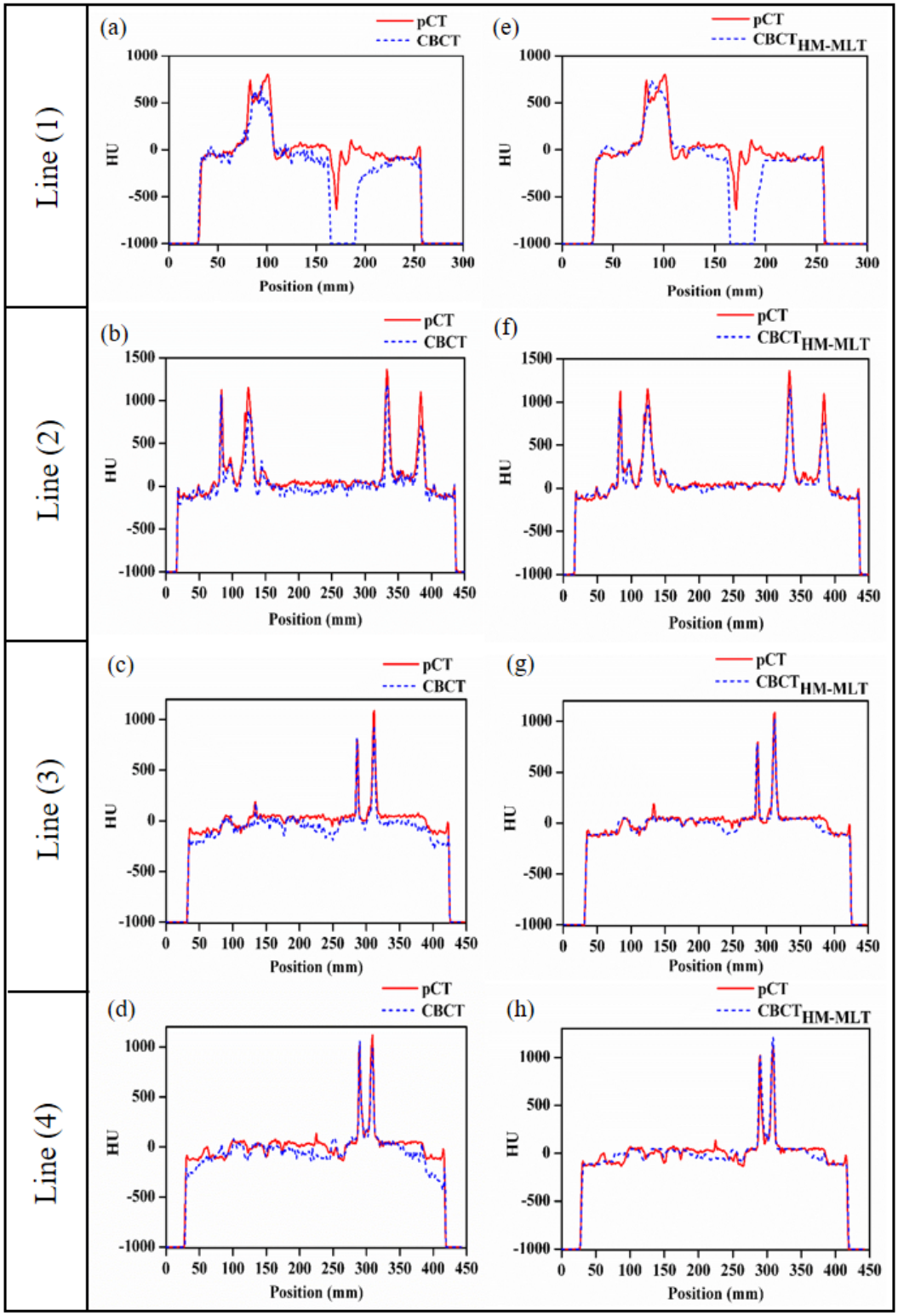

Figure 4.4: HU comparison between deformed pCT and CBCT images (a-d) before any correction and (e-h) after HM+MLT correction along the four lines describing the directions of the extracted profiles shown in Figure 4.2.

and CBCT images especially near the soft tissue-air interfaces. After applying the HM+MLT correction, the HU values in the $CBCT_{HM\text{-}MLT}$ achieved approximately the same values as in the pCT images indicating that the use of this combination contributed significantly to improve the quality of CBCT images.

4.3.3 Correlation

To further evaluate the accuracy of the proposed approach, Figure 4.5 compares the correlation between the deformed pCT, CBCT, $CBCT_{HM}$ and $CBCT_{HM\text{-}MLT}$ images. For all patients, the obtained results show that corrected CBCT images are in good agreement with the deformed pCT with correlation values ranging from 0.9893 to 0.9962 compared to the $CBCT_{HM}$ and CBCT images for which the correlation values range from 0.9878 to 0.9955 and from 0.9871 to 0.9945, respectively.

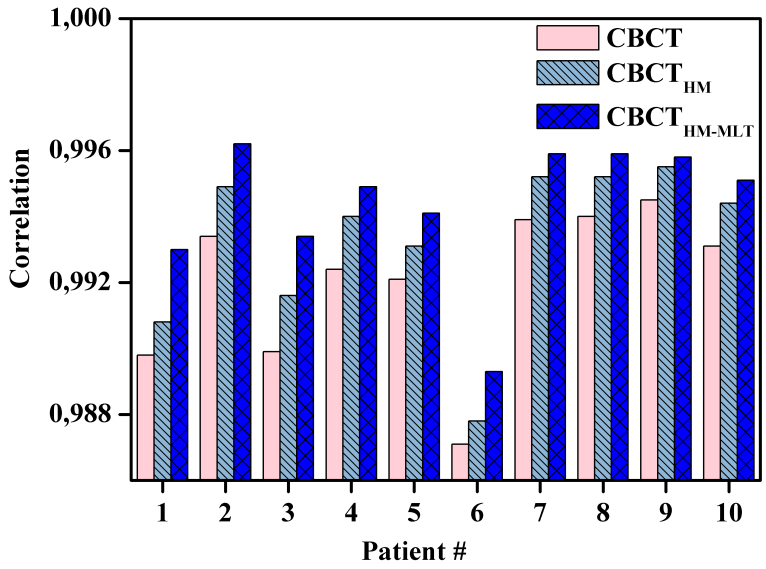

Figure 4.5: Correlation values between deformed pCT, uncorrected CBCT, $CBCT_{HM}$ and $CBCT_{HM\text{-}MLT}$ for each patient.

4.3.4 Volumes Comparison

Table 4.2 shows the RMSD between deformed pCT, uncorrected CBCT, $CBCT_{HM}$ and $CBCT_{HM\text{-}MLT}$. It can be seen that the differences after correction are lower than before, especially, after using the proposed approach which reduced the HU errors over the entire volume from 64.15 ± 9.50 to 51.20 ± 6.76 HU while for the previous approach based only on the HM the errors were reduced to 55.95 ± 10.43 HU.

Table 4.2: RMSD between the HU values of the deformed pCT, CBCT, $CBCT_{HM}$ and $CBCT_{HM\text{-}MLT}$ images for each patient with the mean and the standard deviation.

Patient's number	**CBCT**	**$CBCT_{HM}$**	**$CBCT_{HM\text{-}MLT}$**
1	71.03	64.70	56.32
2	57.89	49.10	42.39
3	73.58	65.17	57.80
4	65.76	55.10	50.96
5	67.48	55.73	51.58
6	82.09	77.88	72.93
7	57.74	47.26	43.90
8	54.89	45.74	42.52
9	51.82	45.90	44.10
10	59.29	52.92	49.50
Mean	**64.15**	**55.95**	**51.20**
SD	**9.50**	**10.43**	**6.76**

4.3.5 Tissue classes comparison

MAE between deformed pCT, CBCT, $CBCT_{HM}$ and $CBCT_{HM\text{-}MLT}$ for different tissue classes were calculated to have information about the localization of the higher errors and plotted in Figure 4.6. These plots indicate that performing MLT process after HM reduces the HU errors in the CBCT images. In addition, it improves the performance of HM to correct HU values in the soft tissue-air interfaces. The remaining errors observed in the soft tissue-air and soft tissue-bone interfaces are due to the misalignment between the deformed pCT and corrected CBCT images which is consistent with the visual assessment (Figure 4.3) and the profiles comparison (Figure 4.4).

4.4 Discussion

In this study the accuracy of a hybrid method combining two pCT-based approaches to correct HU distribution in CBCT images was evaluated. In contrast to other works where these two approaches were applied singularly for correcting CBCT images for dose calculation [6, 55, 57, 71, 72, 73, 74], our proposed method consisted of applying first a HM process, followed by MLT on CBCT images.

In comparison with our previously proposed workflow based only on HM [89], this combination allowed increasing the efficiency of the HM process to produce corrected CBCT images in a good agreement with the pCT images. The results presented in

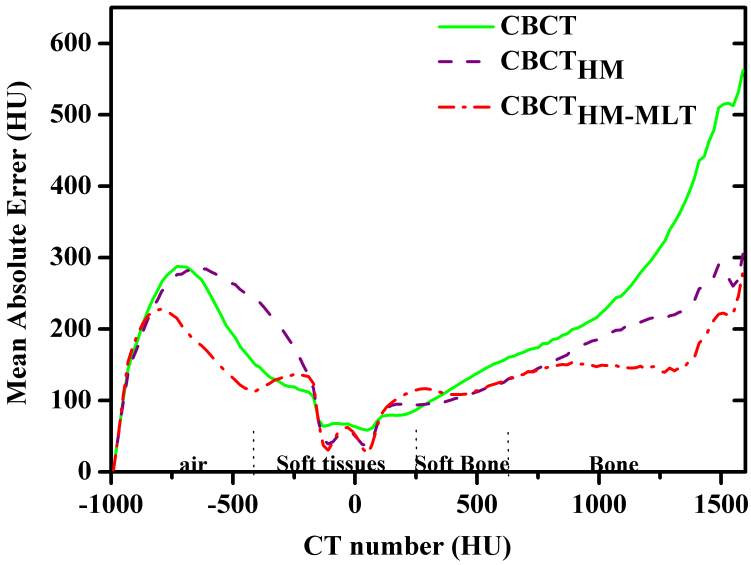

Figure 4.6: MAE between deformed pCT, uncorrected CBCT, $CBCT_{HM}$ and $CBCT_{HM\text{-}MLT}$.

Table 4.2 show a significant reduction in the HU error of about 13% when using only HM, whereas, the combination with MLT yielded a better enhancement of about 20%. Although a 7% error reduction over the entire volume seems insignificant, when focusing on bony regions with HU values higher than 1000 HU (Figure 4.6), the improvement was about 50%. Moreover, the application of MLT after HM improved the performance of the latter by reducing high discrepancies present in the soft tissue-air interfaces. The HU error reduction in these regions is particularly important considering that two main organs at risk in prostate cancer radiotherapy are femoral heads and rectum, across which the beams often pass. After the correction, a slight increase in the MAE values was observed in the soft tissue-bone interfaces. This may have been caused by the use of the mean box filter which resulted in the appearance of new HU values in the corrected CBCT images that do not exist in the pCT images.

In order to prevent the influence of HU uncertainty on the dose calculation, many studies proposed the use of deformed pCT instead of correcting the CBCT images [90, 91]. However, the robustness of such approaches is strongly dependent on the image registration quality and requires accurate DR algorithms to correctly propagate the contours between the pCT and the CBCT images. Marchant et al [8] reported that for prostate cancer the organs deformation errors related to the bladder filling and the gas bowels in the rectum may have a significant impact on the dose calculation than on the correction accuracy. For that reason, the deformed pCT images were used indirectly to correct the HU values and preserve the anatomical structures in the daily CBCT

images, which is the feature that distinguished this study from others. On the other hand, there are some limitations that should be taken into consideration. First, the limited FOV of CBCT systems remains an obstacle for ART based only on corrected CBCT images, especially for head and neck regions where the volumes of interest cannot be entirely covered by the used FOV. Second, since deformed pCT images may not constitute the best ground truth for comparison, due to its sensitivity to the image registration quality, a robust validation of the approach could be accomplished if the patients had undergone a daily fan beam CT images [51]. Furthermore, to provide a stronger validation for the proposed method we are looking forward to study the impact of HU error reduction on the dose calculation. Finally, for the use of MLT, five different tissue types were chosen in this study, while in [92] it was shown that the higher the number of classes the more accurate is the correction. Considering that increasing the number of classes may consequently increase the computation time, the automation of the proposed method and its testing under more efficient hardware architecture are currently being investigated for an online replanning process.

4.5 Conclusion

In this chapter, a hybrid approach combining two pCT-based approaches (HM followed by MLT) for the correction of CBCT images was evaluated using different statistical metrics. The obtained results showed that the use of HM+MLT correction improved the HU distribution in the CBCT images and generated corrected images in good agreement with the pCT. Thus, its implementation in clinical practice could be useful for CBCT-based dose calculation at online ART. However, moving toward online ART based only on CBCT images is not straightforward because all corrections studied in this thesis required the acquisition of pCT and CBCT images for each patient and the application of intra-patient image registration. To tackle this problem, we propose in the next chapter the generalization of our proposed approach by the investigation of pCT images already available in the archive for the correction of CBCT images instead of using the pCT images corresponding to the same patient.

Chapter 5

Generalization of the proposed method using an inter-patient image registration

5.1 Introduction

Recently, the idea of implementing full automated online treatment techniques has seen a special interest. Indeed, converging toward such applications in clinical routine warrants the need to reduce the workload requirements for online strategies, particularly, patient displacement between the imaging room (scanner) and the treatment room (linac). To reach this goal a new concept consisting of ART based only on CBCT images has appeared. This concept would delete the CT imaging completely from treatment workflow and keep just the CBCT images.
In this context, we propose in this chapter a new strategy allowing the correction of CBCT images without recourse to the acquisition of pCT images for each patient; instead of that, the use of the pCT images already available in the archive of our hospitals.

5.2 Methods

5.2.1 Description of the proposed approach

Until now, all proposed correction approaches were performed on pCT and CBCT images corresponding to the same patient after applying in this case what is called an intra-patient image registration. Unlike these approaches, the new correction strategy aims to adjust the HU distribution in the CBCT images acquired for one patient using

the HU values obtained from pCT images that was acquired for another patients after applying an inter-patient image registration. The proposed workflow is depicted in Figure 5.1 and it is based on two main steps that could be described as follows:

In the first step, one series of CBCT images was picked out from the 7 patients dataset for the correction. These images were referred to as the fixed image. Then, as described in chapter 4, to ensure a good alignment between the pCT and the CBCT images, the pCT images acquired for the 6 remaining patients, referred to as the moved images, were rigidly registered to the CBCT images using a 3D rigid transformation with MI as similarity metric. After that, to minimize the difference in organs deformation between the pCT and the CBCT images a multi-resolution B-spline transformation with NCC similarity metric was applied. Finally, the hybrid approach combining the HM with MLT proposed previously [93] was performed.

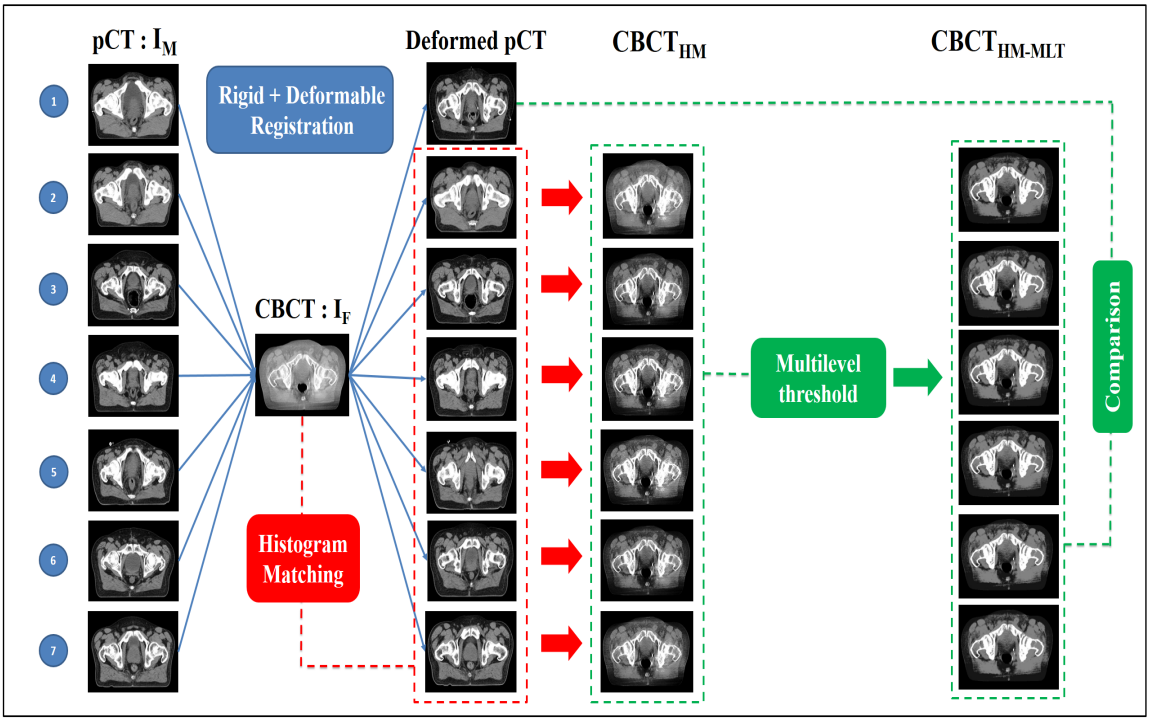

Figure 5.1: Generation of corrected CBCT images pipeline. Example of correcting the CBCT images of the first patient from the pCT images obtained for the remaining patients.

5.2.2 Evaluation

For comparison purposes, the correction accuracy evaluation was based on the same visual and statistic metrics presented in chapter 4. So that, to evaluate the quality of generated CBCT images the absolute differences between the pCT and the CBCT

images before and after correction as well as the extracted profiles according the same lines described previously were visualized and compared. Then, to quantify the agreement between the pCT and the corrected CBCT images the RMSD and the correlation values were calculated and compared.

5.3 Results

5.3.1 Visual assessment

Figure 5.2 and Figure A.1 (refer to appendix A) show the absolute difference between deformed pCT and CBCT images for the first and the 6 remaining patients, respectively. For each patient, the comparison between unprocessed and corrected CBCT images with HM+MLT process using the deformed pCT of the other 6 patients is presented. It is well noticeable that applying HM+MLT correction on the CBCT after using an inter-patient DR has reduced the amount of artefacts in the CBCT and yielded corrected images in good agreement with deformed pCT images compared to the unprocessed CBCT images. In addition, when comparing the results of applying inter-patient DR (e.g., $CBCT_{HM\text{-}MLT\ 1\text{-}2}$, $CBCT_{HM\text{-}MLT\ 1\text{-}3}$, $CBCT_{HM\text{-}MLT\ 1\text{-}4}$, $CBCT_{HM\text{-}MLT\ 1\text{-}5}$, $CBCT_{HM\text{-}MLT\ 1\text{-}6}$ and $CBCT_{HM\text{-}MLT\ 1\text{-}7}$) with those obtained from the intra-patient DR (from deformed pCT of the same patient), referred to as $CBCT_{HM\text{-}MLT\ 1\text{-}1}$; we observe that the resulted CBCT images are close in terms of quality. However, high differences in bony regions and soft tissue-air interfaces can be observed.

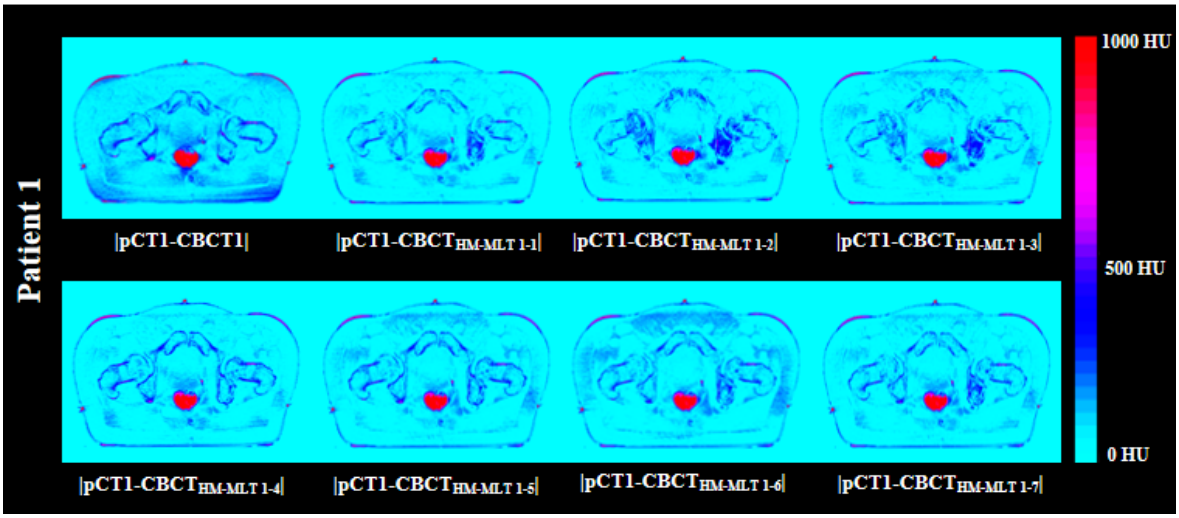

Figure 5.2: Absolute difference between deformed pCT and CBCT for five patients before correction and after correction using pCT images obtained for 6 other patients.

5.3.2 Profiles comparison

Figures 5.3-6 illustrate the extracted profiles at the four lines described in Figure 4.2 for one representative patient. It can be seen that before correction the profiles of the CBCT images are not very close to those of deformed pCT. However, after correction the profiles of corrected CBCT achieve the same values as in the pCT images, especially, the picks representing the bony regions. Moreover, the sensitivity of the correction quality to non-comparable regions as regions of gas in the pCT and CBCT images can be marked. For example, in the Figure 5.3 where the line 1 went through a gas region, the correction of HU distribution was not clearly observed in contradiction to the remaining lines (Figures 5.4-6) for which no gas regions were present. In addition, The comparison of the obtained profiles when using inter-patient DR with those obtained after applying an intra-patient DR shows that both approaches present insignificant differences.

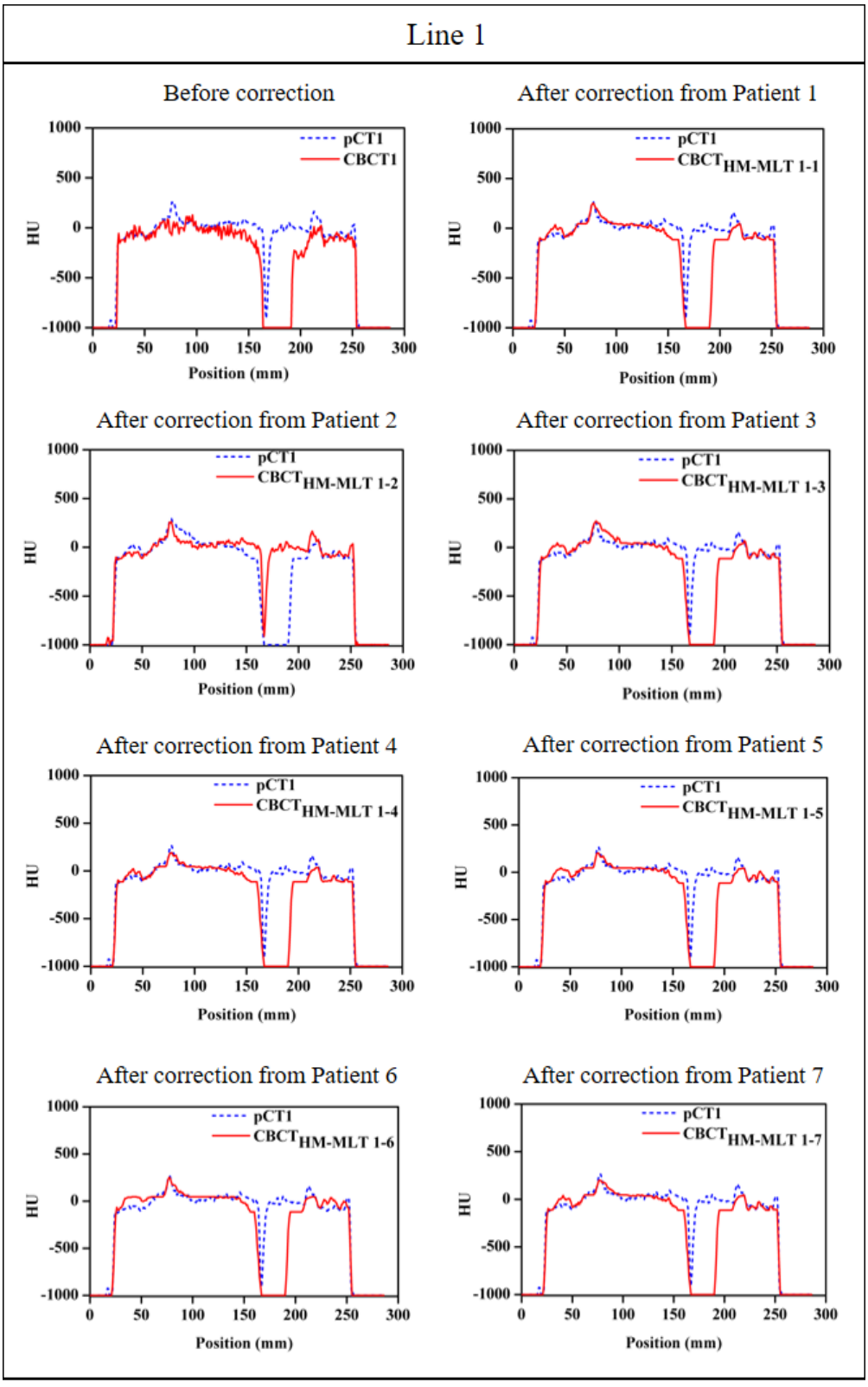

Figure 5.3: Comparison of Hounsfield Units between deformed pCT and CBCT images of the first patient before correction and after correction from the pCT of different patients along the first line.

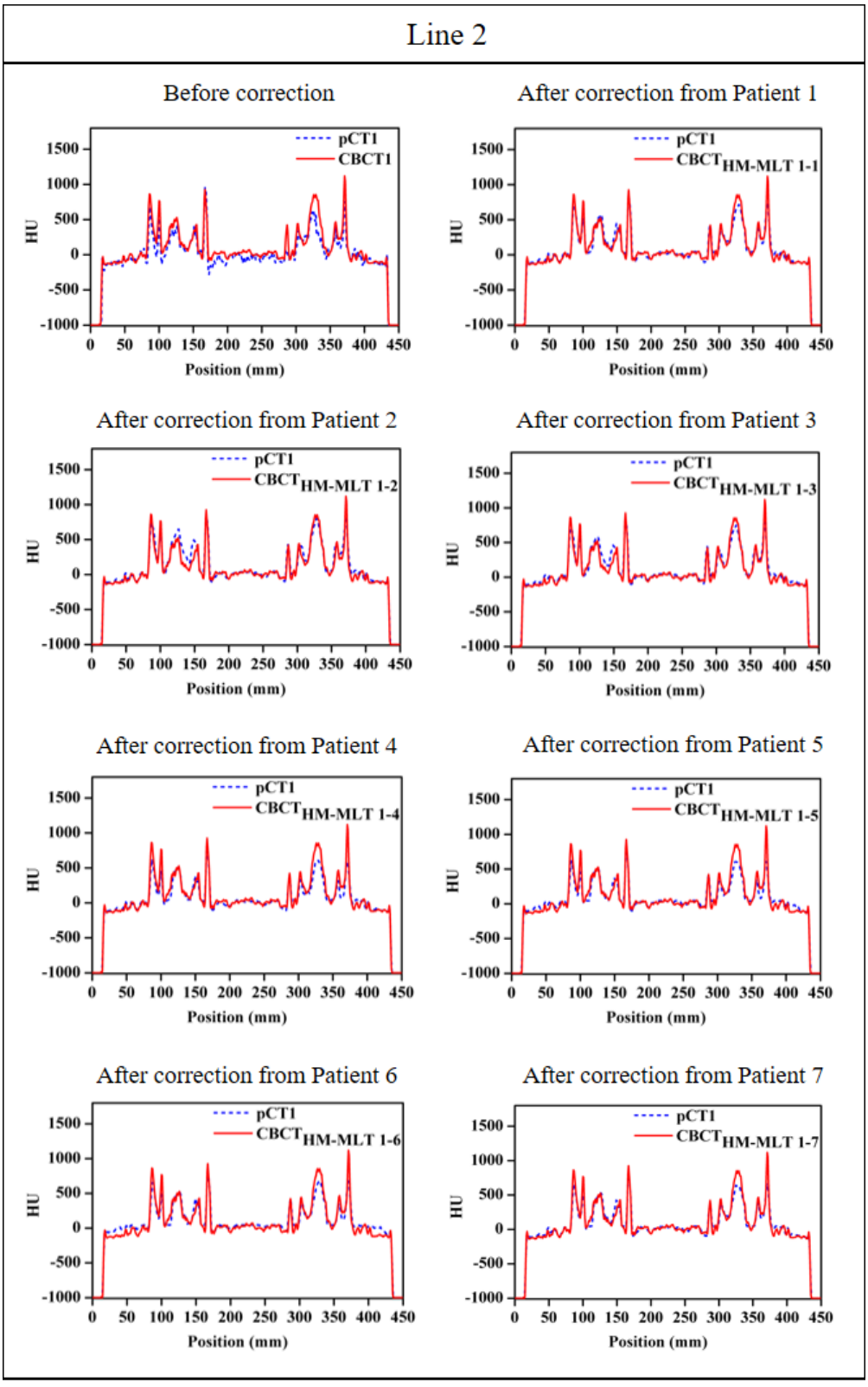

Figure 5.4: Comparison of Hounsfield Units between deformed pCT and CBCT images of the first patient before correction and after correction from the pCT of different patients along the second line.

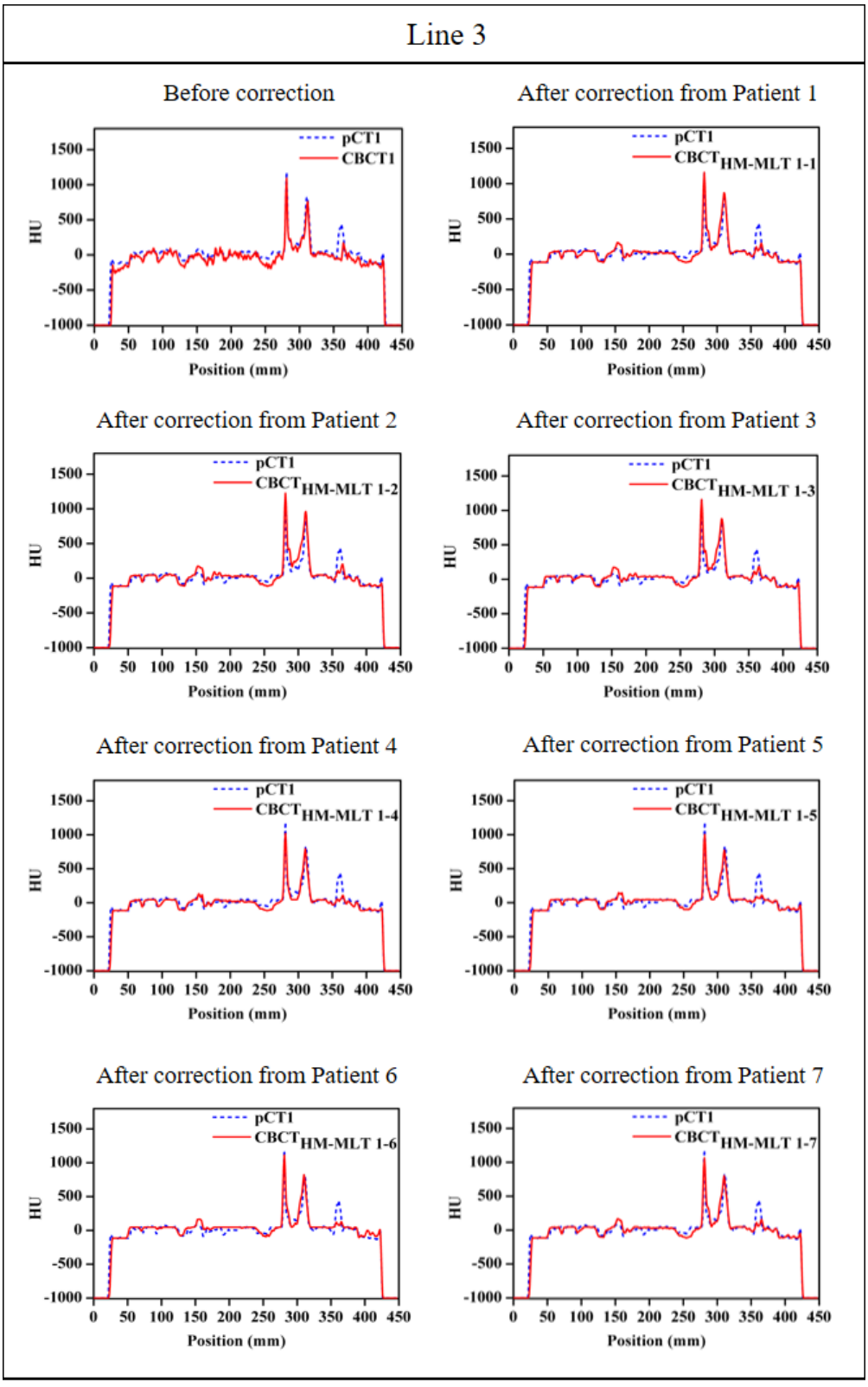

Figure 5.5: Comparison of Hounsfield Units between deformed pCT and CBCT images of the first patient before correction and after correction from the pCT of different patients along the third line.

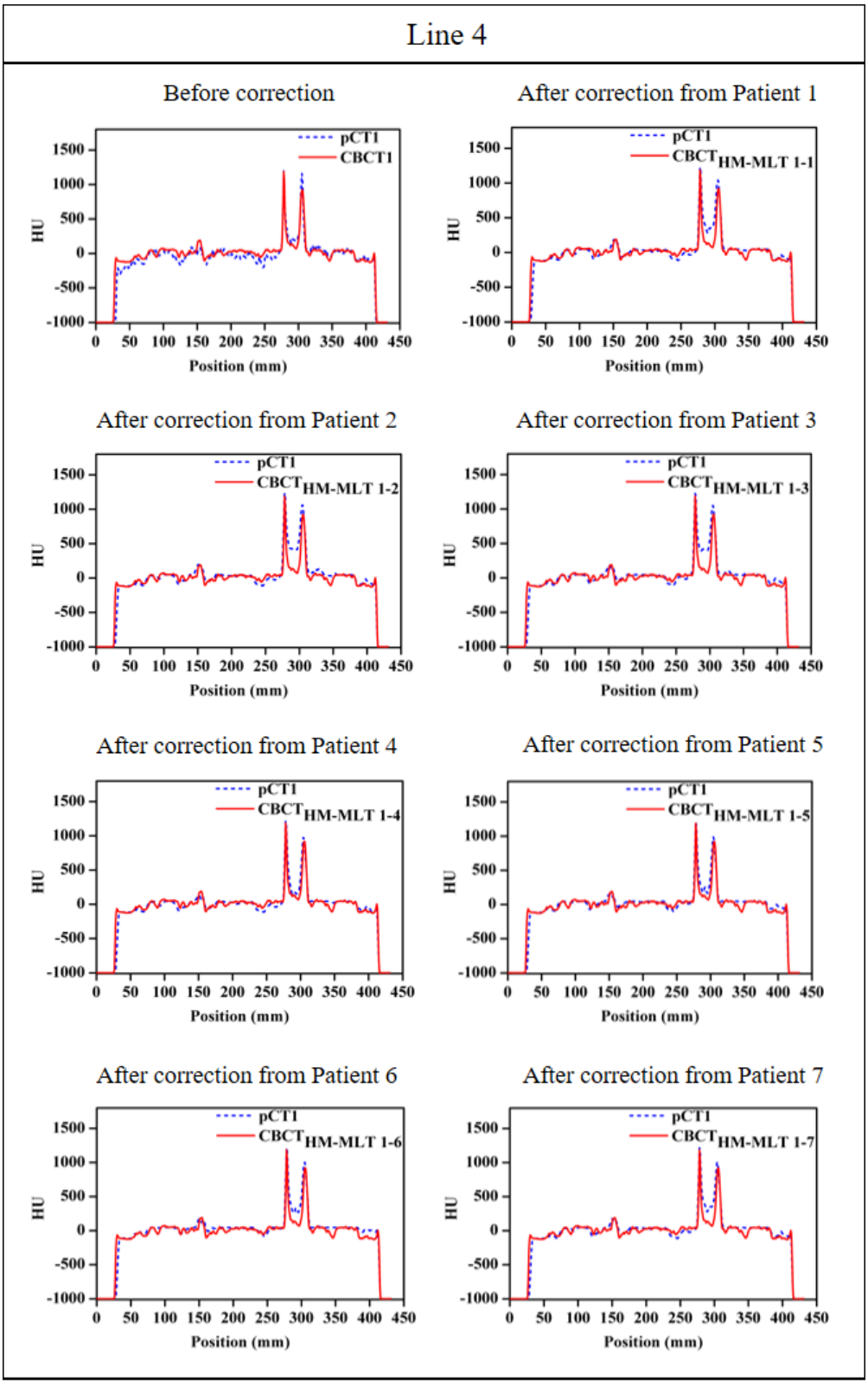

Figure 5.6: Comparison of Hounsfield Units between deformed pCT and CBCT images of the first patient before correction and after correction from the pCT of different patients along the forth line.

5.3.3 Volumes Comparison

Results of volumes comparison for each patient in terms of HU average error between deformed pCT and CBCT before and after correction are shown in Table 5.1. The mean and the standard deviation are also presented. The largest magnitude of V_{err} is observed for unprocessed CBCT images. When using HM+MLT correction after inter-patient DR the mean HU error value of all the patients was significantly reduced. For example, errors for the first patient were reduced from 71.03 HU to 55.92 $\pm$ 0.89 HU. Furthermore, some exceptional cases were observed for which the errors became higher ; e.g., the correction of the CBCT4 and CBCT6 from the deformed pCT2 passed from 82.09 HU to 88.35 HU and from 54.89 HU to 61.54 HU, respectively. This is due to high differences in the anatomical distribution between these patients and that can not be deformed correctly by the used algorithm. Finally, when comparing the results of correction based on the deformed pCT of the same patient and those of the other patients no significant differences can be observed.

Table 5.1: HU average error values between deformed pCT and CBCT images before and after correction for each patient. In bold, the mean and the standard deviation. Values in red represent the HU error when correcting CBCT images from the pCT corresponding to the same patient with the percentage of change.

	Before correction	**After correction**								
		pCT 1	**pCT 2**	**pCT 3**	**pCT 4**	**pCT 5**	**pCT 6**	**pCT 7**	**Mean**	**SD**
CBCT 1	71.03	53.82 (-24%)	57.02	55.73	54.98	56.01	57.41	54.37	**55.92 (-21%)**	**0.89**
CBCT 2	65.76	48.39	48.25 (-26%)	47.89	52.71	50.88	50.91	48.75	**49.92 (-24%)**	**1.57**
CBCT 3	67.48	54.08	56.03	53.82 (-20%)	54.04	54.28	55.19	54.24	**54.64 (-19%)**	**0.64**
CBCT 4	82.09	82.21	88.35	82.77	75.90 (+7%)	77.95	81.65	79.18	**82.01 (0.09%)**	**2.42**
CBCT 5	57.74	45.65	57.23	47.56	43.01	42.44 (-26%)	44.23	46.79	**47.41 (-17%)**	**3.32**
CBCT 6	54.89	48.04	61.54	49.97	45.69	43.82	42.55 (-22%)	48.25	**49.55 (-9%)**	**4.13**
CBCT 7	59.29	48.23	57.21	51.76	47.88	48.22	57.68	58.81 (-0.8%)	**51.33 (-13%)**	**3.22**

5.3.4 Correlation

Figure 5.7 represents the results of correlation between CBCT and deformed CT images before and after correction for all the patients. For this metric the optimum is reached

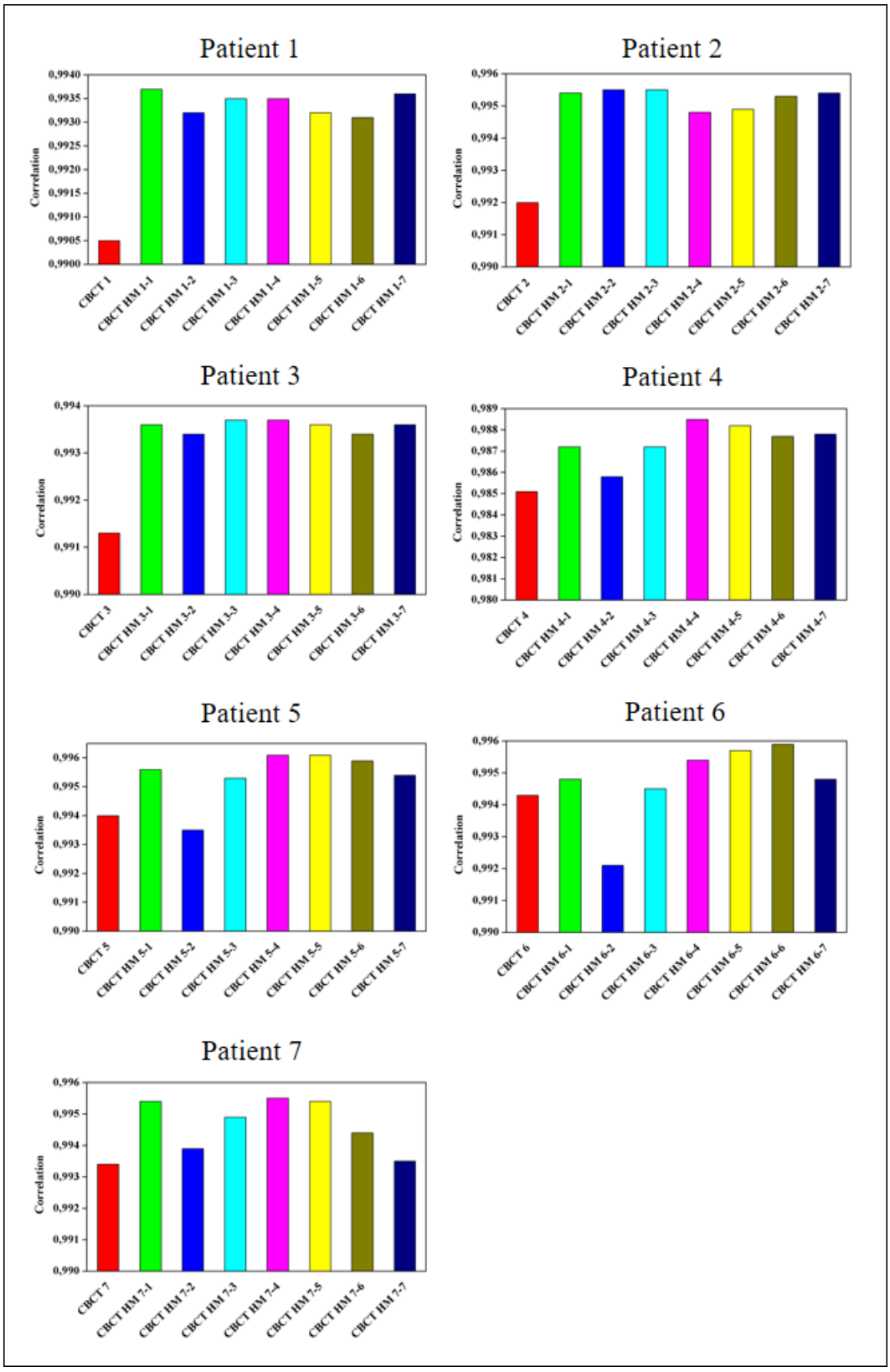

Figure 5.7: Correlation values between deformed pCT, uncorrected CBCT and CBCT after correction for each patient.

for the value 1. We observe that before correction the values of correlation are lower; while after correction the correlation became better with values close to 1 indicating that the resulted CBCT images are in good agreement with the pCT. However, in some cases this agreement was not reached due to the mis-alignment between the different structures present in the CBCT and pCT images ; we cite for example : the correction of the CBCT4, CBCT5, CBCT6 and CBCT7 with pCT2. Moreover, the comparison with the results of using intra-patient DR showed that the use of inter-patient DR yielded approximately the same values, confirming that this last can be used instead of intra-patient DR.

5.4 Discussion

In this chapter, an extension of our previously proposed approach was presented. It aimed to study the performances of applying the hybrid correction approach after using an inter-patient image registration. The uniqueness of this work compared to other studies [6, 89] lies on the investigation of pCT images that are already available in the archive instead of acquiring new ones.

All the obtained results confirmed that the use of inter-patient DR work well as intra-patient DR. The used statistical analysis showed that the percentages of change obtained from these two strategies are approximately the same (e.g., for the first patient, the use of intra-patient DR showed a reduction in the HU error of about 24% while the inter-patient DR yielded a reduction of about 21%). These findings indicate that our proposed strategy can effectively generate corrected CBCT images from the pCT images of different patients in the same way as the use of pCT images corresponding to the same patient. However, as shown in Table 5.1 and Figure 5.7, there were some exceptional cases (e.g., all the corrections performed from the data of the second patient) where the correct HU distribution was not successfully reached due to the high differences in anatomical distribution between the chosen patients which proves the dependency of this strategy to the choice of the pCT images from which the correction will be performed. To deal with this limitation, the construction of a library containing pCT images for several patients with the same properties (age, shape, diagnosis,etc.) is needed. This implies the inclusion of expert radio-oncologists allowing the classification of the different cases present in the archive. Moreover, to avoid the dependency to the patient choice, performing the correction from the pCT representing the mean of all pCT images in the library is another idea that should be adopted in further studies.

5.5 Conclusion

In this study we have demonstrated and validated a strategy that can investigate a library containing pCT images for the correction of CBCT images using the concept of inter-patient DR. We consider that the implementation of our method will contribute to the reduction of the workload requirements for online ART, particularly, the repeated acquisition of pCT images. However, further studies investigating the feasibility of this strategy in terms of dose calculation should be conducted to strengthen its validation.

Conclusions and Perspectives

In modern radiotherapy techniques, the use of medical imaging has dramatically increased; this increase has been made possible thanks to the integration of in-room imaging systems which allowed controlling the evolution and the localization of treated volumes before, during and after the treatment. One of the most widely used in-room imaging for image guidance is the CBCT. Its sufficient contrast and fast acquisition as well as its availability in the treatment room make of it a subject of several studies that aims to investigate these images not only for guidance but also for dose calculation in the context of ART. The one common goal for these studies is to propose promising strategies to overcome all limitation related to the high amount of scatter that reduces the quality of CBCT images and causes a lack of HU accuracy compared to the CT images.

In this thesis, we performed a review of these studies and classified them into four classes in order to analyze their strengths and limitations to eventually propose three main approaches for the correction of CBCT images using pCT data. The first proposed approach is inspired from the fact that the CBCT and the pCT images have not the same gray-level histograms. Therefore, we applied the HM process to resemble their histograms and offer the possibility to distinguish the different tissue types in the CBCT images. It has been found that this process contributed significantly to reduce the HU errors in the CBCT images. Furthermore, to improve the correctness of the HU distribution obtained with HM, we proposed as a second approach the application of MLT. The combination of these two pCT-based approaches (HM followed by MLT) has allowed increasing the efficiency of the HM process to produce corrected CBCT images in good agreement with the pCT images. Finally, in the third approach we proposed the generalization of the previously proposed approaches to contribute in the minimization of the ART workload requirements. The adoption of inter-patient DR instead of intra-patient DR for the correction of CBCT images yielded approximately the same results and could be a promising way towards the creation of pCT library for the correction rather than repeating the acquisition of this later.

Despite the success of the proposed methods in the generation of corrected CBCT

images, there are still many limitations that prevent its use for ART based only on CBCT images. Among them we cite: the limited FOV of the CBCT systems that remains an obstacle in the case of regions where the volumes of interest cannot be entirely covered. Also, the presence of non-comparable regions in the CBCT and the pCT images, e.g. regions of gas in the rectum, is a key limitation that may influence the DR accuracy. Besides, the required computation time to complete the correction process remains a main limiting factor. Finally, a dosimetric evaluation is still needed to reinforce the validation of the proposed approaches. Therefore, to overcome these limitations, further studies taking into consideration the following points should be performed:

- Development of a fusion process allowing the combination of two longitudinal consecutive acquisitions, in order to reconstitute the whole volume and provide a large FOV;
- Automation of the proposed method and its testing under more efficient hardware architecture;
- Evaluation of the HU error reduction effect on the dose calculation in order to provide a stronger validation;
- Application of the proposed approaches on a large number of patients and its translation to other body regions.

Contributions

1. The first contribution is an evaluation of different CT to CBCT deformable registration algorithms. It helped to define the appropriate parameters allowing the better alignment between anatomical structures in the CT and CBCT images.
2. The second contribution is an assessment of the choice of DR algorithm on the accuracy of CBCT correction by HM . It demonstrated that the better the registration the more accurate the correction is.
3. The third contribution is hybrid approach combining the HM with MLT approaches. This contribution helped to improve the performances of HM to correct the HU distribution in CBCT images.
4. The fourth contribution is a generalization of the proposed hybrid approach. It demonstrated the usefulness of inter-patient DR for the correction of CBCT images of new patients.

Bibliography

[1] Weihua Fu, Yong Yang, Ning J Yue, Dwight E Heron, and M Saiful Huq. A cone beam ct-guided online plan modification technique to correct interfractional anatomic changes for prostate cancer imrt treatment. *Physics in Medicine & Biology*, 54(6):1691, 2009.

[2] Ergun E Ahunbay, Cheng Peng, Shannon Holmes, Andrew Godley, Colleen Lawton, and X Allen Li. Online adaptive replanning method for prostate radiotherapy. *International Journal of Radiation Oncology* Biology* Physics*, 77(5):1561–1572, 2010.

[3] Catarina Veiga, Jamie McClelland, Syed Moinuddin, Ana Lourenço, Kate Ricketts, James Annkah, Marc Modat, Sébastien Ourselin, Derek D'Souza, and Gary Royle. Toward adaptive radiotherapy for head and neck patients: feasibility study on using ct-to-cbct deformable registration for dose of the day calculations. *Medical physics*, 41(3), 2014.

[4] Masahiro Endo, Takanori Tsunoo, Nobuyuki Nakamori, and Katsuya Yoshida. Effect of scattered radiation on image noise in cone beam ct. *Medical physics*, 28(4):469–474, 2001.

[5] Mathilda van Zijtveld, Maarten Dirkx, and Ben Heijmen. Correction of conebeam ct values using a planning ct for derivation of the dose of the day. *Radiotherapy and Oncology*, 85(2):195–200, 2007.

[6] Yusuke Onozato, Noriyuki Kadoya, Yukio Fujita, Kazuhiro Arai, Suguru Dobashi, Ken Takeda, Kazuma Kishi, Rei Umezawa, Haruo Matsushita, and Keiichi Jingu. Evaluation of on-board kv cone beam computed tomography–based dose calculation with deformable image registration using hounsfield unit modifications. *International Journal of Radiation Oncology* Biology* Physics*, 89(2):416–423, 2014.

[7] Guy Amit and Thomas G Purdie. Automated planning of breast radiotherapy using cone beam ct imaging. *Medical physics*, 42(2):770–779, 2015.

[8] Thomas E Marchant, Kiran D Joshi, and Christopher J Moore. Accuracy of radiotherapy dose calculations based on cone-beam ct: comparison of deformable registration and image correction based methods. *Physics in Medicine & Biology*, 63(6):065003, 2018.

[9] Satoshi Kida, Takahiro Nakamoto, Masahiro Nakano, Kanabu Nawa, Akihiro Haga, Jun'ichi Kotoku, Hideomi Yamashita, and Keiichi Nakagawa. Cone beam computed tomography image quality improvement using a deep convolutional neural network. *Cureus*, 10(4), 2018.

[10] Uros Stankovic, Marcel van Herk, Lennert S Ploeger, and Jan-Jakob Sonke. Improved image quality of cone beam ct scans for radiotherapy image guidance using fiber-interspaced antiscatter grid. *Medical physics*, 41(6Part1):061910, 2014.

[11] A Sisniega, Wojciech Zbijewski, J Xu, H Dang, Joseph Webster Stayman, J Yorkston, Nafi Aygun, V Koliatsos, and JH Siewerdsen. High-fidelity artifact correction for cone-beam ct imaging of the brain. *Physics in Medicine & Biology*, 60(4):1415, 2015.

[12] Ulrik V Elstrøm, Sune RK Olsen, Ludvig P Muren, Jørgen BB Petersen, and Cai Grau. The impact of cbct reconstruction and calibration for radiotherapy planning in the head and neck region–a phantom study. *Acta Oncologica*, 53(8):1114–1124, 2014.

[13] ICRU. *Prescribing, recording, and reporting photon beam therapy, Report 50.* International Commission on Radiation, 1993.

[14] ICRU. *Prescribing, recording, and reporting photon beam therapy (supplement to ICRU report 50), Report 62.* International Commission on Radiation, 1999.

[15] ICRU. *Prescribing, recording, and reporting photon beam therapy, Report 83.* International Commission on Radiation, 2010.

[16] C Durdux, J E Bibault, and F Jaffré. Principes et techniques de la radiothrapie thoracique des carcinomes bronchiques non petites cellules (cbnpc). *Revue des Maladies Respiratoires Actualits*, 10:303–316, 2018.

[17] Christine Boydev. *Automatic segmentation of cone-beam computed tomography images for prostate cancer radiation therapy.* PhD thesis, Université de Valenciennes et du Hainaut-Cambresis, 2015.

[18] Branislav Jeremić. *Advances in radiation oncology in lung cancer.* Springer, 2011.

[19] JL Meyer, S Leibel, M Roach, and S Vijayakumar. New technologies for the radiotherapy of prostate cancer. In *IMRT, IGRT, SBRT-Advances in the Treatment Planning and Delivery of Radiotherapy*, volume 40, pages 315–337. Karger Publishers, 2007.

[20] Yasumasa Nishimura and Ritsuko Kamaki. *Intensity modulated radiation therapy: clinical evidence and techniques*. Springer, 2015.

[21] Thomas Bortfeld, Wilfried Neve, Rupert Schmidt-Ullrich, and David E Wazer. *Image-guided IMRT*. Springer, 2006.

[22] Anders Brahme, J-E Roos, and Ingemar Lax. Solution of an integral equation encountered in rotation therapy. *Physics in Medicine & Biology*, 27(10):1221, 1982.

[23] David A Palma, Wilko FAR Verbakel, Karl Otto, and Suresh Senan. New developments in arc radiation therapy: a review. *Cancer treatment reviews*, 36(5):393–399, 2010.

[24] S Webb and D McQuaid. Some considerations concerning volume-modulated arc therapy: a stepping stone towards a general theory. *Physics in Medicine and Biology*, 54(14):4345, 2009.

[25] SA Bhide and CM Nutting. Recent advances in radiotherapy. *BMC medicine*, 8(1):25, 2010.

[26] Hans Geinitz, Mack Roach III, and Nicholas Van As. *Radiotherapy in Prostate Cancer*. Springer, 2016.

[27] Sue Chua. *PET/CT in Radiotherapy Planning*. Springer, 2017.

[28] Laura Pisani, David Lockman, David Jaffray, Di Yan, Alvaro Martinez, and John Wong. Setup error in radiotherapy: on-line correction using electronic kilovoltage and megavoltage radiographs. *International Journal of Radiation Oncology, Biology and Physics*, 47(3):825–839, 2000.

[29] Kristy K Brock. *Image processing in radiation therapy*. CRC Press, 2013.

[30] Di Yan and Jian Liang. Expected treatment dose construction and adaptive inverse planning optimization: implementation for offline head and neck cancer adaptive radiotherapy. *Medical physics*, 40(2):021719, 2013.

[31] Joel Castelli, Antoine Simon, Guillaume Louvel, Olivier Henry, Enrique Chajon, Mohamed Nassef, Pascal Haigron, Guillaume Cazoulat, Juan David Ospina, Franck Jegoux, et al. Impact of head and neck cancer adaptive radiotherapy to spare the parotid glands and decrease the risk of xerostomia. *Radiation Oncology*, 10(1):6, 2015.

[32] Chuan Wu, Robert Jeraj, Weiguo Lu, and Thomas R Mackie. Fast treatment plan modification with an over-relaxed cimmino algorithm. *Medical physics*, 31(2):191–200, 2004.

[33] Laurence E Court, Lei Dong, Andrew K Lee, Rex Cheung, Mark D Bonnen, Jennifer ODaniel, He Wang, Radhe Mohan, and Deborah Kuban. An automatic ct-guided adaptive radiation therapy technique by online modification of multileaf collimator leaf positions for prostate cancer. *International Journal of Radiation Oncology* Biology* Physics*, 62(1):154–163, 2005.

[34] Ergun E Ahunbay, Cheng Peng, Guang-Pei Chen, Sreeram Narayanan, Cedric Yu, Colleen Lawton, and X Allen Li. An on-line replanning scheme for interfractional variations a. *Medical physics*, 35(8):3607–3615, 2008.

[35] Sean Collins, Siyan Lei, Nathaniel Piel, Eric K Oermann, Viola J Chen, Andrew W Ju, Kedar N Dahal, Heather N Hanscom, Joy S Kim, Xia Yu, et al. Six-dimensional correction of intra-fractional prostate motion with cyberknife stereotactic body radiation therapy. *Frontiers in oncology*, 1:48, 2011.

[36] Tobias Pommer, Marianne Falk, Per R Poulsen, Paul J Keall, Ricky T O'Brien, Peter Meidahl Petersen, and Per Munck af Rosenschöld. Dosimetric benefit of dmlc tracking for conventional and sub-volume boosted prostate intensity-modulated arc radiotherapy. *Physics in Medicine & Biology*, 58(7):2349, 2013.

[37] E Colvill, Per Rugaard Poulsen, JT Booth, RT O'Brien, JA Ng, and PJ Keall. Dmlc tracking and gating can improve dose coverage for prostate vmat. *Medical physics*, 41(9):091705, 2014.

[38] Stefan Klein, Marius Staring, Keelin Murphy, Max A Viergever, and Josien PW Pluim. Elastix: a toolbox for intensity-based medical image registration. *IEEE transactions on medical imaging*, 29(1):196–205, 2009.

[39] Paul J Keall, Sarang Joshi, S Sastry Vedam, Jeffrey V Siebers, Vijaykumar R Kini, and Radhe Mohan. Four-dimensional radiotherapy planning for dmlc-based respiratory motion tracking. *Medical physics*, 32(4):942–951, 2005.

[40] Eike Rietzel, George TY Chen, Noah C Choi, and Christopher G Willet. Four-dimensional image-based treatment planning: Target volume segmentation and dose calculation in the presence of respiratory motion. *International Journal of Radiation Oncology* Biology* Physics*, 61(5):1535–1550, 2005.

[41] Lei Dong and Arthur L Boyer. An image correlation procedure for digitally reconstructed radiographs and electronic portal images. *International Journal of Radiation Oncology Biology Physics*, 33(5):1053–1060, 1995.

[42] EE Fitchard, JS Aldridge, PJ Reckwerdt, and TR Mackie. Registration of synthetic tomographic projection data sets using cross-correlation. *Physics in Medicine & Biology*, 43(6):1645, 1998.

[43] Frederik Maes, Dirk Vandermeulen, and Paul Suetens. Comparative evaluation of multiresolution optimization strategies for multimodality image registration by maximization of mutual information. *Medical image analysis*, 3(4):373–386, 1999.

[44] Jeongtae Kim, Jeffrey A Fessler, Kwok L Lam, James M Balter, and Randall K Ten Haken. A feasibility study of mutual information based setup error estimation for radiotherapy. *Medical Physics*, 28(12):2507–2517, 2001.

[45] Daniel Rueckert and Julia A Schnabel. Medical image registration. In *Biomedical image processing*, pages 131–154. Springer, 2010.

[46] David A Jaffray, Jeffrey H Siewerdsen, John W Wong, and Alvaro A Martinez. Flat-panel cone-beam computed tomography for image-guided radiation therapy. *International Journal of Radiation Oncology, Biology and Physics*, 53(5):1337–1349, 2002.

[47] Rune Slot Thing. *Dose calculation based on Cone Beam CT images*. PhD thesis, University of Southern Denmark, 2016.

[48] Bruno De Man, Johan Nuyts, Patrick Dupont, Guy Marchal, and Paul Suetens. Metal streak artifacts in x-ray computed tomography: a simulation study. *IEEE Transactions on Nuclear Science*, 46(3):691–696, 1999.

[49] Bruno De Man and Samit Basu. Distance-driven projection and backprojection in three dimensions. *Physics in Medicine & Biology*, 49(11):2463, 2004.

[50] R Schulze, U Heil, D Groβ, DD Bruellmann, E Dranischnikow, U Schwanecke, and E Schoemer. Artefacts in cbct: a review. *Dentomaxillofacial Radiology*, 40(5):265–273, 2011.

[51] Yong Yang, Eduard Schreibmann, Tianfang Li, Chuang Wang, and Lei Xing. Evaluation of on-board kv cone beam ct (cbct)-based dose calculation. *Physics in Medicine & Biology*, 52(3):685, 2007.

[52] Anne Richter, Qiaoqiao Hu, Doreen Steglich, Kurt Baier, Jürgen Wilbert, Matthias Guckenberger, and Michael Flentje. Investigation of the usability of conebeam ct data sets for dose calculation. *Radiation Oncology*, 3(1):42, 2008.

[53] S Schafer, J W. Stayman, Wojciech Zbijewski, C Schmidgunst, G Kleinszig, and J H. Siewerdsen. Antiscatter grids in mobile c-arm cone-beam ct: effect on image quality and dose. *Medical physics*, 39(1):153–159, 2012.

[54] Yuan Xu, Ti Bai, Hao Yan, Luo Ouyang, Arnold Pompos, Jing Wang, Linghong Zhou, Steve B Jiang, and Xun Jia. A practical cone-beam ct scatter correction method with optimized monte carlo simulations for image-guided radiation therapy. *Physics in Medicine & Biology*, 60(9):3567, 2015.

[55] Shifeng Chen, Quynh Le, Yildirim Mutaf, Wei Lu, Elizabeth M Nichols, Byong Yong Yi, Tish Leven, Karl L Prado, and Warren D D'Souza. Feasibility of cbct-based dose with a patient-specific stepwise hu-to-density curve to determine time of replanning. *Journal of applied clinical medical physics*, 18(5):64–69, 2017.

[56] Michael MacFarlane, Daniel Wong, Douglas A Hoover, Eugene Wong, Carol Johnson, Jerry J Battista, and Jeff Z Chen. Patient-specific calibration of cone-beam computed tomography data sets for radiotherapy dose calculations and treatment plan assessment. *Journal of applied clinical medical physics*, 19(2):249–257, 2018.

[57] Turki Almatani, Richard P Hugtenburg, Ryan D Lewis, Susan E Barley, and Mark A Edwards. Automated algorithm for cbct-based dose calculations of prostate radiotherapy with bilateral hip prostheses. *The British journal of radiology*, 89(1066):20160443, 2016.

[58] Daniel Létourneau, Rebecca Wong, Douglas Moseley, Michael B Sharpe, Stephen Ansell, Mary Gospodarowicz, and David A Jaffray. Online planning and delivery technique for radiotherapy of spinal metastases using cone-beam ct: image quality and system performance. *International Journal of Radiation Oncology* Biology* Physics*, 67(4):1229–1237, 2007.

[59] Lei Zhu, Yaoqin Xie, Jing Wang, and Lei Xing. Scatter correction for cone-beam ct in radiation therapy. *Medical physics*, 36(6Part1):2258–2268, 2009.

[60] Jian-Yue Jin, Lei Ren, Qiang Liu, Jinkoo Kim, Ning Wen, Huaiqun Guan, Benjamin Movsas, and Indrin J Chetty. Combining scatter reduction and correction to improve image quality in cone-beam computed tomography (cbct). *Medical physics*, 37(11):5634–5644, 2010.

[61] Geneviève Jarry, Sean A Graham, Douglas J Moseley, David J Jaffray, Jeffrey H Siewerdsen, and Frank Verhaegen. Characterization of scattered radiation in kv cbct images using monte carlo simulations. *Medical physics*, 33(11):4320–4329, 2006.

[62] Ernesto Mainegra-Hing and Iwan Kawrakow. Fast monte carlo calculation of scatter corrections for cbct images. In *Journal of Physics: Conference Series*, volume 102, page 012017. IOP Publishing, 2008.

[63] Rune Slot Thing and Ernesto Mainegra-Hing. Optimizing cone beam ct scatter estimation in egs_cbct for a clinical and virtual chest phantom. *Medical physics*, 41(7):071902, 2014.

[64] GJ Bootsma, Frank Verhaegen, and DA Jaffray. Efficient scatter distribution estimation and correction in cbct using concurrent monte carlo fitting. *Medical physics*, 42(1):54–68, 2015.

[65] Rune Slot Thing, Uffe Bernchou, Ernesto Mainegra-Hing, Olfred Hansen, and Carsten Brink. Hounsfield unit recovery in clinical cone beam ct images of the thorax acquired for image guided radiation therapy. *Physics in Medicine & Biology*, 61(15):5781, 2016.

[66] Rune Slot Thing, Uffe Bernchou, Olfred Hansen, and Carsten Brink. Accuracy of dose calculation based on artefact corrected cone beam ct images of lung cancer patients. *Physics and Imaging in Radiation Oncology*, 1:6–11, 2017.

[67] Joan Hatton, Boyd McCurdy, and Peter B Greer. Cone beam computerized tomography: the effect of calibration of the hounsfield unit number to electron density on dose calculation accuracy for adaptive radiation therapy. *Physics in Medicine & Biology*, 54(15):N329, 2009.

[68] Kavitha Srinivasan, Mohammad Mohammadi, and Justin Shepherd. Cone beam computed tomography for adaptive radiotherapy treatment planning. *Journal of Medical and Biological Engineering*, 34(4):377–385, 2014.

[69] Mariska de Smet, Danny Schuring, Sebastiaan Nijsten, and Frank Verhaegen. Accuracy of dose calculations on kv cone beam ct images of lung cancer patients. *Medical physics*, 43(11):5934–5941, 2016.

[70] Kazuhiro Arai, Noriyuki Kadoya, Takahiro Kato, Hiromitsu Endo, Shinya Komori, Yoshitomo Abe, Tatsuya Nakamura, Hitoshi Wada, Yasuhiro Kikuchi, Yoshihiro Takai, et al. Feasibility of cbct-based proton dose calculation using a histogram-matching algorithm in proton beam therapy. *Physica Medica*, 33:68–76, 2017.

[71] Ramesh Boggula, Friedlieb Lorenz, Yasser Abo-Madyan, Frank Lohr, Dirk Wolff, Judit Boda-Heggemann, Juergen Hesser, Frederik Wenz, and Hansjoerg Wertz. A new strategy for online adaptive prostate radiotherapy based on cone-beam ct. *Zeitschrift für Medizinische Physik*, 19(4):264–276, 2009.

[72] Irina Fotina, Johannes Hopfgartner, Markus Stock, Thomas Steininger, Carola Lütgendorf-Caucig, and Dietmar Georg. Feasibility of cbct-based dose calculation: comparative analysis of hu adjustment techniques. *Radiotherapy and Oncology*, 104(2):249–256, 2012.

[73] Alex Dunlop, Dualta McQuaid, Simeon Nill, Julia Murray, Gavin Poludniowski, Vibeke N Hansen, Shreerang Bhide, Christopher Nutting, Kevin Harrington, Kate Newbold, et al. Comparison of ct number calibration techniques for cbct-based dose calculation. *Strahlentherapie und Onkologie*, 191(12):970–978, 2015.

[74] Valentina Giacometti, Raymond B King, Christina E Agnew, Denise M Irvine, Suneil Jain, Alan R Hounsell, and Conor K McGarry. An evaluation of techniques for dose calculation on cone beam computed tomography. *The British journal of radiology*, 92(1096):20180383, 2019.

[75] Philippe Meyer, Vincent Noblet, Christophe Mazzara, and Alex Lallement. Survey on deep learning for radiotherapy. *Computers in biology and medicine*, 98:126–146, 2018.

[76] Luca Boldrini, Jean-Emmanuel Bibault, Carlotta Masciocchi, Yanting Shen, and Martin-Immanuel Bittner. Deep learning: a review for the radiation oncologist. *Frontiers in Oncology*, 9:977, 2019.

[77] Mark Cicero, Alexander Bilbily, Errol Colak, Tim Dowdell, Bruce Gray, Kuhan Perampaladas, and Joseph Barfett. Training and validating a deep convolutional neural network for computer-aided detection and classification of abnormalities on frontal chest radiographs. *Investigative radiology*, 52(5):281–287, 2017.

[78] Kenny H Cha, Lubomir Hadjiiski, Ravi K Samala, Heang-Ping Chan, Elaine M Caoili, and Richard H Cohan. Urinary bladder segmentation in ct urography using deep-learning convolutional neural network and level sets. *Medical physics*, 43(4):1882–1896, 2016.

[79] S Kida, S Kaji, K Nawa, T Imae, T Nakamoto, S Ozaki, T Ohta, Y Nozawa, and K Nakagawa. Cone-beam ct to planning ct synthesis using generative adversarial networks. *arXiv preprint arXiv:1901.05773*, 2019.

[80] David C Hansen, Guillaume Landry, Florian Kamp, Minglun Li, Claus Belka, Katia Parodi, and Christopher Kurz. Scatternet: A convolutional neural network for cone-beam ct intensity correction. *Medical physics*, 45(11):4916–4926, 2018.

[81] Christopher Kurz, Matteo Maspero, Mark HF Savenije, Guillaume Landry, Florian Kamp, Marco Pinto, Minglun Li, Katia Parodi, Claus Belka, and Cornelis AT Van den Berg. Cbct correction using a cycle-consistent generative adversarial network and unpaired training to enable photon and proton dose calculation. *Physics in Medicine & Biology*, 64(22):225004, 2019.

[82] Matteo Maspero, Mark HF Savenije, Tristan CF van Heijst, Joost JC Verhoeff, Alexis NTJ Kotte, Anette C Houweling, and Cornelis AT van den Berg. Cbct-to-ct synthesis with a single neural network for head-and-neck, lung and breast cancer adaptive radiotherapy. *arXiv preprint arXiv:1912.11136*, 2019.

[83] Johannes Schindelin, Ignacio Arganda-Carreras, Erwin Frise, Verena Kaynig, Mark Longair, Tobias Pietzsch, Stephan Preibisch, Curtis Rueden, Stephan Saalfeld, Benjamin Schmid, et al. Fiji: an open-source platform for biological-image analysis. *Nature methods*, 9(7):676, 2012.

[84] Andriy Fedorov, Reinhard Beichel, Jayashree Kalpathy-Cramer, Julien Finet, Jean-Christophe Fillion-Robin, Sonia Pujol, Christian Bauer, Dominique Jennings, Fiona Fennessy, Milan Sonka, et al. 3d slicer as an image computing platform for the quantitative imaging network. *Magnetic resonance imaging*, 30(9):1323–1341, 2012.

[85] Pierre Seroul and David Sarrut. Vv: a viewer for the evaluation of 4d image registration. In *MIDAS Journal (Medical Image Computing and Computer-Assisted Intervention MICCAI2008, Workshop-Systems and Architectures for Computer Assisted Interventions)*, pages 1–8. Springer, New York, 2008.

[86] C Boydev, B Demol, D Pasquier, H Saint-Jalmes, G Delpon, and N Reynaert. Zero echo time mri-only treatment planning for radiation therapy of brain tumors after resection. *Physica Medica*, 42:332–338, 2017.

[87] Gavin G Poludniowski, Philip M Evans, and Steve Webb. Cone beam computed tomography number errors and consequences for radiotherapy planning: an investigation of correction methods. *International Journal of Radiation Oncology* Biology* Physics*, 84(1):e109–e114, 2012.

[88] Halima Saadia Kidar, Hacene Azizi, and Boukellouz Wafa. Evaluation of ct to cbct deformable registration algorithms for adaptive radiation therapy. *Proceeding of Engineering and Technology*, 33:40–44, 2017.

[89] Halima Saadia Kidar and Hacene Azizi. Assessing the impact of choosing different deformable registration algorithms on cone-beam ct enhancement by histogram matching. *Radiation Oncology*, 13(1):217, 2018.

[90] AJ Cole, C Veiga, U Johnson, D DSouza, NK Lalli, and JR McClelland. Toward adaptive radiotherapy for lung patients: feasibility study on deforming planning ct to cbct to assess the impact of anatomical changes on dosimetry. *Physics in Medicine & Biology*, 63(15):155014, 2018.

[91] Xin Li, Yuyu Zhang, Yinghua Shi, Shuyu Wu, Yang Xiao, Xuejun Gu, Xin Zhen, and Linghong Zhou. Comprehensive evaluation of ten deformable image registration algorithms for contour propagation between ct and cone-beam ct images in adaptive head & neck radiotherapy. *PloS one*, 12(4):e0175906, 2017.

[92] Turki Almatani, Richard P Hugtenburg, Ryan Lewis, Susan Barley, and Mark Edwards. Simplified material assignment for cone beam computed tomography-based dose calculations of prostate radiotherapy with hip prostheses. *Journal of Radiotherapy in Practice*, 15(2):170–180, 2016.

[93] Halima Saadia Kidar and Hacene Azizi. Enhancement of hounsfield unit distribution in cone-beam ct images for adaptive radiation therapy: Evaluation of a hybrid correction approach. *Physica Medica*, 69:269–274, 2020.

Appendices

Appendix A

Supplemental figures

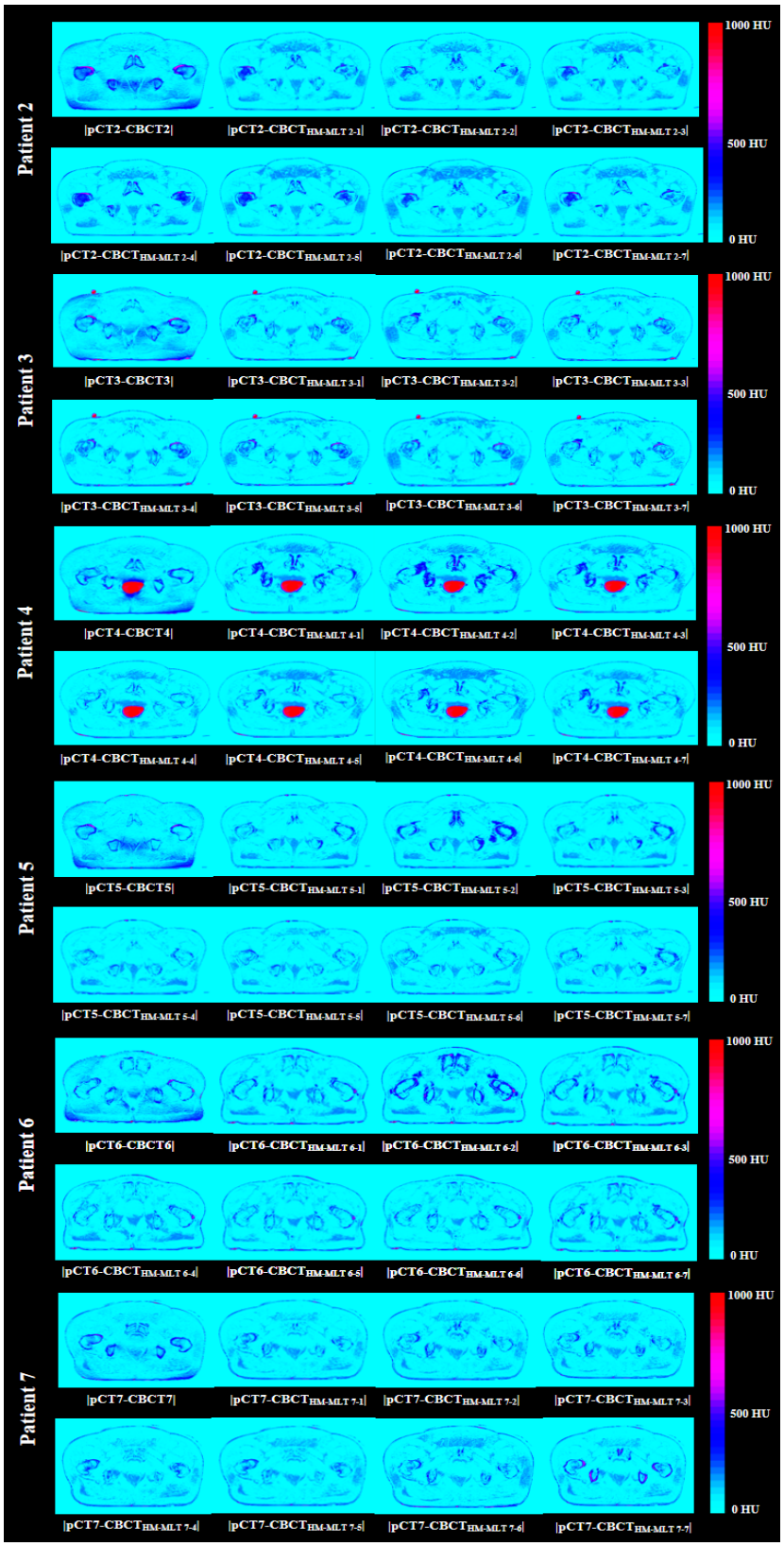

Figure A.1: Absolute difference between deformed pCT and CBCT for six patients before correction and after correction using pCT images obtained for 6 other patients.

ملخص

في الآونة الأخيرة، دمج التصوير المقطعي ذو الشعاع المخروطي (CBCT) في أجهزة العلاج بالأشعة لم يكن فقط أداة قوية لتحسين دقة وضعية المريض ولكن جعل تكييف تخطيط العلاج مع تغيرات تشريح المريض طوال فترة العلاج ممكنا، المعروف باسم العلاج الإشعاعي التكيفي (ART). خلال التخطيط ART، بعد مطابقة الصور CBCT المكتسبة يوميًا والصور المقطعية (pCT) والحصول على معلومات حول تغيرات على مستوى بنية المريض أو الأعضاء الداخلية، هناك حاجة لتكرار التصوير المقطعي لإعادة تخطيط العلاج في حال ما إذا كانت التغيرات معتبرة. على الرغم من أن تكرار الصور المقطعية يوفر أحدث المعلومات حول جسم الإنسان مع توزيع دقيق لوحدات هاونسفيلد (HU) اللازمة لحساب الجرعات، إلا أن اكتسابها المتكرر قد يشكل أضرارا صحية للمرضى بسبب الجرعة الإضافية. لذلك، فإن الهدف من هذه الأطروحة هو استثمار الصور CBCT اليومية لحساب الجرعات بدلا من تكرار الصور المقطعية. الهدف الرئيسي هو اقتراح استراتيجية واعدة للتغلب على القيود المتعلقة بالكمية العالية من الأشعة المتناثرة التي تقلل من جودة الصور CBCT مقارنة مع pCT.

تحقيقا لهذه الغاية، اقترحنا ثلاثة طرق متكاملة تسمح بتصحيح توزيع قيم وحدات HU في الصور CBCT. أول طريقة مقترحة كانت مستوحاة من حقيقة أن CBCT وصور pCT لا تمتلك نفس الرسوم البيانية لتوزيع المستويات الرمادية. لذلك، طبقنا عملية مطابقة الرسوم البيانية (HM) لمشابهة بياناتهما وتوفير إمكانية التمييز بين أنواع الأنسجة المختلفة المتواجدة في الصور CBCT. كطريقة ثانية، اقترحنا تطبيق عتبة متعددة المستويات (MLT) لتحسين صحة توزيع HU المتحصل عليها من HM. و أخيرًا، في الطريقة الثالثة، اقترحنا تعميم الطرق المقترحة مسبقًا للمساهمة في تقليل متطلبات عبء العمل بالتخطيط التكيفي. الفكرة الرئيسية هي إدراج مفهوم التطابق التشويهي بين عدة مرضى من أجل استغلال الصور pCT المتاحة في الأرشيف لتصحيح الصور CBCT بدلا من الحصول على صور pCT جديدة لكل مريض.

أظهرت نتائج التحليل البصري والإحصائي أن الطرق المقترحة يمكن أن تحسن من توزيع HU في صور CBCT وتولد صورًا مصححة في اتفاق جيد مع pCT.

الكلمات المفتاحية:

تصحيح CBCT، تطابق تشويهي، مطابقة الرسوم البيانية، عتبة متعددة المستويات، العلاج الإشعاعي التكيفي.